

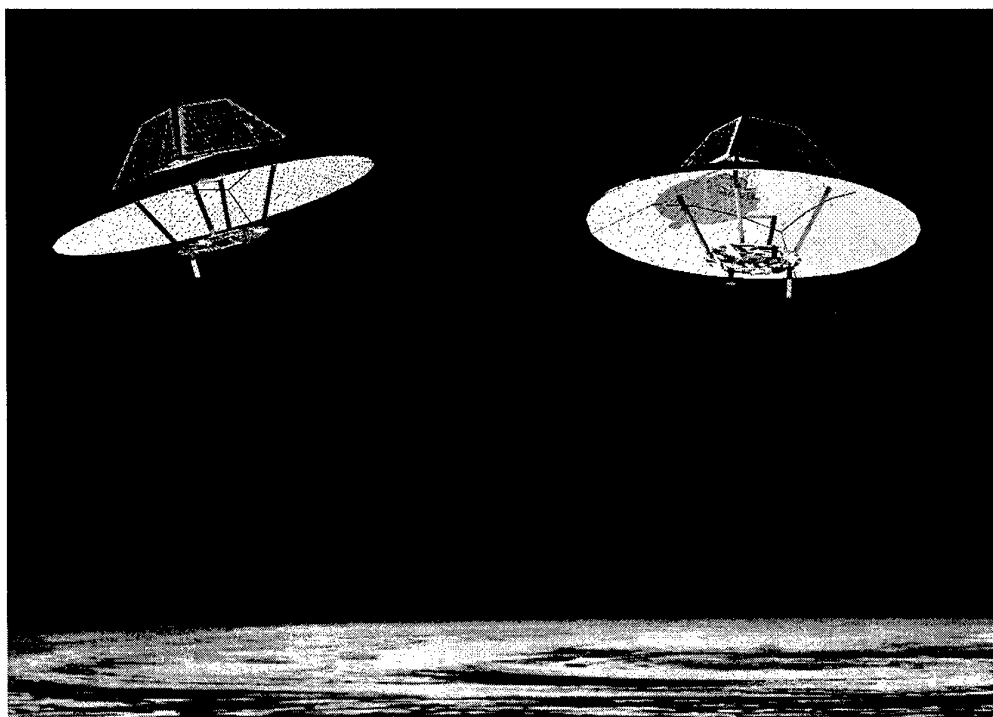
REPORT DOCUMENTATION PAGE			Form Approved OMB No. 0704-0188	
Public reporting burden for this collection of information is estimated to average 1 hour per response, including the time for reviewing instructions, searching existing data sources, gathering and maintaining the data needed, and completing and reviewing the collection of information. Send comments regarding this burden estimate or any other aspect of this collection of information, including suggestions for reducing this burden, to Washington Headquarters Services, Directorate for Information Operations and Reports, 1215 Jefferson Davis Highway, Suite 1204, Arlington, VA 22202-4302, and to the Office of Management and Budget, Paperwork Reduction Project (0704-0188), Washington, DC 20503.				
1. AGENCY USE ONLY (Leave blank)	2. REPORT DATE 5.Sep.02	3. REPORT TYPE AND DATES COVERED THESIS		
4. TITLE AND SUBTITLE A NOVEL METHOD FOR ACHIEVING SYNTHETIC APERTURE RADAR IMAGERY BY MEANS OF A MICRO-SATELLITE CONSTELLATION		5. FUNDING NUMBERS		
6. AUTHOR(S) 1ST LT MITCHELL OLIVIA S				
7. PERFORMING ORGANIZATION NAME(S) AND ADDRESS(ES) KINGS COLLEGE		8. PERFORMING ORGANIZATION REPORT NUMBER  CI02-525		
9. SPONSORING/MONITORING AGENCY NAME(S) AND ADDRESS(ES) THE DEPARTMENT OF THE AIR FORCE AFIT/CIA, BLDG 125 2950 P STREET WPAFB OH 45433		10. SPONSORING/MONITORING AGENCY REPORT NUMBER		
11. SUPPLEMENTARY NOTES				
12a. DISTRIBUTION AVAILABILITY STATEMENT Unlimited distribution In Accordance With AFI 35-205/AFIT Sup 1		12b. DISTRIBUTION CODE		
13. ABSTRACT (Maximum 200 words)				
20021029 032				
14. SUBJECT TERMS			15. NUMBER OF PAGES 163	
			16. PRICE CODE	
17. SECURITY CLASSIFICATION OF REPORT	18. SECURITY CLASSIFICATION OF THIS PAGE	19. SECURITY CLASSIFICATION OF ABSTRACT	20. LIMITATION OF ABSTRACT	

# **A Novel Method for Achieving Synthetic Aperture Radar Imagery by Means of a Micro-satellite Constellation**

Olivia S. Mitchell  
2DLT, USAF

14 Dec 2001

Supervisor: Dr. Craig I. Underwood



Submitted for the Degree of Masters of Philosophy

Surrey Space Center (SSC)  
School of Electronic Engineering, Information Technology and Mathematics  
University of Surrey

## Table of Contents:

Abstract	I
List of Abbreviations	II
List of Figures and Table	III
<b>Chapter 1 Introduction</b>	<b>1-1</b>
1.1 <i>Overview of the Research</i>	1-2
1.2 <i>Motivation</i>	1-3
1.3 <i>Background and Context</i>	1-5
1.3.1 <i>History of Synthetic Aperture Radar</i>	1-5
1.3.2 <i>Context of Project</i>	1-6
1.3.2.1 <i>Current SAR Systems</i>	1-6
1.3.2.2 <i>SAR Cluster Research</i>	1-9
1.4 <i>Objectives and Scope</i>	1-12
1.5 <i>Thesis Structure</i>	1-13
<b>Chapter 2 Background and Theory</b>	<b>2-1</b>
2.1 <i>Radar</i>	2-1
2.1.1 <i>Radio Basics</i>	2-1
2.1.2 <i>The Radar Equation</i>	2-2
2.1.2.1 <i>The Equation</i>	2-2
2.1.2.2 <i>Transmitted Power</i>	2-5
2.1.2.3 <i>Minimum Detectable Signal</i>	2-5
2.1.2.4 <i>Radar Cross Section (RCS)</i>	2-7
2.1.2.5 <i>System Losses</i>	2-8
2.1.2.6 <i>Measurements</i>	2-9
2.2 <i>Imaging Radar</i>	2-12
2.2.1 <i>Law of reflection</i>	2-13
2.2.2 <i>Microwave Scattering</i>	2-13
2.2.3 <i>Imaging Geometry</i>	2-15
2.2.4 <i>Signal Characteristics</i>	2-17
2.2.5 <i>Image Formation</i>	2-18
2.2.6 <i>Resolution</i>	2-19
2.3 <i>Bi-static Radar</i>	2-20
2.3.1 <i>Range Cells</i>	2-22
2.3.2 <i>Ovals of Cassini</i>	2-23
2.3.3 <i>Target Location</i>	2-23
2.3.4 <i>Synchronization</i>	2-25
2.3.5 <i>Doppler Relationships</i>	2-26
2.3.6 <i>Resolution</i>	2-27
2.4 <i>Synthetic Aperture Radar</i>	2-29
2.4.1 <i>Benefits of SAR</i>	2-29
2.4.2 <i>SAR Geometry</i>	2-29

<b>2.4.3 SAR Modes</b>	<b>2-32</b>
<b>2.4.4 Signal Properties</b>	<b>2-33</b>
2.4.4.1 <i>Transmitted Signal</i>	2-33
2.4.4.2 <i>Average Power Requirements</i>	2-35
2.4.4.3 <i>Echo Signal</i>	2-36
2.4.4.4 <i>Speckle and Clutter</i>	2-37
<b>2.4.5 Resolution</b>	<b>2-38</b>
<b>2.4.6 Signal Processing</b>	<b>2-39</b>
2.4.6.1 <i>Optical</i>	2-39
2.4.6.2 <i>Electric/Digital Signal Processors</i>	2-40
<b>2.4.7 Reconstruction Algorithm</b>	<b>2-42</b>
2.4.7.1 <i>Bi-static Extension of Reconstruction Algorithm</i>	2-46
<b>2.4.8 Image Defects and Corrections</b>	<b>2-48</b>
2.4.8.1 <i>Motion Compensation</i>	2-48
2.4.8.2 <i>Auto-focus</i>	2-49
 <b>Chapter 3 SAR System Design</b>	 <b>3-1</b>
<b>3.1 Scattering Properties</b>	<b>3-1</b>
3.1.1 <b>Electromagnetic Scattering from Rough Surfaces</b>	<b>3-1</b>
3.1.2 <b>Remote Sensing of Sea Ice</b>	<b>3-2</b>
<b>3.2 Power Requirements</b>	<b>3-7</b>
<b>3.3 Transmitter and Receiver Design</b>	<b>3-11</b>
3.3.1 <b>Transmitter Subsystem Design</b>	<b>3-11</b>
3.3.2 <b>Receiver Subsystem Design</b>	<b>3-14</b>
<b>3.4 Antenna Design</b>	<b>3-15</b>
<b>3.5 On-board Data Handling and Communication Downlink</b>	<b>3-22</b>
3.5.1 <b>Data Handling</b>	<b>3-22</b>
3.5.2 <b>Data Compression</b>	<b>3-24</b>
3.5.3 <b>Communication Downlink</b>	<b>3-27</b>
<b>3.6 Satellite Synchronization</b>	<b>3-32</b>
3.6.1 <b>Time</b>	<b>3-32</b>
3.6.2 <b>Phase</b>	<b>3-33</b>
3.6.3 <b>Signal</b>	<b>3-33</b>
<b>3.7 Ground Segment</b>	<b>3-35</b>
 <b>Chapter 4 Mission Design</b>	 <b>4-1</b>
<b>4.1 Satellite Design</b>	<b>4-1</b>
4.1.1 <b>Choice of Satellites</b>	<b>4-1</b>
4.1.2 <b>Satellite Structure</b>	<b>4-1</b>
4.1.3 <b>Power System</b>	<b>4-4</b>
4.1.4 <b>Guidance, Navigation and Attitude Determination and Control</b>	<b>4-5</b>
4.1.5 <b>Command, Data Handling and Communications</b>	<b>4-7</b>
<b>4.2 Formation and Orbit Design</b>	<b>4-9</b>
4.2.1 <b>Basic Orbit Design</b>	<b>4-9</b>
4.2.2 <b>Relative Motion Analysis</b>	<b>4-12</b>

<b>4.2.3 Orbital Perturbations</b>	<b>4-17</b>
4.2.3.1 <i>Non-Spherical Earth</i>	4-17
4.2.3.2 <i>Third-Body Perturbations</i>	4-18
4.2.3.3 <i>Atmospheric Drag</i>	4-18
<b>4.2.4 Constellation Optimization and Perturbations</b>	<b>4-19</b>
<b>4.3 Position Sensors and Error Requirements</b>	<b>4-27</b>
4.3.1 Position and Velocity Errors	4-27
4.3.2 Attitude Errors	4-30
4.3.3 Orbital Errors	4-31
<b>4.4 Slot Allocation and Power Flux Requirements</b>	<b>4-32</b>
4.4.1 Slot Allocation	4-32
4.4.2 Power Flux Requirements	4-33
 <b>Chapter 5 Conclusion</b>	 <b>5-1</b>
5.1 <i>Conclusion</i>	5-1
5.2 <i>Future Work</i>	5-5
5.2.1 Sea Ice Scattering	5-5
5.2.2 Antenna	5-6
5.2.3 Data Handling and SAR Processing	5-7
5.2.4 Synchronization	5-7
5.2.5 Satellite Design	5-8
5.2.6 System Applicability	5-8
 <b>Bibliography</b>	 <b>1</b>

## List of Acronyms:

AC—Alternating Current  
ADC—Analog to Digital Converter  
ADCS—Attitude Determination and Control System  
AFRL—Air Force Research Labs (US)  
ALOS—Advanced Land Observing Satellite  
AMI—Active Microwave Instrument  
ASAR—Advanced Synthetic Aperture Radar  
BAQ—Block Adaptive Quantization  
BAVQ—Block Adaptive Vector Quantization  
BPSK—Binary Phase Shift Keying  
CNES—Centre Nationale pour des Etudes Spatiales  
CW—Continuous Wave  
DAC—Digital to Analog Converter  
DC—Direct Current  
DDS—Direct Digital Synthesis  
DEM—Digital Elevation Models  
EIRP—Effective Isotropic Radiated Power  
ESA—European Space Agency  
ERS—Earth Remote Sensing  
FFT—Fast Fourier Transform  
FY—First Year Ice  
GEO—Geostationary Orbit  
GPS—Global Positioning System  
HPOP—High Precision Orbit Propagator  
IF—Intermediate Frequency  
ITU—International Telecommunications Union  
JERS—Japanese Earth Remote Sensing  
JPL—Jet Propulsion Laboratories  
LEO—Low-Earth Orbit  
MSPS—Mega Samples per Second  
MY—Multi-Year Ice  
NASDA—National Space Development Agency (Japan)  
PGA—Phase Gradient Auto-Focus  
PRF—Pulse Repetition Frequency  
QPSK—Quadrature Phase Shift Keying  
RADAR—Radio Detection and Ranging  
RAAN—Right Ascension of the Ascending Node  
RCS—Radar Cross Section  
RF—Radio Frequency  
ROM—Read Only Memory  
S/N—Signal to Noise Ratio  
SAR—Synthetic Aperture Radar  
SSC—Stripmap Spotlight Compression  
SSTL—Surrey Satellite Technologies, Ltd.  
STK—Satellite Tool Kit

## List of Tables and Figures:

Figure 1.1a: Geometry of Proposed Cluster  
Figure 1.1b: Geometry of Proposed Cluster  
Figure 2.1: Isorange Contours  
Figure 2.2: Iso-Doppler Contours  
Figure 2.3a: Reflected Energy  
Figure 2.3b: Scattered Energy  
Figure 2.4: Relative Nature of Surface "Roughness"  
Figure 2.5: Backscattering Coefficient with Respect to Incidence Angle  
Figure 2.6: Imaging Geometry  
Figure 2.7: Left-Right Ambiguity Problem  
Figure 2.8: Image Geometry  
Figure 2.9: Resolution Cell  
Figure 2.10: Bi-static Radar Geometry  
Figure 2.11: Bi-static Isorange Contours  
Figure 2.12: Iso-Doppler and Isorange Contours for Bi-static Radar  
Figure 2.13: Bi-static Resolution  
Figure 2.14: SAR Concept  
Figure 2.15: SAR Geometry  
Figure 2.16: Geometry of a Curved Earth  
Figure 2.17: Spotlight SAR  
Figure 2.18: Pulse Compression  
Table 3.1: Estimated Normalized Radar Cross Section for Sea Ice at 2.4 GHz at 4° Inclination  
Table 3.2: Sea Ice Radar Contrast at 2.4 GHz at 4° Inclination  
Figure 3.1: Average Power Requirements  
Figure 3.2: Peak Power Requirements  
Figure 3.3: DC Power Requirements  
Figure 3.4: Transmitter Block Diagram  
Figure 3.5: Receiver Block Diagram  
Figure 3.6a: Side View of Stowed Antenna  
Figure 3.6b: Deployed Antenna Design  
Figure 3.7: Graph of Focal Length and Angle Relationship  
Figure 3.8: Parabolic Reflector Focal Length  
Figure 3.9: Dipole Feed Design  
Table 3.3: Image Size Requirements  
Figure 3.10: BAQ Block Diagram  
Figure 3.11: Relationship of Distance to the Ground Station with respect to the Elevation Angle  
Figure 3.12: System Margin with Acquisition at the Horizon  
Table 3.4: Link Budget for Communication Downlink  
Figure 3.13: SAR Processing Flow  
Figure 4.1: Enhanced Micro-Satellite Design with Cubic and Truncated Pyramid Shape  
Figure 4.2a: Basic Modular Design  
Figure 4.2b: Modular Design  
Figure 4.3: Proposed Propulsion Systems  
Figure 4.4: SSTL 2-Axis Sun Sensor  
Figure 4.5: Horizon Sensor  
Figure 4.6 GPS Module for an Enhanced Micro-Satellite  
Figure 4.7: Launch Configuration for the Satellite  
Figure 4.8: Deployed Configuration of the Satellite

Figure 4.9: Isorange and Iso-Doppler Contours  
Figure 4.10: Polar View of Satellite's Orbits  
Figure 4.11: Ground Tracks of the Satellite  
Figure 4.12: Relative Position  
Figure 4.13: Relative Velocity  
Figure 4.14: Relative Position of the Satellites Propagated over 15 Days  
Figure 4.15: Relative Velocity Propagated over 15 Days  
Figure 4.16: Nodal Drift of Initial Formation  
Figure 4.17: Nodal Drift with  $3.5^\circ$  RAAN Separation  
Figure 4.18: Nodal Drift of Revised Constellation Design  
Figure 4.19: Relative Position of Satellites after Correction  
Figure 4.20: Relative Velocity of Satellites after Correction  
Figure 4.21: Imaging Latitude based in RAAN Differences  
Figure 4.22: Power Flux Density at S-Band



## **Abstract:**

The current emphasis in the satellite industry is on replacing large satellite platforms with one or more smaller satellites, built at lower costs, yet able to accomplish similar mission objectives. In this context, there is increasing interest in the potential capabilities and applications of so-called "micro-satellites"—satellites of 10-100 kg. However it is recognized that such small satellites pose severe constraints on payload volume, mass and power. Thus, they would appear to be inappropriate for missions such as synthetic aperture radar (SAR) imaging, where payloads have significant size and power demands — specifically the large SAR antenna and high-power radar transmitter.

The primary reason for the high transmit power requirement is that traditional SAR systems use backscatter, which is weak from most terrain types as most energy is scattered in the forward direction. Thus, if it were possible to gather this forward scattered element, then the transmit power requirements could drop significantly, potentially making it feasible for installation on a micro-satellite.

This research is based on this principle of collecting to the forward scattered element—a novel method by which two micro-satellites "fly" in a specific formation to accomplish a SAR imaging mission bi-statically. The transmitting satellite will be the master, with the receiver satellite slaved off it for synchronization. The satellites view a swath of 30x30 km, at a ground resolution of 30 m, from an altitude of 700 km. The constellation geometry proposed requires minimal orbit control resources, and allows for the resolution of the left-right ambiguity.

The satellite design is based on the Surrey Satellite Technology, Ltd. enhanced micro-satellite, with a mass of 100 kg, and a standard volume of 1x1m base and a 0.6 m height. The satellite shape will be a truncated pyramid, allowing for increased power production by the body-mounted Gallium Arsenide solar cells and provides a larger platform base for the 2.5 m diameter parabolic dish antenna.

The signal is transmitted at 2.4 GHz, as a "chirped" pulse of 34  $\mu$ s duration. The receiver will collect, compress and store the data, which will later be sent to a ground station. This will require a data storage of 1 Gbit and a downlink of 2 Mbps. The main processing of the SAR data will be conducted on a ground facility, due to the complex and time required for processing.

## **1.1 Overview of the Research:**

This thesis is centred on the proposition of placing a SAR system on a micro-satellite constellation, reducing cost whilst maintaining the quality of images. This idea was studied in 1993 by Ms. Regina Coult at the University of Surrey [COUL-97]. The resulting conclusion was that the power needed for SAR is too high to be placed on a small satellite—100 kg—and maintain the focused image achievable with the then current SAR satellites. The average small satellite can provide power at a few hundred watts—100W for the enhanced micro-satellite used in this research. Since then, Astrium has also begun a project to design TerraSAR, a SAR system based on a pair of small, yet otherwise conventional, SAR satellites, one operating at X-band and the other at L-band. However, detailed information concerning this project is not yet available.

If a SAR system appears impractical to place on a single micro-satellite, the possibility exists that through task allocation between multiple satellites flying in formation, a single SAR system can be synthesized. This idea still encompasses the problem of high power consumption by the transmitter and introduces another level of complexity with the accuracy of control needed to maintain coherent signal processing, but offers a potential solution.

The proposed architecture is a cluster of two satellites—a transmitting satellite and a receiving satellite—in a bi-static configuration. Each satellite is a micro-satellite of similar mass and cross-sectional area to allow for similar drag, negating the need for excessive station keeping resources. The transmitting satellite will be the master satellite and the receiver will be slaved to it.

The satellites are placed in a formation as shown in Figure 1.1a and b. The receiver and the transmitter will be offset to ensure a separation of 60 km during imaging. This formation allows for the satellites to be deployed from the same launch vehicle and requires a  $\Delta V$  to realign the transmitter to the receiver. From this position, the receiver will receive the forward-scattered echoes, rather than the backscatter. This will significantly reduce the power required for the transmitter.

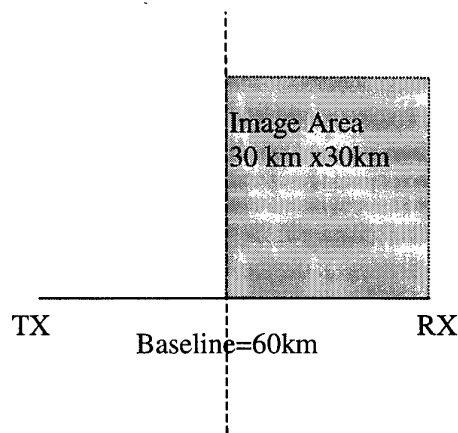


Figure 1.1a

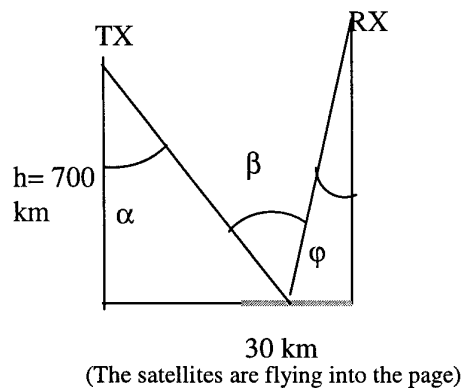


Figure 1.1b

Geometry of Proposed Cluster

The antenna of the transmitter is pointed at the angle,  $\alpha$ , approximately  $3.7^\circ$ , such that the antenna beam centre is located at approximately 45 km from the transmitter (as seen in Figure 1.1b). These design decisions are necessary to maintain signal-processing requirements within feasible limits. The receiver antenna will point at an angle,  $\phi$ , of approximately  $2^\circ$  to collect the forward-scattered element.

## 1.2 Motivation:

There is a dual motivation for this research: to show the feasibility of a SAR system on a micro-satellite constellation providing high-resolution, radar imagery and to apply the system to study the polar regions, monitoring and classifying sea ice for scientific and commercial benefits.

High-resolution imagery of the Earth's surface is a useful tool in scientific, monitoring, and commercial applications. However, with the current state of system design, SAR platforms require large amounts of time and money, and high level of technical expertise. Such projects can only be undertaken by nationally or internationally supported programs. This limits the diversity of SAR imagery, as well as the actual number of SAR platforms put into operation. Due to the few operational platforms that exist, the imaged area and amount of data that can be collected is severely limited.

Yet, while the availability of these data is limited, its uses can be considered almost endless. Radar can be used in a variety of scientific uses: ocean or land monitoring, disaster monitoring, and climate studies, as well as commercial mapping. In order to fully exploit the benefits of high-resolution SAR imagery, the platforms for space-based systems need to become available for wider use.

This study was designed to place a SAR system on a constellation of micro-satellites with a modular design for fast, reproducible and replaceable system and to show the feasibility of this system. The micro-satellite size and modular design makes the system highly cost-effective. Being small in size also allows for reduction of launch costs and the increase in launch opportunities as they can be launched as secondary payloads.

The motivation for choosing the polar regions as the area of interest for the design was based on the commercial and scientific benefits. Commercially, mapping of the polar regions during both the summer and winter would provide shipping companies with polar routes, thus reducing the shipping costs and time. Scientifically, the polar regions are areas of great interest in studying the effects of polar ice sheets' growth, motion and development on climate changes of the Earth. Also, this area is often covered by clouds, making optical imagery ineffective. The polar regions, therefore, seem to be a perfect example for which a low-cost SAR system could be valuable.

### **1.3 Background and Context:**

#### **1.3.1 History of Synthetic Aperture Radar:**

Radar, **RA**dio **D**etection **A**nd **R**anging, has beginnings in many countries, but the first radar was invented in 1904 by Christian Hulsmeyer for detecting ships at a distance of 1 mile [SKOL-80]. Being developed for military applications, each new development was tightly guarded. It was the outbreak of WWII that supplied the impetus for significant developments in radar. Initially a location device, other applications were soon found, both civilian and military, eventually leading to the development of radar imaging from aircraft. As continuous wave radars gave way to advanced pulsed forms, radar imaging became more widespread, allowing for accurate images to be gathered during night and day and all-weather operations [SKOL-80]. Today, radar imaging is used for applications ranging from ballistic missile early warning, monitoring the use of civilian airspace, air and marine navigation, and remote sensing [SKOL-80].

SAR was first detailed in 1950 by Carl Wiley of the Goodyear Aircraft Corporation, when he discovered that the Doppler spread of the echo signal could be used to synthesize a longer aperture [CURR-91]. To improve the resolution in the azimuth direction requires a narrower beam width, and therefore a larger aperture. This improvement is limited by the physical factors of the aperture and radar platform. Wiley noticed that the length of an aperture could be synthesized by using the motion of the radar platform to make multiple radar measurements. These would then be coherently added using signal processing and the corresponding Doppler shift, creating a single image with the same resolution as one with an aperture the length of the traveled distance. The power of SAR, therefore, comes from the signal processing of the received echo signal rather than the components themselves.

### **1.3.2 Context of Project:**

#### **1.3.2.1 Current SAR Systems:**

As the demand for space borne radar images has increased, the number and variety of systems designed and implemented has grown to match. For the purposes of this thesis, the discussion will be limited to those systems used for imaging and mapping only.

To begin the discussion, the similarities of all SAR systems will first be discussed to limit their repetition. For all the independent, Earth-orbiting satellites currently investigated the orbit description is a low Earth, near-circular orbit, with an altitude of around 700 km, with a sun-synchronous inclination of approximately  $98^\circ$  [FRAN-99]. This orbit has a period of around 98 minutes, requiring both a high data rate for downlink systems and multiple ground station sites. This orbit places the solar array panels in maximum exposure to fulfill the need for high transmit power [FRAN-99].

The first satellite designed for remote sensing of the Earth using SAR is Seasat. It was designed to monitor oceanographic phenomena and determine the requirements for an operational SAR satellite. The payload consisted of a SAR system for imaging, a radar altimeter to measure wave height, a satellite scatterometer to measure wind speed, and a microwave radiometer to measure surface temperature. The SAR system operated at L-band with a pulse repetition frequency of 1500 Hz and a pulse length of 33.4  $\mu\text{s}$ . The swath width was 100 km with a theoretical resolution of 25 by 25 m. The peak power required was 1.0 kW. The Seasat mission ended after only 42 hours of operation due to a power system failure [JPL-01].

Following Seasat came the missions of the Shuttle Imaging Radar, SIR-A, SIR-B, and SIR-C X-SAR. None of the missions were freestanding satellites, as the SAR imaging was conducted from the cargo bay of the space shuttle. These systems were used for understanding geological radar signals with SIR-A, the effect of multi-incidence angle imagery for SIR-B and vegetation monitoring, soil moisture measurement, oceanography

applications and volcanism for SIR-C X-SAR. These systems worked at L-band frequency, 23.8 cm wavelengths, with SIR-C X-SAR having a C-band frequency, 5.8 cm wavelengths, and the X-band frequency, 3.0 cm wavelength, capability as well. The power consumption ranged from a peak power of 1.0 kW for SIR-A, 1.12 kW for SIR-B and 3-9 kW, depending on the radar pulse characteristics and the application, for SIR-C. The swath width of this system varied from 15-90 km and could achieve a resolution of 40 by 40 m for SIR-A and 30m or better in both the range and azimuth directions for SIR-B and SIR-C [JPL-01]. The characteristics of these SAR systems cannot be directly applied to this study since they are not freestanding systems, but a shuttle payload only. This allowed for a relaxation of certain constraints [FRAN-99].

RADARSAT-1 and 2 are a Canadian-led SAR project, in conjunction with the United States, which uses C-band radar, 5.3 GHz, to monitor the Earth's resources and environmental changes, and to support the commercial industries of fishing, shipping, agriculture and oil exploration. RADARSAT-1 was launched in 1995, to be followed by RADARSAT-2, in 2003, to continue the mission. These satellites use a state-of-the-art electronically steered, multi-polarizable, phased array antenna to gain high-resolution images using separate polarization schemes. RADARSAT-1 weighed 2750 kg at launch with the capability of producing 2.5 kW of power. The radar system payload had a frequency of 5.3 GHz, an RF bandwidth of 30.0 MHz and utilized an average power of 300W and a peak power of 5 kW. With an antenna 15m x 1.5m, the system was able to achieve a standard resolution of approximately 30 m within a swath width of 100 km, at incident angle of 10-60 degrees [RADA-01].

ERS-1 and 2 are projects by the European Space Agency, ESA, starting with ERS-1 in 1991 and continuing the mission with ERS-2 in 1995, and is considered the premiere SAR satellite developed in Europe. The overall mission of both satellites is the imaging and measuring of the polar icecaps, oceans and coastal areas. These two satellites are similar in construction save for the additional stratospheric and tropospheric ozone measuring device—GOME and advanced on-board data handling, which is present on ERS-2 only. The total mass was 2157 kg on launch and covered a 12-metre distance at

the widest point when fully deployed. The payload includes the Active Microwave Instrument (AMI) and a radar altimeter and wind scatterometer. AMI is the biggest on-board system yet produced, which operates in multiple modes, one of which is SAR. AMI produces, from an antenna 10m by 1m, a swath-width of 100 km at an angle of 20-60 degrees from nadir and a resolution of 25 metres in the range direction and 12.5 in the azimuth direction. Operating in the C-band, at 5.3 GHz, the AMI uses a peak power of 4.8 kW, approximately 550 W average power, to produce an image and directly down linked to Earth at 4.5 million pixels per second. At these specifications, the sampling rate of the system is almost 20 Mbits/s with a downlink of 105 Mbit/s and has an on-board storage capacity of 6.5 Gbits [ERS-01].

JERS-1, launched in 1992 by the Japanese Space Agency NASDA (National Space Development Agency), and operating until 1998, performed nearly as well as ERS-1. However, JERS-1 is an Earth observation satellite dedicated to imaging landmasses for geological study, environmental protection, agricultural industry and disaster prevention. The SAR system operates with a 12 x 2.5 m antenna at a frequency of 1.275 GHz. Unlike similar missions, JERS-1 operates at an altitude of only 570 km. The SAR system creates a swath of 75 km at an angle of 35 degrees from nadir and has a resolution of 30 m across-track and 18 m along-track [NASD-01].

ALOS, Advances Land Observing Satellite, is also a NASDA project, scheduled for launch in 2002. Its mission is similar to that of JERS-1, but concentrating its resources on the Asian Pacific region. This satellite will weigh approximately 3850 kg at the time of launch. Again working in the L-band region, this satellite will take advantage of a phased-array antenna to provide a higher performance than previous satellites. With a swath width of approximately 75 km, and an incident angle of between 18 and 48 degrees, the system should provide a resolution of 10m in the across and along track directions. Like other SAR systems, the ability to produce these high quality images comes with a price in power consumption—nearly 7 kW for complete operation of the satellite [NASD-01].



The most recent undertaking in mono-static SAR systems is EnviSat. This satellite will be 26x10x5m when fully deployed in orbit, with a total mass of 8211 kg. The total payload consists of ten different systems to carry out monitoring of the Earth's environment. The radar instrument of most interest is the Advanced Synthetic Aperture Radar system (ASAR) [ENVI-01].

ASAR is a high-resolution, wide-swath instrument calibrated for land, sea ice and ocean monitoring—with special emphasis on ocean characterization, disaster monitoring and deforestation monitoring. It has the ability to operate in an image, wide swath, cross polarization, wave and global monitoring mode. This instrument replaces the passive array antenna with an active one—10m x 1.3m—which provides a more than 400 km swath width when using the ScanSAR techniques. In simple imaging mode, the satellite offers a resolution of 30m by 30m—the resolution decreases for other modes. This system will operate at a frequency of 5.3 GHz and a PRF of 2100 Hz. ASAR weighs over 830 kg and had a power consumption of 713 W to 1365 W depending on the mode. The data rate for ASAR is over 100 Mbps for the image, wide swath mode and cross polarization modes and 0.9Mbps for the wave and global monitoring [ENVI-01].

#### **1.3.2.2 SAR Cluster Research:**

Using these existing SAR missions as a baseline, the performance parameters for a SAR satellite constellation can be determined. To be competitive with the current technology, the system must offer the same image quality, in terms of resolution, while still being feasible from the small satellite platform and at a much lower cost.

There are two systems currently under investigation by CNES, Centre Nationale pour des Etudes Spatiales, and the US Air Force. Each project involves the implementation of SAR-type imaging from small satellite platforms.

#### *1.3.2.2.1 Interferometric Cartwheel:*

The interferometric cartwheel is a project proposed by CNES. The basic concept of this study is to use passive receivers to trail an already existing SAR satellite and take simultaneous images to be used later to improve the final resolution and provide interferometric data [MASS-99]. This uses cost-effective satellites to fully exploit the possibilities of coherent combination, such as Digital Elevation Models (DEM), and super-synthesis of range and azimuth using a diversity of viewpoints [MASS-99].

In this constellation, all satellites are limited to 100 kg but maintain the capability of three-axis attitude control and adequate station keeping. Since these receivers are passive, the mission requirement is to maintain the spacecraft pointing to the area illuminated by the emitter. This requirement is not severe, as it need only be accurate to a fraction of the width of the antenna pattern due to the passive nature of the system [MASS-99]. The receiving satellite will then store the data for use in later signal processing. Since the satellites will work in conjunction with each other, there exists the possibility to split the requirements for data storage and global antenna surface. As currently designed, each micro-satellite has a deployable umbrella antenna, approximately  $4\text{m}^2$  in area, 20 Gbits of data memory storage and a 50Mbit/s downlink channel. The envisioned mission is to achieve global coverage over the lifetime of the satellites [MASS-00].

The orbit design for this system consists of three micro-satellites, equally spaced, orbiting ahead of the emitter on the same trajectory, and pointed to allow for the collection of the scatter from the emitter [Mass-2000]. An advantage of this configuration is the geometric stability provided to the baselines, both horizontal and vertical. It is the maintenance of these distances, which allows for the independence of the images, making coherent combination possible.

Similar to the project proposed here, the interferometric cartwheel faces the challenges of maintaining the precise distance, within a 10% error for each baseline maximum value,

minimizing the spillover from the emitter and calibrating the oscillators and clocks of the receiver to the emitter.

#### *1.3.2.2.2 TechSat21:*

TechSat21 is the proposed mission of Air Force Research Labs (AFRL), in conjunction with Massachusetts Institute of Technology, Stanford, and Texas A&M University. This project is not the passive mission of CNES, but rather active, placing complete SAR systems onto each small satellite and then placing these satellites in a tightly controlled formation. These satellites will be used for surveillance, ground mapping, navigation and communication [JPL-01].

The TechSat21 mission will work using the principles of traditional SAR in a distributed network of micro-satellites operating collectively to function as a single satellite. Each of the small satellites will communicate with the others to share the processing, communications and payload functions. The cluster concept allows for life cycle cost reductions by mass-producing the satellites which are upgradeable, as technology increases, new satellites can be integrated into the existing system, and replaceable, as a satellite reaches the end of its lifetime, it is easily replaced by another.

The radar payload on-board the TechSat21 satellites will be known as Ground Moving Target Indication. Within the formation, each satellite will coherently detect the response of its own transmitted pulse and the bi-static responses of the other satellites. This allows for independent samples with different angles-off-arrival. The spatial differences between the satellites and the corresponding difference in propagation paths lead to errors affecting cluster performance.

In order to achieve this sparse array, it will be necessary for the cluster to maintain a fixed and accurate geometry, changing only by small perturbations. This need for rigid control of the satellite's position will be one of the greatest challenges of the mission. A combination of possible sensors—laser and radar ranging, RF communications link

ranging, differential GPS and star trackers—allow for relative position to be known within a 30 mm error. Therefore, a suitable orbit control system will also have to be developed. This is not a low-cost system.

#### ***1.4 Objectives and Scope:***

The primary objective of this research is to provide a system study to define a bi-static SAR system compatible with a low-cost micro-satellite platform, making this technology more readily available for varied scientific and commercial purposes. This objective will be achieved through a basic design phase, and a feasibility study of the system with modifications of the design based upon the outcome of a feasibility review.

The research approach can be divided into three main parts:

- 1) The initial approach to the research was a detailed review and analysis of current SAR systems and technologies. This included the basic theories of radar, imaging radar, synthetic aperture radar and multi-static radar to gain an understanding of the guiding principles and design factors, which would be important in the design of a micro-satellite SAR system. Also, a study was conducted of the current SAR systems in use or in design to ensure the system quality met industrial standards. This initial research included a study into the design of a micro-satellite to determine the constraints that would be placed upon the system.
- 2) Following the theoretical research, a bi-static SAR system was designed within the constraints of the SSTL enhanced micro-satellite design. This includes a theoretical study into the requirements of the components of the SAR system, transmitter, receiver, data storage and downlink, antenna and ground signal processing segment. The design also includes a base level analysis of the synchronization required between the transmitter and the receiver, as the system is to be distributed on two satellites.

- 3) The final step of the research was to design and study the mission level requirements of the system: orbit and constellation design,  $\Delta V$  requirements for orbital manoeuvres and station keeping, relative motion and position analysis, and a constellation control study to maintain the imaging geometry.

This study offers a researched solution to the requirements and constraints of a bi-static SAR system placed on a micro-satellite. The research is limited to a theoretical study and simulation-based review. There was no construction or testing of hardware conducted during the project.

### ***1.5 Thesis Structure:***

This report is structured into five chapters discussing the basics of radar, radar imaging, synthetic aperture radar and the specific application of these principles to the project.

Chapter 1 is designed as an overall introduction to the project, providing a brief history of the area of study and an explanation into the motivation of the research, the scope and objectives of the project, and the setting of the project in the context of current state-of-the-art.

Chapter 2 is designed to provide the theoretical foundation for the project. It explains the basic theory of radar systems, beginning with the structure of the radio wave, the performance of a radar system, and an investigation into the individual components to the radar equation. From this, the theory of imaging radar is built, explaining the theory of scattering of electromagnetic waves and how the image is formed. Next, as the project specifically deals with the distribution of the radar system onto two platforms, the concept of bi-static radar is explored and the basic equations and theories of the previous discussion on radar are expanded to encompass this variation. Finally, the theory is expanded to provide an explanation of SAR. A concentration will be placed on the

geometric characteristics of SAR, the properties of the signal, which can be exploited in the synthesis, and the processing methods used for SAR data.

Having supplied a sound theoretical background for the project, Chapter 3 describes the design and characteristics of the proposed SAR system. The chapter looks at the basic scattering properties of the chosen imaging region to gain an understanding of the environment. Next, an investigation into the basic design of the radar transmitter and receiver subsystems, to include a requirements study and simplified block diagram, is provided. There is no detailed hardware design of any of the SAR components. The description and design for the radar antennas are then provided to explain the deployment sequence, allowing for a compact volume prior to deployment, the geometry of the antenna and the radiative characteristics. The system synchronization process, imperative due to the distributed nature of the system, is discussed. Finally, an analysis of the ground segment of the system, for the reception and processing of the data is discussed.

Chapter 4 investigates the mission design aspects of the project. The spacecraft design characteristics are detailed as they apply to the SAR system and a discussion on the choice of platforms is provided. Finally, the orbit design and constellation control is examined.

Chapter 5 will provide the conclusion of the research into SAR technology placed on a micro-satellite and discusses further work, which will be necessary to implement such a system.

## Chapter 2 Background and Theory:

### 2.1 Radar:

#### 2.1.1 Radio Basics:

To understand radar, it is first necessary to consider the nature of electromagnetic waves and wave propagation. Radio frequency (RF) propagation is defined as the travel of electromagnetic waves through a medium. Consisting of frequencies between 100 kHz and 40 GHz, radio waves travel in a direct line of sight as wave fronts—contours of equal phase in step with each other [ELACa-87]. To first gain a general understanding of radio wave propagation, it is usual to consider a point source, assumed to radiate perfectly in all directions in the form of a sphere. At a sufficient distance from the radiating source, it can be assumed that the wave front is planar—the phase is constant within a small error, defined by the system parameters [ELACa-87]. The sufficient distance is defined by the far field equation:

$$R_{ff} = \frac{2d^2}{\lambda} \quad [2.1]$$

where  $d$  is the diameter of the transmitting antenna,  $\lambda$  is the wavelength and  $R_{ff}$  is the minimum far field distance[ELACa-87].

A radio signal is often represented by the time-varying, sinusoidal equation:

$$\begin{aligned} v(t) &= A \sin(\omega(t - \tau)) \\ v(t) &= A \sin(\omega t + \phi) \end{aligned} \quad [2.2]$$

where  $A$  is the amplitude,  $\omega$  is the angular frequency,  $\tau$  is the time delay between the source and the receiver and  $\phi$  is the phase. This would be the nature of the signal seen by the observer, with a variance in  $\phi$  depending upon the distance from the site to the observer. If the distance between the source and the observer is changing, at a given rate, the Doppler effect—negative shift for increasing distance and positive shift for a decreasing distance, shifts the frequency of the received signal. This Doppler frequency

shift, can be found by the equation:

$$f_d = \frac{v_r}{\lambda} \quad [2.3]$$

where  $v_r$  is the relative velocity between the transmitter and the receiver, and  $\lambda$  is the wavelength [SKOLa-62]. This aspect of the propagation of radio waves is essential in the formation of radar to determine the range rate of the target.

## **2.1.2 The Radar Equation:**

### **2.1.2.1 The Equation:**

These basic principles of radio wave propagation led to the development of the radar equation—a description of the range performance of a system as the fundamental relationship between the radar system parameters, the received signal and the target. The equation relates the power transmitted in the system to the power received at the receiver, including the interactions with the target, as the simple propagation of the radio wave from the transmitter to the receiver is now affected by the reflection of the incident energy off an object.

The first portion of the equation is based on the idea of the power density of a signal radiated from an omni-directional source. From the propagation theory of electromagnetic waves, it is known that the peak power density,  $P_D$ , of the signal at a distance,  $R$ , from the radiating site is:

$$P_D = \frac{P_t}{4\pi R^2} \quad [2.4]$$

where  $P_t$  is the peak transmitted power. The power density equation is the transmitted power multiplied by the spreading loss [SKOLb-62].

In the situation where the antenna is no longer omni-directional, but channels the power in a certain direction, the gain of the transmitting antenna,  $G_t$ , is added to the equation:



$$P_D = \frac{P_t G_t}{4 \pi R^2} \quad [2.5]$$

where the antenna gain is given by the equation:

$$G = \frac{4 \pi A \eta}{\lambda^2} \quad [2.6]$$

and  $A$  is the area of the antenna,  $\eta$  is the antenna efficiency and  $\lambda$  is the wavelength [SKOLb-62].

The target intercepts a portion of this power and re-radiates a fraction of the signal back in the direction of the radar, based on the target's equivalent area that reflects back in the direction of the radar and its electromagnetic characteristics. The radar cross section can be understood through the equation:

$$\sigma = A_s G_{rs} (1 - f_e) \quad [2.7]$$

where  $(1 - f_e)$  is the fraction of power not absorbed,  $A_s$  is the area of the scattering element and  $G_{rs}$  is the gain of the scatterer in the direction of the receiver [SKOLb-62].

Therefore, the power re-radiated from the scatterer is:

$$P_e = \frac{P_t G_t \sigma}{4 \pi R^2} \quad [2.8]$$

As with the signal from the transmitter to the target, the re-radiated signal, returning to the receiver, is affected by the free space loss. The antenna at the receiver only captures a portion of this echo power—the power per unit area at the receiver is the power re-radiated from the scatterer multiplied by the gain of the receiver and divided by the surface of the spreading sphere of energy [SKOLb-62]. If this is multiplied by the effective receiving area of the receiver antenna, the power received is:

$$\begin{aligned} P_r &= \frac{P_t G_t \sigma A_r}{(4 \pi R^2)^2} \\ \text{However} \quad : G_r &= \frac{4 \pi A_r}{\lambda^2} \\ \therefore P_r &= \frac{P_t G_t G_r \lambda^2 \sigma}{(4 \pi)^3 R^4} \end{aligned} \quad [2.9]$$

where  $G_r$  is the gain of the receiving antenna and  $A_r$  is the area of the receiving aperture.

This is an idealized form of the equation, in which there is only one scattering element in the sight of the radar. This is not the case for remote sensing applications where the target is usually an extended area rather than a point target. In this case, the radar cross section is statistically averaged over a predetermined portion of the total area. This concept will be explained later when discussing range bins in imaging applications.

One of the benefits of the range equation is the ability to determine the maximum range,  $R_{\max}$ , of the radar. This is done by replacing the received signal with the minimum signal,  $S_{\min}$ , detectable by the receiver and solving for the range [SKOLb-62]. This leaves the solution for the maximum range as:

$$R_{\max} = \left( \frac{P_t G_t G_r \lambda^2 \sigma}{(4\pi)^3 S_{\min}} \right)^{\frac{1}{4}} \quad [2.10]$$

Substituting the value for the minimum detectable signal with its related minimum signal-to-noise ratio,  $S/N$ , the receiver sensitivity, for the receiver gives the final equation as:

$$R_{\max} = \left( \frac{P_t G_t G_r \lambda^2 \sigma}{(4\pi)^3 (S/N)_{\min} F_n k T_o B} \right)^{\frac{1}{4}} \quad [2.11]$$

where  $F_n$  is the noise figure for the receiver and  $kT_o B$  is the thermal noise of the receiver. The noise figure is defined as the ratio of the input signal-to-noise ratio,  $S/N$ , to the output  $S/N$  [SKOLb-62].

From this equation, the longer the range between the transmitter and the target, the higher the transmitted power, the antenna gain and the larger the area of the gathering aperture must be. However, in this basic equation, there are no system losses, other than path loss, and the statistical natures of many of the parameters are not included, to simplify the understanding. Due to the simplistic nature of the equation, certain parameters need to be more fully explained in order to understand the complexity of radar.

### 2.1.2.2 Transmitted Power:

The transmitted power considered in the general radar equation is the output power of the transmitter for a sine wave transmission. This is generally proportional to the maximum amplitude of a continuous wave (CW) signal [SKOLb-62]. However, in most modern uses of the radar, the transmitted signal is a pulsed transmission. Therefore, the peak transmitted power in the equation is often substituted by the average power for a pulse, given by:

$$P_{av} = \frac{P_t \tau}{T_r} = P_t f_r \tau \quad [2.12]$$

where  $f_r$  is the pulse repetition frequency (PRF) and  $\tau$  is the pulse width [HOVA-80]. The PRF of an imaging radar system is chosen so that the maximum range will be preserved and yet not allowing multiple echoes to confuse the image. This value for the average power is substituted directly into the radar equation as the transmitted power in applications where the pulse waveform is used instead of the continuous wave.

### 2.1.2.3 Minimum Detectable Signal:

The minimum detectable signal is the weakest signal that the receiver can detect given a predetermined probability of detection and the noise energy, which occupies the same bandwidth. Thus, the detection of a signal by the receiver is probabilistic in nature and will allow for changes in the power requirements based upon the requirements of detection. The threshold voltage, a predetermined voltage which, when achieved, assumes the presence of a target, is determined by the probabilities of detection and false alarm [SKOLb-62]. Combined with the signal is the receiver noise, consisting of thermal noise power and filter noise. The sum of these powers must produce a voltage greater than the threshold voltage for the signal to be detected.

When random noise is strong enough to cross the threshold value, a false target will be registered. It is therefore necessary to have a threshold value high enough to significantly limit the false-alarm probability. However, if the threshold value is set too high, then the

probability that weak signals will be detected becomes too low. A balance must be reached between the probability of detection and of false alarm.

In the specific case of the detection of a radar signal, the noise entering the system can be considered Gaussian with a density function of:

$$p(v)dv = \frac{1}{\sqrt{2\pi\psi_o}} e^{\frac{-v^2}{2\psi_o}} \quad [2.13]$$

where  $p(v)dv$  is the probability of finding the noise voltage between an envelope  $v$  and  $v+dv$  and  $\psi_o$  is the variance of the voltage of the received values. As this noise function is passed through the receiver, the probability density function transforms from a Gaussian form to a Rayleigh function, whose probability of detection above the threshold value as:

$$P(V_t < v < \infty) = \int_{V_t}^{\infty} \frac{v}{\psi_o} e^{\frac{-v^2}{2\psi_o}} dv = e^{\frac{-V_t^2}{2\psi_o}} = P_{fa} \quad [2.14]$$

where  $P_{fa}$  is the probability of a false alarm [SKOLb-62].

The choice of an acceptable false alarm probability is based upon the system requirements for the application and from this the threshold voltage can be determined. This voltage value cannot, however, be chosen arbitrarily to limit the false alarm probability, since it also limits the probability of detection of the signal, given by a similar Rayleigh probability-density function. Setting the threshold value to limit the probability of a false alarm will also lead to a limited sensitivity, with the consequent detection of very few of the returning echoes. Therefore, there is a compromise to be made so that the probability of detection is high enough to ensure complete data, yet the system can handle the related false alarms. This compromise is highly dependent upon the nature of the radar system and in most systems, it is the probability of detection which is the driving factor for determining the threshold voltage.

#### 2.1.2.4 Radar Cross Section (RCS):

The radar cross section (RCS) affects the power of the re-radiated signal. The smaller the RCS of the target, the weaker the back-scattered signal, thus resulting in a lower received signal. The RCS is the measure of the target's ability to reflect the radar signal back in the direction of the receiver, i.e. the measure of the ratio of backscatter power per unit of solid angle in the direction of the receiver to the power density that illuminates the target [SKOLb-62]. The RCS may also be represented by the target's complex amplitude pattern, containing both a real and imaginary component as a function of the angular frequency and position. In most applications, however, it is assumed to be constant, so is represented simply by  $\sigma$ . This is a valid assumption for a single pulse, even if the system is moving, as the RCS of the target does not change significantly over the pulse width. The RCS is, therefore, the product of the cross section area, the reflectivity and the directivity of the object. The value of many simple shapes, such as a sphere or a flat plane, can be easily determined experimentally or using Maxwell's equations. However, in operational situations, the target is rarely a simple shape with a single RCS. Rather it displays a combination of multiple RCSs.

The RCS is often replaced by the backscatter coefficient for remote sensing applications since the targets are often extended land features or terrain rather than point targets. This coefficient is defined as a relationship involving the dielectric constant of the surface, the roughness of the surface and the incidence angle of the signal [SKOLb-62]. It is a dimensionless coefficient, which is not directly dependent on the shape of the reflecting surface. It may be thought of as the RCS divided by the projected area of the target, i.e. facing the signal:

$$\sigma^o = \frac{\sigma_t}{A_t} \quad [2.15]$$

The  $\sigma_t$  and  $A_t$  terms are considered to be constants over the pulse width.

This becomes more apparent in remote sensing applications in which the RCS of an area defined by the resolution of the system is actually the combination of multiple RCS of individual objects in each differential area. In this case, there are a large, but finite number of individual radiating elements in each small area of the target. In each of these areas, the average backscattering coefficient for a given target is simply a statistical average of all the individual coefficients within the area divided by their individual ground areas:

$$\sigma^o = \left\langle \frac{\Delta\sigma_t}{\Delta A_t} \right\rangle \quad [2.16]$$

This represents the backscattering coefficient value that is used by the signal processor.

#### **2.1.2.5 System Losses:**

The RCS is not the only limiting factor for the received power. The losses in the transmitter, along the path of propagation, and at the receiver will also reduce the performance of the system. The values of system losses can be added into the denominator of the radar equation as a total system loss value, whose noise figure will always be greater than or equal to one, thereby showing that the loss will create noise.

The system introduces losses through the wave-guide, antenna characteristics, and receiver noise quality [SKOLb-62]. The wave-guide losses are caused directly from the wiring, transmission lines, receiver lines and connectors. These losses are typically small, unless the components are of poor quality or the frequency is extremely low. The loss due to the antenna characteristics is called the beam-shape loss, where non-optimal beam forming causes a reduction in the transmitted power in the desired direction. Limiting losses are caused by the limitation of the signal at the receiver due to the probability of detection as was described with the minimum detectable signal. Careful engineering and design control this loss.

The losses due to propagation effects are attenuation, multipath and refraction. Attenuation, the loss from absorption, is caused by the atmosphere, mainly in the

troposphere and ionosphere regions. The presence of moisture in the air, clouds, fog, rain, etc, causes some energy to be absorbed or reflected. This loss is highly dependent on the frequency of the signal. Multipath loss is caused by the reflection of a signal off multiple objects. The signal is therefore not received. The bending of the propagating waves by the atmosphere causes refraction loss. The changing of the refractive index of the propagating medium causes this error, causing the path traveled to change by slight values, making it non-linear.

#### **2.1.2.6 Measurements:**

Having now discussed the basic nature of the radar signal and the system performance, it may be determined what information is gained from the returned signal. As it's name suggests, the first radar systems were used as detection and ranging devices. In WWII, the Royal Air Force employed radar to detect the incoming enemy aircraft [FRAN-99]. It is still used today to control the airspace environment. The detection, however, is done by simply receiving an echoed signal strong enough.

The range information that comes from the radar equation is based upon the time of propagation from the transmitter to the target and back to the receiver. As can be seen from the basic nature of radar, the measurements of range and Doppler shift can be determined directly from the received echo signal. The time it takes for the signal to travel from the radar to the target and back to the radar,  $T$ , leads to the range determination equation:

$$R = \frac{cT}{2} \quad [2.17]$$

which states that the range to the target is half the time it takes for the signal to return to the transmitter multiplied by the speed at which the signal propagates through the medium, assumed here to be the speed of light through free space— $c \approx 3 \times 10^8$  m/s. This equation does not take into account any propagation effects, such as the change in refractive index, which slightly degrades the accuracy of the reading.

The accuracy of the measurement of the propagation time,  $T$ , is critical to achieving an accurate measurement of range, making an accurate clock a vital component of the radar system. Even small clock biases, considered to be in the microsecond range, can cause large distance errors, on the order of hundreds of metres.

Even considering these errors, the calculated range between the radar and the receiver does not give the position of the target. The equation establishes the distance between the radar and target, which actually places the target on a sphere surrounding the radar (assuming a omni-directional antenna—it would be a portion of a sphere for a directional antenna). Assuming the targets lie on a plane, this can be reduced to a circle. Therefore, for a radar range measurement, there exist isorange contours; concentric circles, creating ambiguity in the use of only time measurements for the determination of range. See Figure 2.1.

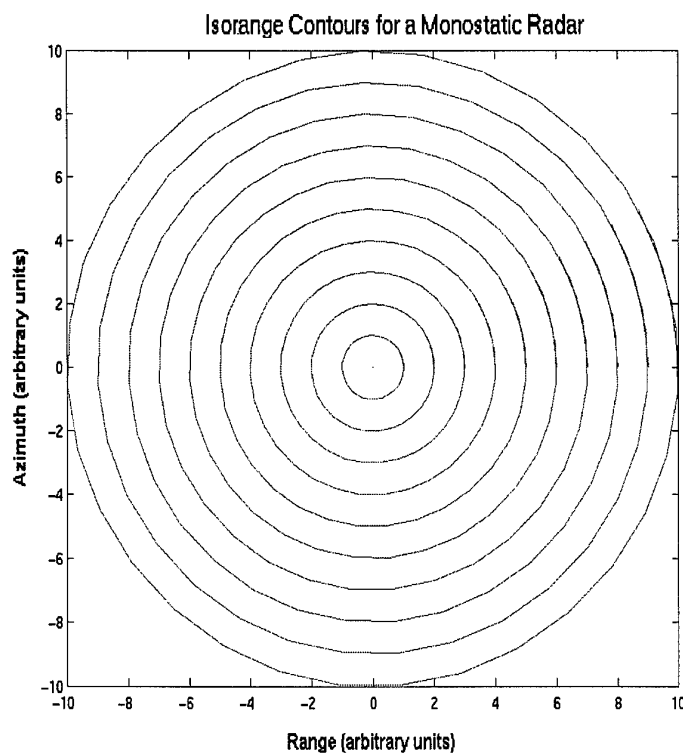


Figure 2.1 Isorange Contours



As explained above, the propagation time of the signal determines the range. However, the pulse is not infinitesimally small and this characteristic leads to a width of response. As the signal interacts with the target at a range  $R$ , there is not a single response, but a pulse response, equaling the width of the transmitted pulse. Therefore, the resolvable distance from the source to the target can only be found within the error of the length of the pulse. In addition, since there may be multiple targets within a distance defined by the error of the length of the pulse, their returns will be combined and cannot be individually resolved. This is known as the range resolution of the radar system.

The measurement of the Doppler frequency shift is slightly more complicated, but is necessary to resolve targets at equidistant ranges. The Doppler frequency shift depends upon the relative motion of the transmitter, the receiver, and the target. This correlates directly to the velocity of the radar, given that the target is stationary. The governing equation for this relationship is:

$$f_d = \frac{2v_r}{\lambda} \quad [2.18]$$

Therefore, by subtracting the transmitted frequency from the received frequency, to gain the Doppler frequency shift, it is possible to determine the relative velocity of the radar to the target,  $v_r$ . Consequently, if the velocity of the radar is known, it is possible to determine the azimuth contour of the target based on the Doppler frequency. These contours are represented in Figure 2.2.

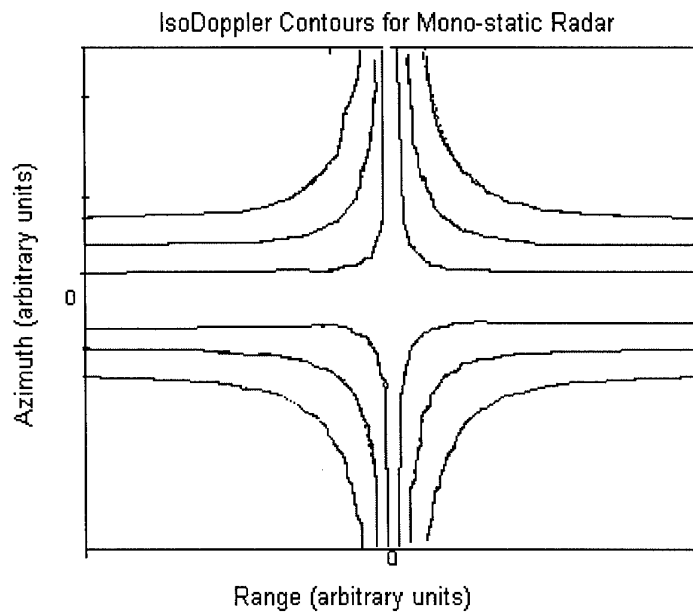


Figure 2.2 Iso-Doppler Contours

The two intersection points between the isorange and iso-Doppler contours are possible target positions—one to the left of centre and one to the right. This inability to resolve the information to a unique point is known as the left-right ambiguity. Left-right ambiguity is the inability to resolve two points equally spaced from the antenna centre of a downward looking radar as explained by Figure 2.1. A side-looking radar can solve this.

## 2.2 Imaging Radar:

Applying the theory of radar, the concept and principles of radar imaging are found. The governing principles are the same for real aperture radar and synthetic aperture radar (to be discussed later) with differences only in the signal processing of the returns.

### 2.2.1 Law of Reflection:

As a radar wave is incident on a surface, there is an amount of energy that is absorbed into the second medium, or refracted, and a portion that is reflected. It is the reflected, or more precisely the scattered energy, that is used in radar imaging. The law of reflection states that when a wave strikes a plane, smooth surface, the incident and reflected rays, and the normal to the reflected rays, are all coplanar and the angle of incidence is equal to the angle of reflection [BECKa-87]. See Figure 2.3a for a pictorial representation of the specular reflection. For a more general surface, the energy is also scattered, and some energy is “backscattered” towards the source.

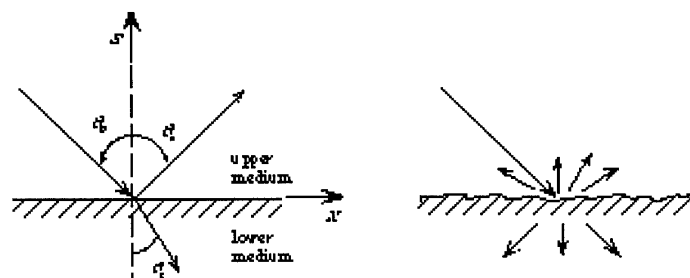


Figure 2.3a Reflected Energy    Figure 2.3b Scattered Energy

(adapted from: [www.csr.utexas.edu](http://www.csr.utexas.edu))

### 2.2.2 Microwave Scattering:

Detailed studies have been made into the basic principles of backscattered energy as used in radar and the signal and target parameters effects. Whenever an electromagnetic wave is incident to a surface, a portion of the energy is reflected back above the surface and the remainder is absorbed. When rough surfaces are involved, it is difficult to determine the normal to the surface since it changes rapidly with position. The reflection from a rough surface will appear scattered due to the varying normals. This roughness of the surface

causes the energy to scatter diffusely, where the total reflection is actually the sum of all reflections over the differing degrees of the normals. There is a portion of energy, which is perfectly reflected, but the majority is diffusely scattered energy and becomes the backscatter used in radar. Figure 2.3b shows this relationship.

The proportion of directly reflected energy to backscatter is determined by the roughness of the surface compared to the wavelength [BECKa-87]. A smooth surface will scatter almost all the energy coherently, while a “rough” surface will have almost no coherent scatter. The term “rough” is relative in that the surface must “appear” rough to the incident wavelength. As shown in Figure 2.4, even though the first surface is not perfectly smooth, it appears to be as the variations in the height of the surface is small compared to the wavelength and the energy is reflected. However, as the surface becomes rough enough to appear rough to the wavelength, the energy is reflected and backscattered. This is due to the assumption that a surface may be considered a collection of small particles. In order for a wave to strongly interact with these particles, they must be approximately 10% of the wavelength or larger. Therefore, at smaller wavelengths, surfaces will appear to be rougher than they are to longer wavelengths as the radiation interacts with more of the particles.

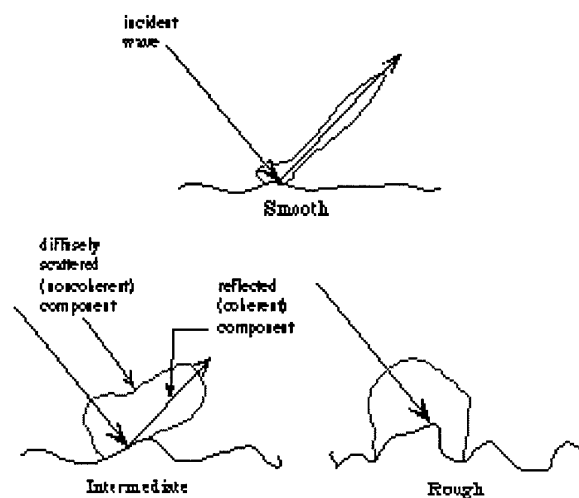


Figure 2.4 Relative Nature of Surface “Roughness”

(adapted from: [www.csr.utexas.edu](http://www.csr.utexas.edu))

However, the wavelength is not the only factor that determines the strength of the backscatter. The incidence angle also contributes to the backscatter energy. The incident angle is the angle from the local surface normal to the propagation vector of the incident beam [BECKa-87]. Figure 2.5 shows the general relationships, i.e. not to scale, between the incident angle and the backscatter coefficient.

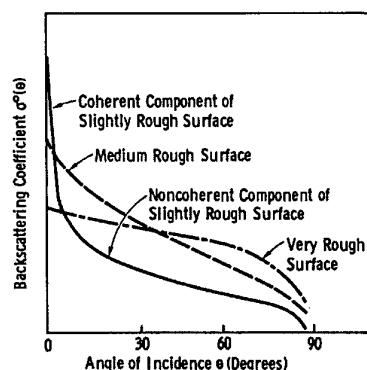


Figure 2.5 Backscattering Coefficient with Respect to Incidence Angle

(not to scale)

(adapted from: [www.csr.utexas.edu](http://www.csr.utexas.edu))

### 2.2.3 Imaging Geometry:

This scattering theory becomes useful when applied to the geometry of an imaging radar system. The imaging geometry is shown in Figure 2.8, where the antenna-illuminated surface is called a footprint. The radar beam is typically angled to the surface, called side-looking radar, as opposed to the nadir system to eliminate the left-right ambiguity of two points. This can be seen in Figure 2.7.

The swath width of a radar is given by:

$$S \cong \frac{\lambda h}{l \cos^2 \theta_i} = \frac{h \beta_i}{\cos^2 \theta_i} \quad [2.19]$$

where the  $\beta$  is the beam width in elevation,  $l$  is the width of the antenna,  $\theta_i$  is the look angle from beam centre and  $h$  is the height of the radar system. Figure 2.6 offers a pictorial representation of this geometry.

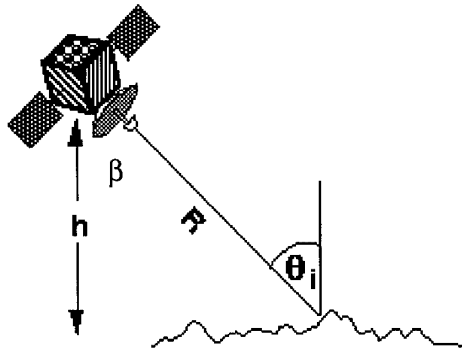


Figure 2.6 Imaging Geometry  
(adapted from: [www.southport.jpl.nasa.gov](http://www.southport.jpl.nasa.gov))

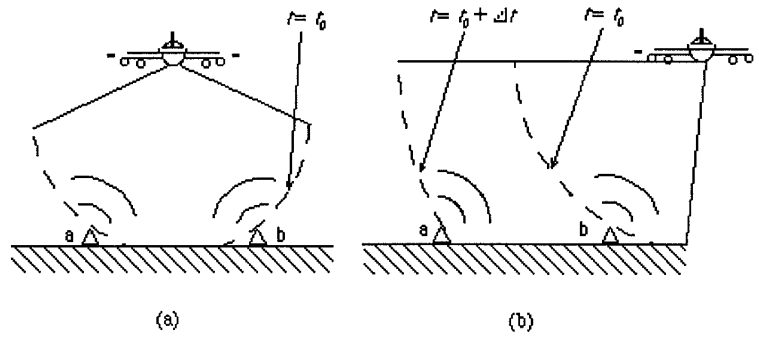


Figure 2.7 Left-Right Ambiguity Problem  
(adapted from: [www.csr.utexas.edu](http://www.csr.utexas.edu))

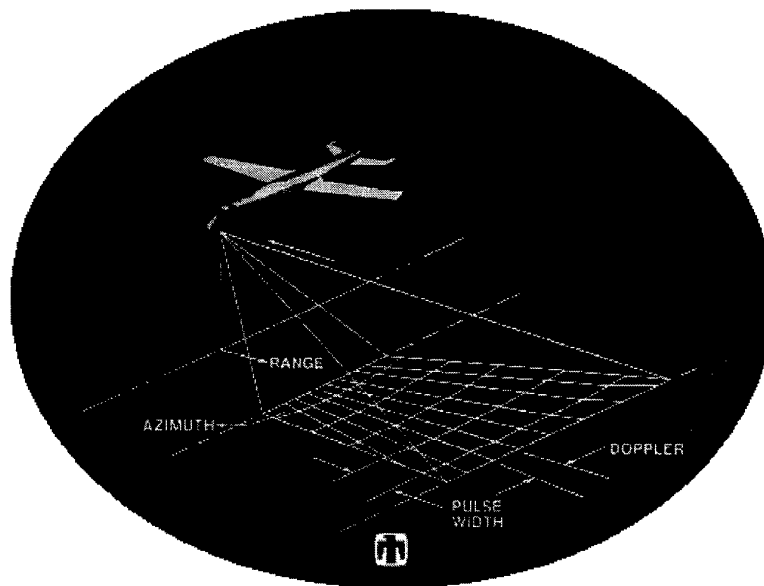


Figure 2.8 Image Geometry  
(adapted from: [www.scandia.gov](http://www.scandia.gov))

#### 2.2.4 Signal Characteristics:

To explain the signal characteristics of the radar system, the focus must be on the four basic characteristics of a pulsed waveform: carrier frequency, pulse width, modulation and pulse repetition frequency [SKOL-70]. The carrier frequency is the centre frequency of the sinusoidal wave within the pulse during transmission. The pulse width is the duration of the pulse described in time. This is an important characteristic as it determines the range resolution of the system. Intra-pulse modulation is any modulation technique applied to the carrier signal within the pulse. Pulse repetition frequency is the rate at which the radar transmits pulses. The advantage of pulsed transmission is the reduction of noise at the receiver, which can be isolated from the transmitter while remaining on the same platform by receiving only when the radar is not transmitting.

### **2.2.5 Image Formation:**

The principles of radar previously discussed, also form the theoretical basis for imaging radar. It is only necessary, therefore, to explain the process of forming an image from the received echoes to complete the theory. Imaging radar works very much like a flash camera, where the radar provides its own illumination source and records the reflection [JPL-01].

The radar image itself is composed of many pixels, which represent the radar backscatter from a corresponding target or targets. For simplification of this explanation, the target is assumed as a flat portion of the Earth. Each pixel is then defined by the information within the echo response from the corresponding small area on the surface.

The system transmits a pulse, which interacts with the target, or targets, and the echo is received. This echo contains the information needed to reconstruct the image. The range of the target from the radar system is found from the time delay of the returned echo. This places the target on an isorange contour.

The relative velocity of the radar system to the target is then used to place the response within a single pixel on the image plane. As defined in section 2.4.3, the system is side looking, which allows for the iso-Doppler contour to intersect with only one isorange contour at a unique point, corresponding to a single pixel in the image.

Finally, the intensity of the backscatter is used to apply a brightness to the pixel. The amplitude of the echo response is determined by the system and translated to a grey level, usually based upon 256 levels. The higher the amplitude of the signal, the greater the backscatter and the lighter the shade of grey.

This information is gathered for each pixel within the image and once complete, an image of the target is produced. The detail of the image depends directly upon the pixel size, as defined by the resolution of the system.



### 2.2.6 Resolution:

Resolution is used to define the quality of the picture, or the detail that is gathered within the image. For a radar system there is resolution in the range direction and the azimuth direction. Figure 2.9 represents the resolution cell.

Range resolution is the minimum distance between two scatterers on the surface to be separated in terms of differing delay times. Since the distance between two objects in radar is determined by the time difference of the signal returns, the smallest discernable time difference is given by the pulse width [SKOL-70]. Therefore, the range resolution is:

$$X_r = \frac{c\tau}{2\sin\theta} \quad [2.20]$$

where  $\tau$  is the pulse width,  $c$  is the speed of propagation and  $\theta$  is the look angle of the radar measured from the vertical axis (see Figure 2.9). Therefore, this is the ground resolution, rather than the slant range resolution.

In the azimuth direction, resolution is the closest distance between two points that may be determined along a constant delay line. For real aperture radar, this is equal to the width of the footprint, as the echoes from points along a line spanning the width are undetermined in time [SKOL-70]. The azimuth resolution is given by:

$$X_a = \frac{h\lambda}{l\cos\theta} \quad [2.21]$$

where  $l$  is the length of the radar aperture in the azimuth direction,  $h$  is the height of the radar, and  $\lambda$  is the wavelength. From this equation, it can be seen that if the wavelength is very small or the aperture size,  $l$ , of the system is large, then the azimuth resolution will be very fine. There is, however, a limit to the size of aperture that can be used. This led to the development of synthetic aperture radar, which uses a combination of multiple looks to synthesize a large aperture, and therefore achieve a finer azimuth resolution.

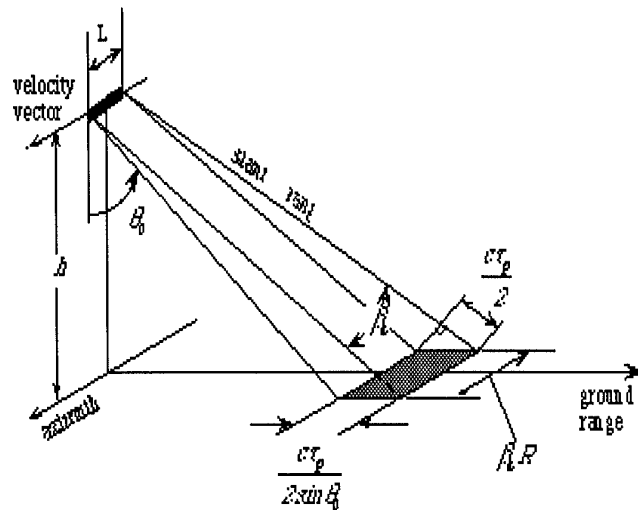


Figure 2.9 Resolution Cell

### 2.3 Bi-static Radar:

Given the principles of the mono-static radar system, the equations can be extended to a bi-static system. Bi-static radar uses a separate site for the transmitter and the receiver. This changes the geometry of the radar system from a line between the radar and the target to a triangle. Figure 2.10 shows the geometric relationship of a bi-static radar system.

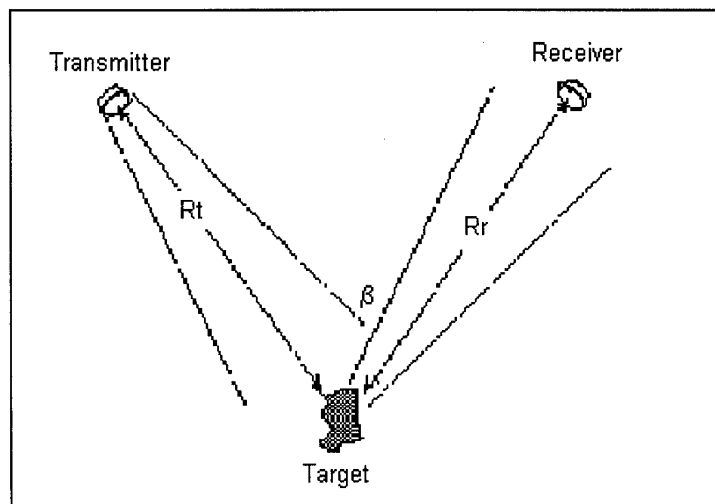


Figure 2.10 Bi-static Radar Geometry

(Adapted from: [www.csr.utexas.edu](http://www.csr.utexas.edu))

The local coordinate system at both the transmitter and the receiver must be based on the same principal direction. In the case of space-based radar, the main axis is nadir pointing, assuming a flat Earth. In operational systems where this is not true, the principal axis are set parallel and angle errors are corrected during signal processing.

The changes made to mono-static radar for bi-static systems are based solely upon the differing geometry [WILLa-91]. All other parameters can be considered identical. The radar range equation for bi-static radar is similar to that of mono-static, only, where the range was a single value for mono-static systems, it becomes the addition of the range from the transmitter to the target,  $R_t$ , and the target to the receiver,  $R_r$ . The following equation is known as the bi-static radar equation:

$$(R_T R_R)_{\max} = \left( \frac{P_T G_T G_R F_T^2 F_R^2 \lambda^2 \sigma_b}{(4\pi)^3 k T_s B_N \left( \frac{S}{N} \right)_{\min}} \right)^{\frac{1}{2}} \quad [2.22]$$

where the F is the factor of propagation. There are separate factors in a bi-static system due to a separate transmitting and receiving antennas and the propagation path being different. The antenna pattern factor is the relative strength of the free-space field radiated by the antenna as a function of the pointing angles of azimuth and elevation. The propagation factors include multi-path, diffraction and refraction. The atmospheric losses and antenna system losses can be combined in the loss factors,  $L_R$  and  $L_T$ , for the receiver and transmitter, respectively and added to the equation.

$$(R_T R_R)_{\max} = \left( \frac{P_T G_T G_R F_T^2 F_R^2 \lambda^2 \sigma_b}{(4\pi)^3 k T_s B_N \left( \frac{S}{N} \right)_{\min} L_T L_R} \right)^{\frac{1}{2}} \quad [2.23]$$

Like the mono-static system, bi-static radar also exhibits the isorange contours. However, instead of concentric circles centred on the radar system, bi-static isorange contours are confocal ellipses where the transmitter and receiver positions are the foci

[WILLb-91]. If one considers the mono-static case to be a bi-static radar with co-located foci, then the result is circular contours, as shown in Figure 2.1. Thus, it is simple to picture the effect of the separation of the transmitting and receiving antennas on the isorange con

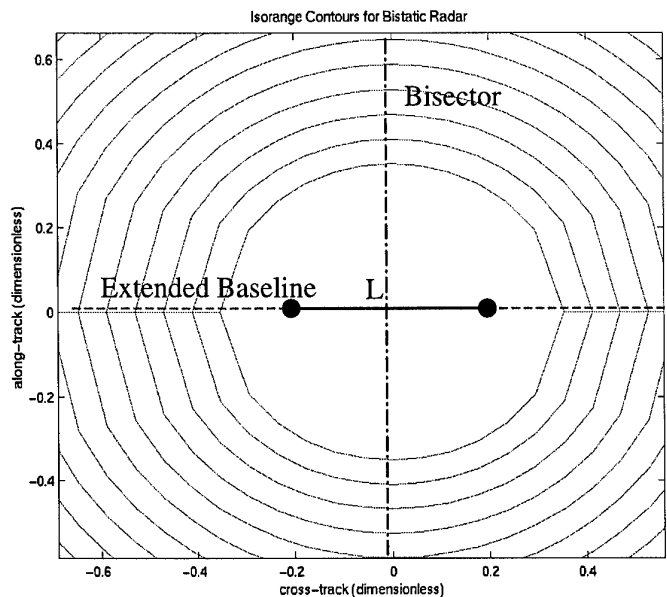


Figure 2.11 Bi-static Isorange Contours

### 2.3.1 Range Cells:

The concept of a range cell is derived from the unique relationship between confocal ellipses of the isorange contours. Also known as range resolution cells, the separation of isorange contours in a bi-static system is not constant as it is in mono-static radar, as the distance between confocal ellipses varies from a minimum at the extended baseline,  $L$ , to a maximum at the perpendicular bisector of the baseline (which has a value equivalent to the mono-static range cell value). An accurate estimate for the range cells is given by the equation:

$$\Delta R_B = \frac{c\tau}{2\cos\left(\frac{\beta}{2}\right)} \quad [2.24]$$

where  $\beta$  is the bi-static angle, measured at the target, and  $\Delta R_B$  is the range cell size in metres.

This concept becomes important in the discussion on the signal processing of radar information and the consequent pixel size that is derived from the resolution.

### 2.3.2 Ovals of Cassini:

Also useful in performance analysis of the bi-static radar is the determination of the maximum range with respect to the S/N using the Ovals of Cassini [WILLb-91]. Ovals of Cassini are described as the locus of the vertex of a triangle when the product of the sides adjacent to the vertex is a constant and the length of the side opposite the vertex is fixed. This concept applies to bi-static radar systems, as the fixed position of the transmitter with respect to the receiver gives a fixed length,  $L$ , and the locus defines a maximum range given a specific S/N.

From these ovals, the S/N is given by:

$$\left(\frac{S}{N}\right) = \frac{K}{\left(r^2 + \frac{L^2}{4}\right)^2 - r^2 L^2 \cos^2 \theta} \quad [2.25]$$

$$K = \frac{P_T G_T G_R F_T^2 F_R^2 \lambda^2 \sigma_b}{(4\pi)^3 K T_s B_N L_T L_R}$$

and are given in polar coordinate format, where  $r$  is the distance to the target from the origin of the system,  $L$  is the baseline and  $\theta$  is the angle between baseline,  $L$ , and  $r$ . The origin of the system is the bisector of baseline.

### 2.3.3 Target Location:

Similar to the relationship of the parameters of a bi-static system to a mono-static system, the method by which information is gained from the bi-static system can be derived from the mono-static case. Following the basic range solution of using the time difference of transmission and reception as a means to determine the two-way propagation distance, the separation of the antennas creates another level of complexity. This complexity is the

need to know, to a high degree of precision, the position of the transmitter and the distance between the transmitter and the receiver. While relatively easy to achieve for stationary platforms, it can be extremely difficult to obtain accurate values for moving platforms, such as satellites.

The location of the target can be determined by its range from the receiving site, with the position of the transmitting site being actively sent to the receiver by the transmitter and the distance between the two sensors,  $L$ , measured by the receiver. The equation for the range from the target to the receiver is given by:

$$R_R = \frac{(R_T + R_R)^2 - L^2}{2(R_T + R_R + L \sin \theta_R)} \quad [2.26]$$

where the range sum,  $R_T + R_R$ , is measured by the delay time of the signal and  $\theta_R$  is the angle between the local vertical and the receiver range vector,  $R_R$ , measured at the receiver [WILLb-91]. The assumption of a flat Earth is still valid. This can be done either directly or indirectly by the following equations:

$$\begin{aligned} R_T + R_R &= c\Delta T_{RT} + L \\ R_T + R_R &= c\Delta T_{TT} \end{aligned} \quad [2.27]$$

where  $L$  is the baseline between the transmitter and the receiver,  $\Delta T_{RT}$  is the delay time between the reception of the transmitted signal and the received echo and  $\Delta T_{TT}$  is the total time delay from the transmitter to the receiver.

The errors in the range determination are due to errors in the range sum measurement, the baseline measurement or the angle of reception measurement and are given by:

$$\begin{aligned}
dR_R &= \sqrt{\left(\frac{\delta R_R}{\delta(R_T + R_R)} \times \delta(R_T + R_R)\right)^2 + \left(\frac{\delta R_R}{\delta(L)} \times \delta(L)\right)^2 + \left(\frac{\delta R_R}{\delta\theta_R} \times \delta\theta_R\right)^2} \\
\frac{\delta R_R}{\delta(R_T + R_R)} &= \frac{1 + e^2 + 2e \sin \theta_R}{2(1 + e \sin \theta_R)^2} \\
\frac{\delta R_R}{\delta(L)} &= \frac{(e^2 + 1) \sin \theta_R + 2e}{2(1 + e \sin \theta_R)^2} \\
\frac{\delta R_R}{\delta\theta_R} &= \frac{L(1 - e^2) \cos \theta_R}{2(1 + e \sin \theta_R)^2} \\
e &= \frac{L}{R_T + R_R}
\end{aligned} \tag{2.28}$$

where  $e$  is the eccentricity of the isorange contours [WILLb-91].

It may be seen that as the baseline of the system,  $L$ , approaches the range sum value, its effect increases and vice versa. Therefore, with a small baseline, compared to the range, the errors in baseline measurements can be neglected. However, when treated like a thinned array, changes in  $L$  of the order of the magnitude of wavelengths cause phase errors that degrade the array effectiveness. This will become a determining factor in the performance of a bi-static satellite system.

#### 2.3.4 Synchronization:

As stated above, within the bi-static system, the transmitter and receiver are no longer co-located. Therefore, the two sites must be time and phase synchronized [BOVE-87]. Time stability must be accomplished within a fraction of the transmitter's compressed pulse width, usually a few nanoseconds. This can be accomplished directly by receiving a signal from the transmitter and using it to synchronize the receiver clock. If the pulse repetition interval is stable, then the time synchronization may be accomplished indirectly by using stable clocks at both the transmitter and the receiver and matching them only periodically or by slaving both the transmitter and receiver clocks to an outside clock. Another means of indirect clock synchronization is to slave both clocks off a second source such as GPS [WILLd-91].

Phase synchronization may be accomplished by similar methods—directly, by phase locking the receiver to the transmitted signal or indirectly, by using matched local oscillators and synchronizing them periodically [WILLc-91]. The errors introduced by the synchronization process of the system are inherent in the bi-static system and must be limited to acceptable levels based on the needed performance of the system.

### 2.3.5 Doppler Relationships:

With the extraction of the time-based range information and range errors explained, the next step is to determine the effect of the bi-static geometry on the Doppler frequency shift. Within the context of bi-static radar, the Doppler shift frequency is:

$$f_{DB} = \frac{1}{\lambda} \left( \frac{dR_T}{dt} + \frac{dR_R}{dt} \right) \quad [2.29]$$

where the time rates of change are the sums of all velocities adding to the perceived motion of the sensors. For stationary targets with a moving transmitter and receiver, the above equation can be simplified to:

$$f_{DB} = \frac{V_T}{\lambda} \cos(\delta_T - \theta_T) + \frac{V_R}{\lambda} \cos(\delta_R - \theta_R) \quad [2.30]$$

where  $\delta$  represents the angle between the local vertical axes of the transmitter and receiver and the velocity vector and  $\theta$  is the angle between the local vertical of the transmitter and receiver and the target [WILLc-91].

If the target is moving as well as the transmitter and receiver, the total value of the shift is:

$$f_{TTR} = \frac{V_T}{\lambda} \cos(\delta_T - \theta_T) + \frac{V_R}{\lambda} \cos(\delta_R - \theta_R) + \frac{2V}{\lambda} \cos \delta \cos(\beta/2) \quad [2.31]$$

where the values of the last term are associated with the target values.

With this determination of the Doppler shift, combined with the range value, the location of a target may be determined. The velocities of the transmitter, receiver and target must



all be taken in the same frame, usually an Earth-fixed frame, thereby neglecting the rotation of the Earth. Figure 2.12 shows the relationship of the iso-Doppler contours to the isorange contours in a bi-static system. It can be seen from the relationship that the same left-right ambiguity exists in bi-static as mono-static systems.

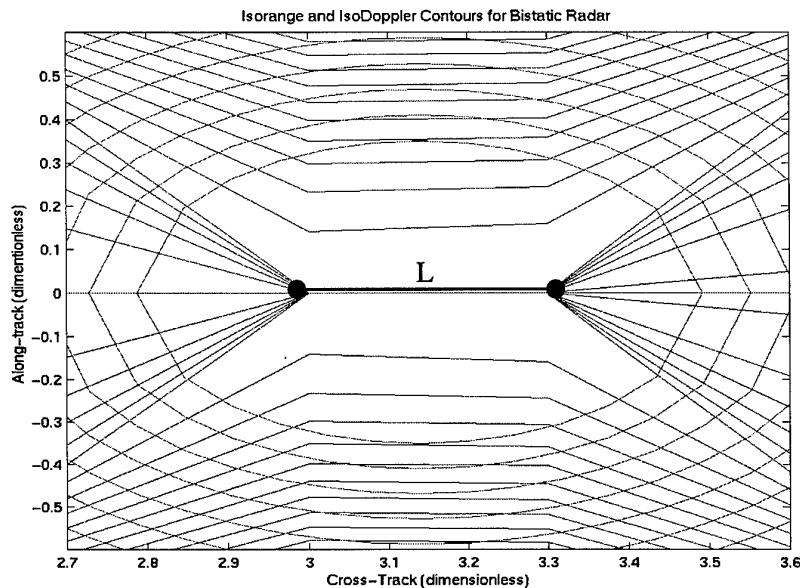


Figure 2.12 Iso-Doppler and Isorange Contours for Bi-static Radar

### 2.3.6 Resolution:

The final system performance factor for a bi-static system is, like the mono-static system, the quality of the image, i.e. resolution. As previously stated, the value for the range cells is given by:

$$\Delta R_B = \frac{c\tau}{2 \cos\left(\frac{\beta}{2}\right)} \quad [2.32]$$

where  $\beta$  is the bi-static angle as shown in Figure 2.13, and  $\tau$  is the propagation time. This may also represent the range resolution of the bi-static system for all targets whose line joining them together is collinear with the bi-static bisector. When this is not the case, the range resolution becomes:

$$\Delta R_B = \frac{c\tau}{2 \cos\left(\frac{\beta}{2}\right) \cos \psi} \quad [2.33]$$

where  $\psi$  is the angle between the bi-static bisector of target 1 and the line joining target 1 to target 2 [WILLc-91]. See Figure 2.13.

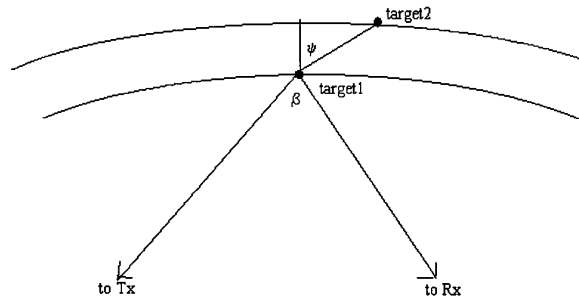


Figure 2.13 Bi-static Resolution

Similar to range resolution, the Doppler, or azimuth, resolution of a bi-static system is the minimum discernable distance between two targets is given by:

$$\Delta R_a = \frac{\lambda}{2L_{eff} \cos\left(\frac{\beta}{2}\right)} \quad [2.34]$$

where  $L_{eff}$  is the effective aperture length,  $\beta$  is the bi-static angle and  $\Delta\theta_R$  is the difference between the reception angle of the two targets.

## 2.4 Synthetic Aperture Radar:

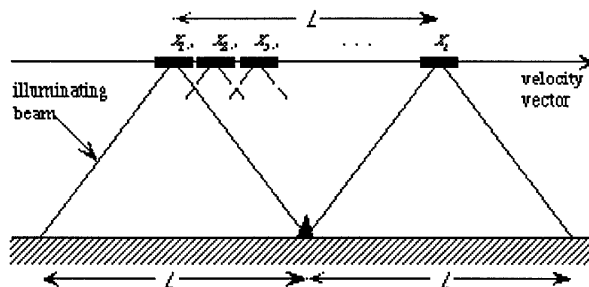


Figure 2.14 SAR Concept

### 2.4.1 Benefits of SAR:

The basic premise behind SAR as an active, coherent imaging system is to achieve enhanced spatial resolution in the azimuth direction by exploiting the motion of the radar platform to synthesize an aperture of large dimensions, as the actual aperture size is limited. Therefore, the most obvious benefit to using SAR as a means of radar imaging is the increase in azimuth resolution.

However, there is an added benefit to the use of SAR over simple linear arrays in that, linear arrays are focused to a specific range. This is typically done at infinity so that linear arrays are considered “unfocused.” In synthetic aperture, the focusing of each range can be achieved by separately adjusting the phase of each of the received signals before summation. Therefore, the complexity of a synthetic aperture system comes not from the physical elements of the system, but rather the signal processing, reducing the effect of system errors.

### 2.4.2 SAR Geometry:

To begin a discussion on SAR, the geometry of the system must be explained. Designed to be a side-looking radar system, single snapshot geometry of a SAR system is given by

Figure 2.14 and 2.15. The ground swath in the cross-track direction and the angular spread in the along-track direction determine the footprint of the radar. This differs from the nadir pointing system in which the footprint is determined by the beam width. The following equations are used to find the size of the individual radar footprint:

$$W_g = \frac{\lambda R_s}{l \cos \theta}$$

$$W_h = \frac{\lambda}{l} R_s$$
[2.35]

where  $W_g$  is the ground range swath width,  $W_h$  is the ground azimuth swath width,  $\lambda$  is the wavelength,  $R_s$  is the slant range from the antenna to the midpoint of the swath,  $h$  is the height of the antenna,  $\theta$  is the look angle of the system and  $l$  is the physical length of the antenna in the along-track direction [FRAN-99].

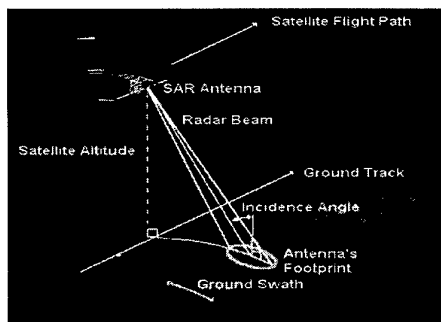


Figure 2.15 SAR Geometry

The angular spread in the along-track direction is also known as the maximum effective length.

This geometry only works when it is assumed that the Earth is flat. This cannot be done for space borne SAR. Conversion between calculated values for the flat-Earth assumption and space borne radar equations can be accomplished by the following relations:

$$\begin{aligned}
R_o &= (R_E + h) \frac{\sin \gamma}{\sin \theta} \approx (R_E + h) \frac{\gamma}{\sin \theta} \\
R_o^2 &= R_E^2 + (R_E + h)^2 - 2R_E(R_E + h) \cos \gamma \\
R_g &= R_E \gamma \\
\gamma &= \theta - \alpha \\
\sin \alpha &= \frac{R_E}{R_E + h} \sin \theta
\end{aligned} \tag{2.36}$$

where  $R_o$  is the slant range found by the time delay,  $R_g$  is the equivalent ground range,  $R_E$  is the Earth's radius,  $h$  is the altitude of the satellite,  $\gamma$  is the Earth central angle,  $\alpha$  is the look angle and  $\theta$  is the relative Earth angle [CURLa-91]. The geometry can be found in Figure 2.16. This will affect the range and azimuth swath widths leading to the equations:

$$\begin{aligned}
W_g &= \frac{\lambda(R_E + h) \frac{\gamma}{\sin \theta_E}}{l \cos \theta} \\
W_h &= \frac{\lambda}{l} (R_E + h) \frac{\gamma}{\sin \theta_E}
\end{aligned} \tag{2.37}$$

where the look angle  $\theta$  is slightly distorted from the angle when the Earth was assumed flat.

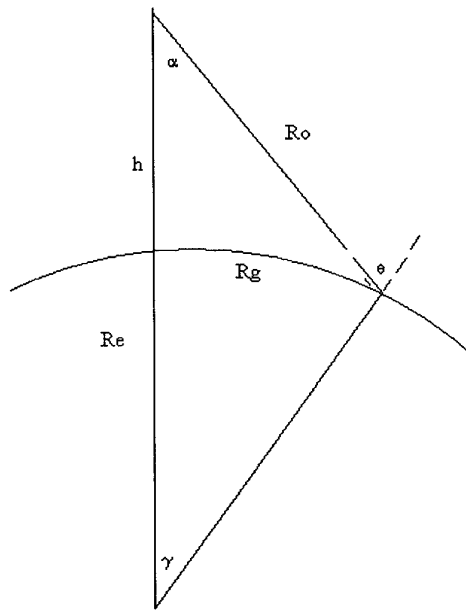


Figure 2.16 Geometry of a Curved Earth

### 2.4.3 SAR Modes:

Having explained the general geometry of SAR, it is necessary to explain the differences in two main modes of operation—Spotlight and Stripmap. While the general geometry remains the same, the differences in the illumination patterns requires slightly different signal processing methods.

Spotlight SAR is named because the antenna beam is steered, either electrically or mechanically, to remain pointed at only one area throughout the synthesized array time. This creates a linear array of returns, which have a similar scene centre and simply “look” at the scene from differing angles [STIMc-98]. This application offers a finer azimuth resolution than strip map mode. Also, with the subsequent imaging of the same scene from differing angles, it is possible to construct a more realistic three-dimensional scaled model of the scene. Figure 2.17 represents a spotlight SAR system.

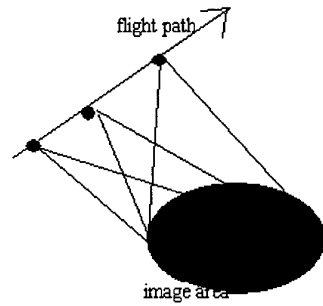


Figure 2.17 Spotlight SAR

In the traditional stripmap mode of SAR, the antenna pointing is fixed, and the radar actually images a long strip of ground rather than a single scene [STIMc-98]. The benefit of this mode is the lower complexity of the system and the reduction of the beam-pointing error distortion. In addition, this method is more useful for general remote sensing or Earth mapping applications, where large areas need to be imaged. Figure 2.15 represents a strip map mode SAR system.

## 2.4.4 Signal Properties:

### 2.4.4.1 Transmitted Signal:

As SAR involves the exploitation of signal processing, an analysis of the signal must accompany the geometry. The signals used in SAR systems are identical to the real aperture radar. For this study, the signal will be considered as a chirp pulse of an active radar system. This results in a signal:

$$p(t) = a(t) \cos \left( \omega_o t + \frac{\Delta \omega}{2\tau} t^2 + \phi_o \right) \quad [2.38]$$

where  $\tau$  is the pulse time, the pulse can be compressed at reception with delay lines. In this equation,  $\omega_o$  is the related angular frequency of the carrier,  $\omega = 2\pi f$ .

The common form of the transmitted waveform for a radar system is that of a “chirp”—a linear frequency modulated transmission. The frequency within the transmitted pulse is

increased at a constant rate throughout the length of the pulse. The principle of pulse compression was introduced to solve the dilemma of the need for both a long pulse for a higher energy and the desire for a short pulse for fine resolution. The pulse can be compressed at its reception into a smaller pulse width, thus increasing the system's resolution while maintaining a high energy. This is done by passing the received echo through a digital delay filter, which introduces a time lag, e.g. delays higher frequencies more than lower frequencies. At the output of this filter, the successive portions bunch together, increasing the amplitude, but decreasing the pulse width [STIMa-98]. Closely spaced targets, whose echoes are merged at the input of the filter, are fully resolvable at the output due to the compression. See Figure 2.18.

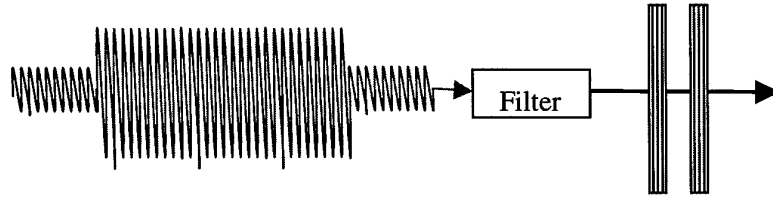


Figure 2.18 Pulse Compression [STIMa-98]

Given that a continuous wave radar signal can be represented by the sinusoidal function:

$$v(t) = A \sin(\omega_o(t - \tau)) \quad [2.39]$$

a frequency modulated pulse is:

$$v(t) = A \cos(\omega_o t + \frac{\Delta\omega}{2\tau} t^2) \quad [2.40]$$

where  $\omega_o$  is the frequency at the start of transmission,  $\Delta\omega$  is the spread of the frequency,  $t$  is the time from the start of transmission and  $2\tau$  is the total pulse length.

The amount of compression is given by the equation:

$$\frac{\tau'}{\tau_o} = \tau' \frac{\Delta\omega}{2\pi} \quad [2.41]$$

where  $\tau'$  is the compressed pulse width,  $\tau_o$  is the actual pulse length, and  $\Delta\omega$  is the frequency spread from the start to the end of the pulse [CURLa-1991].



#### 2.4.4.2 Average Power Requirements:

In the discussion of the radar equation, the power used was the power output from the transmitter. This power is defined as the power level of the individual pulse from beginning to end and determines the voltages, which must be applied to the transmitter.

As previously stated, the returned echoes from a SAR system are coherently added in the signal processing. The average power of a transmitted pulse train is the averaged power over the inter-pulse period. This is the power used to determine the initial power supplied to the transmitter.

To determine the average power, the number of pulses that will be added is found by the PRF and the synthetic array time, T:

$$f_r T = \frac{f_r R \lambda}{l V \sin \theta} \quad [2.42]$$

where  $l$  is the actual aperture length,  $f_r$  is the PRF,  $\theta$  is the incident angle, and  $V$  is the platform velocity [HOVA-80]. If this value is multiplied by the S/N per pulse:

$$\frac{S}{N} = \frac{P_t G_t G_r \lambda^2}{(4\pi)^3 R^4 k T B L} \left( \frac{l c \tau \sigma_o}{4 \cos \theta} \right) \left( \frac{f_r R \lambda}{l V \sin \theta} \right) \quad [2.43]$$

where  $L$  is the losses,  $\tau$  is the pulse width, and  $\theta$  is the incident angle. By expressing the average power of the signal in terms of the peak power, pulse width and the inter-pulse period, the average power required is found by the equation:

$$\bar{P} = \frac{(4\pi)^3 R^3 k T L}{G_t G_r X_r \cos \alpha \lambda^2 \sigma_o} \left( \frac{2V}{\lambda} \right) \left( \frac{S}{N} \right) \sin \theta \quad [2.44]$$

having replaced  $\frac{c\tau}{2}$  with  $X_r$ , the range resolution, and the pulse width with the inverse of bandwidth. This is the required average power for the given range resolution [HOVA-80]. It is important to realize that when using pulse compression, the resolution may be increased without increasing the transmitted power. This does not, however, reduce the average power requirement, but simply allows more average power to be transmitted due to the longer pulse and then later compressed to increase the range resolution.

#### 2.4.4.3 Echo Signal:

After the transmitted signal interacts with the target, the amplitude and phase are used to reconstruct the image in a similar way to that of real aperture radar imaging.

Given that a target is at a slant range,  $R$ , from the radar, the received echo signal is the transmitted signal in Equation 2.38 with a time and phase delay:

$$p\left(t - \frac{2R}{c}\right) = a(t - \tau)\sigma \cos\left(\omega_o\left(t - \frac{2R}{c}\right) + \frac{\Delta\omega}{2\tau}\left(t - \frac{2R}{c}\right)^2 + \phi_o\right) \quad [2.45]$$

where  $\sigma$  is the RCS of the target. This is the idealized return signal from a single point scatterer [STIMa-98].

In real applications, there is usually not a single scatterer within the view of the radar. For example, terrain is often considered as the combination of a near infinite number of individual scatterers. For this reason, the echo signals returned within the same range cell are added together to result in a single expression to represent all the scatterers within that cell. If this idea were considered in context of resolution, it would seem logical that the signal from an object will combine with other signals from objects within the resolution area, since the resolution is defined as the minimum distance between two points for their signals to be resolvable. Scattering elements that are separated by a distance less than the resolution are not distinguishable and the responses will be summed together.

As in real aperture radar imaging, the echo signal contains the data needed for image processing. The contribution of the time delay to determine the range,  $R$ , from the aperture to the target has already been discussed.

The azimuth component is found through the Doppler frequency shift history. Each returned echo from a cell, while it is within the swath width, will be shifted a certain Doppler frequency, which is directly proportional to the radial component of the relative

velocity. Therefore, each cell will have a different shift due to the slightly different speeds, based on the slightly different angles with respect to the track of the radar. This provides a second coordinate, the first being the range, relative to a point directly beneath the radar. This provides a localization of the point in two dimensions.

The amplitude of the signal is converted into a voltage, which is used directly for each pixel, rather than used as a history. As the signal is received, the amplitude is measured and is stored for each pixel element in the scene. This intensity is then used to determine the level of light and dark of the image pixel.

#### **2.4.4.4 Speckle and Clutter:**

In conjunction with the echo signal, it is necessary to mention the signal responses that limit the quality of the image. Speckle is the noise-like quality of coherent imaging. In SAR, this arises due to the true scattering properties of the Earth's surface. Ideally, each range cell would have one signal. In truth, each resolution cell contains a large number of discrete scattering elements. As the wave interacts with the surface, each scattering element contributes a backscatter wave with a certain phase and amplitude. As the backscatter echo of each individual element is added, there are interference effects because of phase differences, which degrade the quality of the image with speckle [BURD-68]. This phenomenon does not change resolution, but decreases the clarity of the image.

Clutter is comparable to speckle in that it can degrade the image quality, but it arises not from the various scattering elements per resolution cell, but from the extension of features across multiple cells [BURD-68]. This causes unwanted echoes to combine with the desired signal and change the intensity of the returning echo, degrading the image quality.

### 2.4.5 Resolution:

For a general figure on resolution refer to Figure 2.9. There is no increase in range resolution from SAR imaging, i.e. the slant range resolution is identical to that of real aperture imaging:

$$X_r = \frac{c}{2B} \quad [2.46]$$

where B is the bandwidth of the signal. Since the particular aim of this project is satellite based SAR systems, it is important to include the curvature of the earth as a factor in the resolution. Therefore, using Figure 2.16 to explain the geometry of a curved earth, the ground resolution becomes:

$$\begin{aligned} \frac{r_g}{r_s} &= \frac{dR_g}{dR_o} = \frac{R_o}{(R_e + h) \sin \gamma} = \frac{1}{\sin \theta} \\ X_r &= \frac{c}{2B \sin \theta} \end{aligned} \quad [2.47]$$

where  $r_g$  is the ground range resolution and  $r_s$  is the slant range resolution.

The improvement in azimuth resolution is the main benefit from SAR. In conventional radar theory, resolution can be approximated by:

$$X_a = \frac{\lambda R}{l} \quad [2.48]$$

where  $l$  is the aperture length, R is the radar range, and  $\lambda$  is the wavelength. This is, in effect, the half-power beam width multiplied by the range, as was discussed in the conventional radar resolution.

In SAR, the half-power beam width,  $\beta$ , is given by:

$$\beta_{eff} = \frac{\lambda}{2L_{eff}} \quad [2.49]$$

where  $L_{eff}$  is the effective length of the synthetic aperture. This can be found by determining the horizontal beam at a range  $R$ , which gives the maximum value for the length of the synthetic aperture that can be used. Therefore,  $L_{eff}$  is:

$$L_{eff} = \frac{R\lambda}{l} \quad [2.50]$$

where  $l$  is the length of the real aperture.

Applying these equations to the definition of azimuth resolution gives:

$$X_a = R\beta_{eff} = R \frac{\lambda L}{2R\lambda} = \frac{l}{2} \quad [2.51]$$

This is the resolution given for focused SAR system.

For space borne radar, the curvature of the Earth helps to achieve slightly a better resolution, in both the range and azimuth directions, when the curvature factor is included, using Figure 2.16 for the geometry:

$$\begin{aligned} X_a &= \frac{R_E}{R_E + h} \frac{l}{2} \\ X_r &= \frac{R_E}{R_E + h} \frac{c\tau}{2 \sin \theta} \end{aligned} \quad [2.52]$$

## **2.4.6 Signal Processing:**

The power of SAR comes not from the radar system itself, but in the ability to achieve the desired system performance through signal processing. The basic theory behind the formation of the synthetic aperture has already been discussed at length in the preceding sections. Therefore, the initial description will be reserved until the discussion of image formation algorithms and the actual signal processors available for SAR systems.

### **2.4.6.1 Optical:**

The optical processor was the initial choice for the focused SAR system, due to the optical nature of the image. In this process, the target coordinates are taken as  $x$ , the

azimuth position, and  $y$ , the range position. This processor is the best for wide swath, high-resolution applications where immediate access to the map is not required [STIMb-98].

In the optical processor, the signal information is recorded onto a data film, with each pulse maintaining the same range coordinates,  $y$ , but the motion of the film allows for the translation of the azimuth coordinates,  $x$ . Once detailed with the signal responses, the film is then passed through a coherent optical imager and the coded information becomes an image. This process takes a myriad of different lenses in order to preserve the relative dimensions of  $x$  and  $y$  and to align the image [HOVA-80].

The power of the optical image processor comes from its relatively simple application rather than complex and intricate linear formations needed in numerical processing [STIMb-98]. This is due to the identical nature of the laws governing the propagation of reflected radar waves and optical waves. The disadvantage of this system is the time that it takes to create the image and develop the film. While compatible with airborne radar systems, the power requirements, the nature of the space environment, and the movement within the image processor make it less than ideal for space applications.

#### **2.4.6.1 Electric/Digital Signal Processors:**

Focused SAR offers fine resolution, but also requires a large amount of data storage, which first led to the use of optical systems where the photographic film can store such quantities. However, with the advent of high-speed and large capacity digital computers to execute the fast Fourier transforms (FFT), digital signal processing has become more widely used [STIMb-98]. The digital processor has advantages due to the near digital form of the radar returns in that the echoes are already samples of a continuous return. This allows for many image processing techniques to enhance the image and allow for near real-time implementation when desired.

In the digital processor, the in-phase and quadrature components of the returned signal are first quantized. Unlike in optical processing, digital processors allow for auto-focusing and motion compensation to occur as a pre-filtering of the data. The range, determined by the time delay, and the azimuth, determined by the Doppler behavior, are stored into the memory before being processed through the Fast Fourier Transform (FFT) block.

A fundamental issue for the design of a digital system is determining the sampling rate of the incoming response. The first level of sampling frequency is the pulse repetition frequency, PRF, of the transmitter. This frequency is limited by the mapping range of the radar and the Doppler frequency shift from the extreme points of coverage [STIMb-98]. The lower limit of the PRF is found from the Doppler frequency shift. In this case, the PRF must be greater than the highest Doppler shift so that the returns will be centred on the carrier frequency. The upper limit of the PRF comes from the need to allow for the maximum mapping range return to fall within the inter-pulse period. Therefore, the PRF must fit within the following inequality:

$$\frac{2V}{l} \leq PRF \leq \frac{c}{2R_{\max}} \quad [2.53]$$

where  $l$  is the real aperture length in the azimuth direction,  $R_{\max}$  is the maximum range and  $V$  is the radar platform velocity.

In the case of space borne SAR, it is possible to transmit several pulses before the ground return from the initial pulse. This does not pose a problem as long as there is a window of reception between each pulse so the maximum range return from the first pulse is received before the minimum range return from the following pulse [STIMb-98].

With the PRF defining the sampling frequency in the azimuth direction, it is necessary to determine the sampling needed for the range. In digital SAR processing, as in most digital signal processing, the sampling frequency of the returned signal is determined by the Nyquist criterion—the number of time samples for representing a frequency should be at least twice that frequency [HOVA-80]. Thus, at the input to the receiver, the pulse

compression filter, the digital sampling rate must be twice that of the frequency excursion of the pulse,  $\Delta\omega$ . Therefore, the initial sampling rate is:

$$f_{sr} = 2\Delta f \quad [2.54]$$

This sampling rate, multiplied by the sampling time,  $T_s$ , gives the total number of samples where:

$$T_s = N_R \tau \quad [2.55]$$

and  $\tau$  is the compressed pulse width and  $N_R$  is the number of range gates, the division of the returns based upon resolution.

The number of range gates, or range bins, can be found from the range resolution:

$$N_R = \frac{R_{\max} - R_{\min}}{X_R} = \frac{R}{X_R \tau \tan \alpha} \quad [2.56]$$

where  $R$  is the average range,  $\tau$  is the compressed pulse width,  $X_R$  is the range resolution and  $\alpha$  is the incident angle. The number of range gates may also be looked at as the swath width in the range direction divided by the range resolution value.

## 2.4.7 Reconstruction Algorithm:

The final step is to analyse the method by which the raw SAR data is turned into an image. This is a process with three steps: analysing the return echo and correlating with a copy of the transmitted signal; echo compression sampling in amplitude and phase; and FFT the focused amplitude and phase into intensity to form the image.

Matched filtering is the first step in this process, occurring in the intermediate frequency (IF) filter. The purpose of this step is to estimate the correlation between the echo and the transmitted signal to establish the temporal resolution and maximize the S/N [BARB-85]. The transmitted pulse of the system is given by the equation:

$$s_t(t) = a(t) \exp(j2\pi(f_c t + \frac{\alpha t^2}{2})) \quad [2.57]$$

$$\alpha = \frac{\Delta\omega}{\tau}$$



where  $\alpha$  is the frequency sweep of the system,  $f_c$  is the centre frequency and  $\tau$  is the pulse length. This function will be used to correlate the received echo.

On the receipt of each pulse, the receiver down converts the RF centre frequency to an offset base-band frequency,  $f_1$ , where:

$$f_1 \geq \frac{B}{2} \approx \frac{f_s}{4} \quad [2.58]$$

where  $B$  is the system bandwidth and  $f_s$  is the sampling frequency. The receiver output signal is given by the equation:

$$s_r(t) = \exp \left( j2\pi \left( f_1 t_n - f_c t_D + \alpha \frac{(t_n - t_D)^2}{2} \right) \right) \quad [2.59]$$

where  $f_c$  is the RF centre frequency,  $t_n$  is the time at the centre of the pulse, and  $t_D$  is the delay time of the signal. This signal is correlated to the filter impulse response function,  $h(t)$ , which is the complex conjugate of a replica of the chirped signal [CURLa-91].

The matched filter can also be designed as a pulse compression filter. Like the matched filter, the impulse response for a pulse compression filter is the complex conjugate of the replicated chirp signal, however, for pulse compression, the impulse response is the inverted complex conjugate [CURLa-91]. Once the signal has passed through either the matched filter or the pulse compression filter, it is ready to be processed in the range and azimuth directions.

The first step in reconstructing the image is range compression. This is performed on each pulse as it is output from the receiver and consists of correlating the receiver output with the replica of the transmitted pulse translated to the offset video frequency. The peak correlation occurs at the round trip time delay [FRAN-99]. The continuous functions are sampled at an appropriate frequency, then Fourier transformed to allow for correlation in the frequency domain with a digital FFT to reduce computations. To use the digital FFT, it is necessary that the number of samples is a power of two ( $N=2^n$ ), and therefore the pulsed signal is truncated, or packed with zeros, as the sampling requirements rarely give an appropriate number of samples [FRAN-99]. The pulse

replica is sampled at the same sampling frequency and packed with zeros to make it the same length as the recorded pulse length. The two signals are then correlated using a digital convolution.

Given the previously defined transmitted and received signals, the point-spread function from the correlation is:

$$g_R = \frac{1}{2} \int_{t_D - \frac{\tau}{2}}^{t_D + \frac{\tau}{2}} \exp\{j2\pi(f_1 t_n - f_o t_D + \alpha(t_n - t_D)^2)\} \times \exp\{-j2\pi(f_1(t_n - \tau_R) + \alpha(t_n - \tau_R)^2)\} \\ + \int_{t_D - \frac{\tau}{2}}^{t_D + \frac{\tau}{2}} \exp\{-j2\pi(f_1 t_n - f_o t_D + \alpha(t_n - t_D)^2)\} \times \exp\{j2\pi(f_1(t_n - \tau_R) + \alpha(t_n - \tau_R)^2)\} dt_n \quad [2.60]$$

where  $\tau_R$  is the correlation variable,  $t_n$  is the time at the centre of the pulse,  $f_1$  is the offset base-band frequency,  $f_o$  is the centre frequency, and  $t_D$  is the time delay. The resulting output response is:

$$g_R = \exp\{j2\pi(-f_o t_D + f_1 \tau_R - \alpha(t_D - \tau_R)^2)\} \sin c(\pi \Delta F_R(t_D - \tau_R)) \quad [2.61]$$

where  $\Delta F_R$  is the chirp pulse bandwidth.

After range compression, Equation 2.61, the pulse is stored in bulk-storage memory serially line by line in large blocks. However, for azimuth compression, the data needs to be accessible in column format, as there are samples taken from each pulse. The data is then reorganized through the process of "corner-turning" before being processed through the azimuth filter [CURLb-91]. In this process, the data is re-ordered so that it is accessible in equi-range blocks rather than range lines.

Before azimuth compression, the data must also be corrected for range migration. Range migration is the movement of the response from a point through different range cells due to the Doppler error due to the rotation of the Earth and the changing slant range for an orbital platform. The correction for range migration must be applied before the azimuth compression.

If the time delay to the point target,  $t_D$ , is expanded in a Taylor series around  $t=0$ , the centre of the aperture, then:

$$t_D = \frac{2}{c}(a_0 + a_1 t + a_2 t^2) \quad [2.62]$$

where all higher order terms are neglected and  $a_0$  is the slant range,  $a_1$  is the slant range velocity and  $a_2$  is the slant range acceleration [BARB-85]. This range polynomial can be calculated from the orbital characteristics and the rotation of the Earth. This is used in the correction of range migration.

It is now possible to apply the function to the azimuth compression filter. The phase history of the point is given by:

$$\phi(t) = \exp\{-j2\pi f_o t_D\} \quad [2.63]$$

where  $t_D$  is found in Equation 2.62. This history is correlated against the processor response:

$$\begin{aligned} \phi'(t) &= \exp\{-j2\pi f_o t_D'\} \\ t_D' &= \frac{2}{c}(a_o + \Delta a_o + a_1 t + a_2 t^2) \end{aligned} \quad [2.64]$$

where  $\Delta a_o$  is the small change in the slant range value over the interval  $\tau_R$ .

The azimuth correlation function, including the convolution for the range migration is given by the equation:

$$\begin{aligned} g(\tau_R, \tau_A) &= \int_{-\frac{T_A}{2}}^{\frac{T_A}{2}} \int_{T_D - \frac{\tau}{2}}^{T_D + \frac{\tau}{2}} \delta(t_D - t_R + \tau_R) dt_R \times \exp\{-j2\pi \cdot \alpha(t_D - t_R) \text{sinc}(\pi \Delta F(t_D - t_R))\} \\ &\times \exp\left\{-j \frac{2\pi}{c} 2f_o(a_o + a_1 t + a_2 t^2)\right\} \times \exp\left\{j2\pi \frac{2f_o}{c}(a_o + \Delta a_o + a_1(t - \tau_A) + a_2(t - \tau_A)^2)\right\} dt \end{aligned} \quad [2.65]$$

where the range compressed data spans the time interval of  $t_D \pm \frac{\tau}{2}$  [BARB-85].

When these correlations are applied to the receiver output signal in the correct order, the result is a point intensity for each target at the measured range and azimuth. These values can then be coordinated with a latitude and longitude for a map projection image.

#### 2.4.7.1 Bi-static Extension of Reconstruction Algorithm:

The reconstruction algorithm with respect to a mono-static SAR system can be extended to a bi-static system with relatively few modifications to the equations. The basic process of reconstruction and the assumptions laid forward in the mono-static case will apply for the extension.

Corresponding to the mono-static case, matched filtering is still the primary step in the processing algorithm. The transmitted signal and the received signal match with Equations 2.57 and 2.59, respectively. However, in the bi-static case, the time delay for the signal is:

$$t_D = \frac{R_T + R_R}{c} \quad [2.66]$$

Again, following the matched filtering to maximize S/N, the signal is then passed through the range compression filter to determine the round trip time delay. The range equations for the transmitter and receiver are first expanded using a Taylor series:

$$\begin{aligned} R_T(s) &= R_{Tc} + \dot{R}_{Tc}(s_T - s_c) + \ddot{R}_{Tc}(s_T - s_c)^2 \\ R_R(s) &= R_{Rc} + \dot{R}_{Rc}(s_R - s_c) + \ddot{R}_{Rc}(s_R - s_c)^2 \end{aligned} \quad [2.67]$$

where  $s_T = \frac{s}{V_T}$  and  $s_R = \frac{s}{V_R}$

and  $s$  is the spatial variable in the azimuth direction  $\dot{R}$  is the rate of change in the range, i.e. velocity, and  $\ddot{R}$  is the second derivative of the range, i.e. acceleration.

Therefore, the signal at the receiver can be written as:

$$s_r(s, t) = \exp \left\{ j2\pi \left[ f_1 \left( t_n - \frac{R_T(s) + R_R(s)}{c} \right) + \alpha \frac{\left( t_n - \frac{R_T(s) + R_R(s)}{c} \right)^2}{2} \right] \right\} \quad [2.68]$$

Correlating this with the replica of the transmitted pulse gives an output correlation response of:

$$g(s, t) = B_R \exp \left\{ -j4\pi \left( \frac{R_1(s)}{\lambda} \right) \right\} \sin c \left[ \pi \frac{B_R}{c} \left( \frac{R_T + R_R}{c} - R_1(s) \right) \right] \quad [2.69]$$

$$R_1(s) = R_{Tc} + R_{Rc} - \frac{\lambda}{2} (f_{DT} + f_{DR})s + \left( \dot{f}_{DT} + \dot{f}_{DR} \right) \frac{s^2}{2}$$

where  $B_R$  is the bandwidth of the received signal,  $f_{DT}$  and  $f_{DR}$  is the Doppler frequency shift due to the system platform for the transmitter or receiver, respectively and  $\dot{f}_{DT}$  and  $\dot{f}_{DR}$  are the Doppler frequency rate of change for the transmitter and receiver, respectively. This result is equivalent to the output response in Equation 2.61, where  $t_D$  is as defined in Equation 2.67.

When expanding the azimuth equations to a bi-static notation, the Taylor series expansion for the time delay is:

$$t_D = \frac{[(a_{T0} + a_{R0} + (a_{T1} + a_{R1})t + (a_{T2} + a_{R2})t^2)]}{c} \quad [2.70]$$

where the subscripts T and R correspond to the transmitter and receiver contributions, respectively and the range polynomial coefficients are the same as in Equation 2.62.

The slant ranges  $a_{T0}$  and  $a_{R0}$  can be found from the time delay of the system, however, the other coefficients come from the orbital characteristics and the rotation of the earth and give the range migration corrections for the system.

Therefore, with this new definition of the range polynomial, the azimuth compression output can be expressed as Equation 2.65.

### **2.4.8 Image Defects and Corrections:**

This method of image reconstruction should lead to a focused image with the appropriate resolutions. However, this is not always the case as any number of factors can cause errors in the phase and amplitude measurements to degrade the image quality.

The first, and most troubling, effect of these errors is image defocusing. This is caused by the occurrence of fluctuations in the path length between the radar receiver aperture and the scene, caused by variations in the refractive index, multi-path effects, and the deviations of the sensor from the established track [CURLb-91]. This deviation from the assumed trajectory may be from a mismatch in the assumed velocity and acceleration or a displacement of the platform from the estimated position. As seen from the explanation of the echo signal and the reconstruction algorithm, SAR uses the accurately known distance for correcting of the phase delay. Any distortion of this will cause the image to defocus in that each pixel is not accurately mapped. Auto-focus techniques have been developed to help overcome these errors and improve the image quality [CURLb-91].

Geometric and radiometric distortion is the other main error that reduces the image quality. Again, this error is caused by the deviations from the assumed motion in the range and azimuth directions. This causes not only a defocusing of the image, but also distortion of the actual dimensions of the image. These distortions are proportional to the velocity deviations. Unlike defocusing, the main effect of the distortions comes from non-planar movement of the platform. This cannot be corrected with auto-focus, but rather through the measuring of the actual motion of the platform and this information is then used in the processing to correct the image. This is called motion compensation [CURLb-91].

#### **2.4.8.1 Motion compensation:**

Motion compensation is the method used to correct for the planar and non-planar motion deviations from the assumed trajectory [STIMc-98]. In radar applications, it is

acceptable to have deviation within a quarter of the wavelength during a single pulse, to maintain phase coherence within a small error. This deviation is reduced by another factor of two for SAR due to the two-way propagation—one eighth of a wavelength [STEI-76]. This level of control may not be possible to achieve. However, with signal processing, it has become possible to use a correction for the motion deviation with the signal echo to maintain this accuracy.

In motion compensation, an external motion sensor is used to accurately record the actual motion of the radar platform [STIMc-98]. This motion is then manipulated to determine the frequency change that accompanies the deviated motion and this is applied to the echo response as the signal is being processed. This, in effect, removes the phase error by applying a corrective function to the signal processing. While this cannot remove all errors, it can remove enough for to maintain image quality.

#### **2.4.8.2 Auto-focus:**

Auto-focusing of SAR images is a widely used signal processing strategy to compensate for the quadratic and higher level phase errors [CURLb-91]. This technique is most often applied after the original motion compensation and data formatting. Auto-focus is normally accomplished in two steps: error estimation within the signal and error compensation.

There are multiple methods of auto-focusing. Prominent point processing is used when strong point targets exist. This method allows for high performance in correcting phase errors, but requires dominant scattering elements throughout the scene. The coherent auto-focusing methods are phase gradient and phase difference [WU-00]. These techniques operate directly on the complex,  $e^{j\theta}$ , received signal to correlate the phase differences or gradients between phases throughout the picture. These values are then used to estimate a correction function. Finally, incoherent methods, map drift and contrast optimization, use the intensity of compressed images and disregard the phase information [WU-00].

The most common algorithm used for auto-focusing an image is called Phase Gradient Auto-focus, PGA [WU-00]. It consists of making an estimate of the gradient of the phase error in the SAR image using four steps: centre shifting, windowing, phase gradient estimation, and iteration. The algorithm was created for spotlight SAR, due to the plausible assumption in spotlight SAR that the phase error is constant with range. This assumption is not correct for stripmap SAR until the data has been formatted further.

The auto-focus algorithm is applied after the range compression of the raw data has been completed to allow for the separation of the image into range bins. For each range bin, the strongest scatterer,  $a_n$ , is chosen and shifted to the origin of the image. This is done to remove the frequency offset due to the Doppler shift. This must be done in a circular manner so that samples, which are shifted off the edge may be wrapped around and shifted to the opposite side. This centre shifting attempts to align strong scatterers and subsequently improve the S/N for the phase estimation.

Once the image has been centre shifted, it is windowed, preserving the width of the dominant blur for each range bin while discarding the data that does not contribute to the phase error estimation, i.e. clutter. The window size,  $W$ , is chosen by registering the dominant blur on each range bin and averaging over all the bins. These are incoherently summed to obtain a one-dimensional function whose width, at a chosen threshold, gives the point-spread function. This is nominally given by:

$$s(x) = \sum_n |f_n(x)|^2 \quad [2.71]$$

where  $f_n(x)$  is the circularly shifted image data and  $n$  is the bin number [WAHL-94].

The redundancy of the blur, as assumed with a constant phase error with range, the function,  $s(x)$ , will plateau at its maximum value approximately the width of the window,  $W$ , and smaller outside of  $W$ . As the image becomes more focused,  $W$  will converge until it is only a few pixels in size.



When the scene does not contain strong scatterers, i.e. images of natural landscapes, seascapes or icescapes, the above method will not work, as the range bins do not provide a strong enough scattered response to allow for windowing of  $s(x)$ . The window width,  $W$ , is then chosen to span the maximum possible blur width and progressively reduce by 20% per iteration.

Once shifted and windowed, the image data is now represented by

$$G_n(u) = |G_n(u)| e^{j[\phi_e(u) + \theta_n(u)]} \quad [2.72]$$

where  $G_n(u)$  is the inverse Fourier transform of the image data,  $g_n(x)$ ,  $\theta_n(u)$  is the scatterer-dependent phase function and  $\phi_e(u)$  is the phase error [WAHL-94].

The linear unbiased minimum variance (LUMV) estimate for the gradient of the phase error is given by:

$$\begin{aligned} \hat{\phi}_{lumv}(u) &= \frac{\sum_n \text{Im} \{G_n^*(u) \dot{G}_n(u)\}}{\sum_n |G_n(u)|^2} \\ \hat{\phi}_{lumv}(u) &= \dot{\phi}_e(u) + \frac{\sum_n |G_n(u)|^2 \dot{\theta}_n(u)}{\sum_n |G_n(u)|^2} \end{aligned} \quad [2.74]$$

The estimated phase gradient,  $\hat{\phi}_{lumv}(u)$ , is integrated to obtain an averaged value which is then used as the phase correction,  $\hat{\phi}_e(u)$ . This is done to remove any bias and linear trend. This phase correction is then complex multiplied by the range-compressed phase history domain data by:  $\exp[-j\hat{\phi}_e(u)]$ . The process of center shifting, windowing and phase gradient estimation is repeated. As the image begins to focus, the scatterers become more compact making the circular shifting more precise and the window size smaller.

When the PGA algorithm is applied to stripmap data, the assumption of constant phase error with range is no longer valid and a conversion of the data from stripmap to spotlight, known as Stripmap Spotlight Compression (SSC) [BATE-98].

## **Chapter 3 SAR System Design:**

### ***3.1 Scattering Properties:***

The following discussion builds upon the general electromagnetic propagation background already provided with an emphasis on radar applications and the properties of sea ice.

#### **3.1.1 Electromagnetic Scattering from Rough Surfaces:**

Any electromagnetic field which is incident upon a boundary between changing media will be either transmitted, reflected or scattered, depending upon the wavelength of the incident wave, the incident angle of the wave and the electric properties—emissivity, permeability, and conductivity, of the second media [BECKa-87]. While the scattering from a plane boundary, in which the interface is smooth, is well known, when the surface becomes “rough”, the problem becomes complex. A smooth plane will reflect the incident wave in a single direction. A “rough” surface will scatter the wave in multiple directions. It is this property of a “rough” surface, which makes it difficult to determine the characteristics of the scattering. To make this problem easier, certain acceptable assumptions are made to simplify the equations:

- 1) The dimensions of the scattering elements are either much smaller or much greater than the wavelength
- 2) The radius of curvature of the scattering elements is much greater or much smaller than the wavelength
- 3) Shadowing effects are neglected
- 4) Only the far-field situation is considered
- 5) No volumetric or multiple scattering is considered
- 6) The density of scatterers remains constant over the entire medium [BECKa-87]

The first step in determining the scatter from the interface is to determine the “roughness” criteria, better known as the Rayleigh Criterion, in which the path length and phase difference between the two rays incident upon a surface with an irregularity height of  $h$  offer the general criteria of:

$$h \leq \frac{\lambda}{8 \sin \gamma} \quad [3.1]$$

where  $\gamma$  is the incidence angle of the rays upon the surface and  $\lambda$  is the wavelength of the incident energy [BECKa-87]. From this criterion, the relationship between “roughness” and wavelength is clear: the roughness of the surface is directly dependent on the incident wavelength. A surface that appears rough to a short wavelength, would appear smooth when the incident wavelength is longer.

A theoretical algorithm to model the scattering from a rough surface is provided by Beckman and Spizzichino [BECKa-87]. From this algorithm, it is possible to calculate a generalized scattering model if the average height of the irregularities is known, and the electromagnetic and physical properties of the surface are known or can be accurately estimated.

### **3.1.2 Remote Sensing of Sea Ice:**

The proposed mission for the SAR system is the remote sensing of the polar regions for either scientific or commercial applications. Both applications require knowledge of the thickness of the sea ice, the distribution of that thickness, the extent of ice coverage, and the thawing and freezing cycles of the area. It is, therefore, important to know the scattering characteristics of sea ice based upon these physical properties and electromagnetic characteristics.

To gain an understanding into the actual properties of ice, it is important to understand how it is formed and the changes in the composition of the ice over multiple cycles. As microwave scattering characteristics of ice are very sensitive to changes in structure and

composition, by understanding the different stages of ice, it is possible to classify the return as originating from specific types of ice.

In the polar region, ice begins to form on the surface of the ocean as a thin layer of slush. This is due mainly due to the nature of the ocean: high salinity and surface movement. This initial formation of crystals on the ocean surface causes a reduction to the movement of the surface of the ocean [CARS-92]. As this happens, the ice begins to coagulate forming a thin layer, up to 10 cm thick or forms pancake ice, small cylinder structures of ice ranging from 0.3 to 3 metres in thickness. Pancake ice usually forms in areas of more open water where the surface movement is greater. The composition of this newly formed ice is one of pure ice, brine inclusions—caused by the super-cooling of the seawater and the forcing of brine into pockets—and pockets of trapped air [CARS-92]. This composition greatly affects the electromagnetic and scattering properties of the ice.

As the ice begins to grow, a desalination process takes place. As brine is denser than the surrounding ice, gravity will cause the brine to drain from the ice sheet or to form large brine pockets. However, this occurs more in the bottom layers of ice, whereas the top layer, due to its colder temperature will maintain a high level of salinity. As the ice grows, it also increases the pressure on the individual crystalline structures, causing an increase in density and, again, forces the brine pockets out of the ice [CARS-92]. Throughout the aging of the ice, it continues to desalinate, thus changing the electromagnetic characteristics between first year ice (FY) and multi-year ice(MY).

The factor that causes the greatest difference in the characteristics of MY ice from FY ice is the melt season [CARS-92]. As the temperature rises during the summer months, the ice continues to desalinate. The differences in FY salinity to MY salinity can be up to 9%. The melting of the surface causes not only desalination, but also melt ponds and hummocks. The melt ponds are collection, on the surface of the ice, of water. The water collects in small ponds, creating a depression. The ice located between these depressions is called hummocks. When ice begins to refreeze in late summer and early fall, the melt

ponds re-freeze, creating smooth patches, which exhibit FY ice characteristics, while the surrounding area will exhibit MY ice characteristics.

Other great differences in the characteristics of FY ice to MY ice include surface roughness and density. The surface of undeformed FY ice is flat with little variation. Deformed FY ice is characterized by sharp, angular ridges [CARS-92]. MY ice has an undulating surface with hummocks and melt ponds. The once deformed FY ice has been weathered away so that the deformed MY ice shows none of the angular characteristics, simply the presence of hill-like structures [CARS-92]. The density of MY ice is much greater than that of FY ice due to aging compression [CARS-92]. This allows for more volumetric scattering to occur in MY ice compared to FY ice.

Understanding the basic physical structure of ice is useful when discussing the electromagnetic properties important to scattering characteristics. The main factor when addressing the electromagnetic properties of ice is the relative permittivity. This is the complex (real and imaginary) electrical property of ice, based on free space and electromagnetic loss of the material [CARS-92]. This value is related to the conductivity, absorption, and penetration depth of the incident energy. As sea ice is a melange of freshwater ice, brine and air, the electromagnetic properties of the ice depend directly on the combination of these constituents. Through multiple experiments and measurements, it has been determined that the relative permittivity of sea ice at 2.4 GHz is:

$$\begin{aligned}\epsilon &= \epsilon' + j\epsilon'' \\ \epsilon' &= 3.09 + 0.0081V_b \\ \epsilon'' &= 0.03 + 0.0042V_b\end{aligned}\tag{3.2}$$

where  $V_b$  is the volume of brine measured in part per trillion [CARS-92].

Having thus laid out the physical and electromagnetic properties of different types of sea ice, it is necessary to now translate these into scattering behaviour and the scattering coefficients for radar signatures. When analysing the scattering from ice structures, the following factors affect the scattering coefficient [CARS-92]:

- 1) Backscattering increasing with increasing ice crystal size

- 2) Increasing frequency increases the scattering coefficient
- 3) Increasing scattering coefficient with decreasing incidence angle
- 4) Scattering due to ice thickness varies based on composition of ice, but generally increases
- 5) Scattering decreases with water content
- 6) Scattering increases with increasing air bubble size
- 7) Scattering increases with increasing density

With such a wide variety of variables in the modelling of scattering from sea ice and the inability to gain accurate estimations of the variability in height, it is difficult to achieve an accurate model of any ice structure from a theoretical algorithm. Generalized models of types of ice are constructed on a case-wise basis. However, as volumetric scattering is difficult to model, the theoretical values vary significantly at times from actual results. Given these inaccuracies, extrapolated values from actual measurements will be used to estimate the scattering coefficients used in this study. The assumption made when establishing these values was at the small incident angle at which the system will be operating ( $4^\circ$ ) it is feasible to use results for a  $0^\circ$  incidence angle as an approximation.

Beginning first with the scattering of energy from the ocean surface, which will give a base when comparing the signatures of ice structures, it is important to remember the dependence of the scattering from ocean surfaces on wave size and wind strength. Each of these variables will change the characteristics of the surface. From a smooth, calm ocean surface (which is often found within close proximity to ice) there is a powerful vertical incidence reflection coefficient of approximately 0.5, with little absorption in the media. This will cause a very high response from a smooth ocean, i.e. it will appear very bright in the system. Any increase in wave height or surface winds will decrease the total reflected energy, but it will still remain brighter than the surrounding ice. The normalized radar scattering cross section, as is used in the radar equation, of a calm sea is -0.5 to -3 dB [ONST-92]. This value is constant throughout the year.

Grey ice or thin FY ice, characterized by 1-20 cm in thickness, has a high salinity content with a surface temperature of 0°C [ONST-92]. This causes a high dielectric constant, but a low absorption coefficient as there is often large concentrations of liquid water mixed within or between the ice. For smooth, undeformed ice the reflection for vertical incidence is high, dropping sharply for increasing deformity.

Thick FY ice, has lost some of the brine of new ice, has a rougher surface texture, typically covered with snow or a brine slush, and has a lower surface temperature. This will decrease the vertical reflection coefficient.

MY ice can be divided into two parts, the upper part, characterized by low density and large air bubble size, and a lower part, with high density and a high concentration of melt ponds. Therefore, the upper part will have nearly the same reflection as thick FY ice [ONST-92]. The lower part of the ice will produce a slightly higher vertical reflection coefficient as the contributions from the melt ponds and the higher density reduce volumetric scattering.

Using these general characteristics and extrapolating from the data of the Radar lookup tables of ERS-1, JERS-1 and EOS, the following approximate values for the radar normalized cross sectional vertical scattering coefficients are found:

	Winter/ Spring	Late Spring	Early Summer	Mid- Summer	Late Summer	Fall
MY (>220 cm)	-6.7 ± 2.2 dB	-4.3 ± 2.1dB	-9.3 ± 1.1 dB	-8.7 ± 1.1dB	-4.0 ± 1.8dB	-6.1 ± 2.4dB
Thick FY (70-220 cm)	-9.0 ± 2.1 dB	-8.1 ± 1.4 dB	-9.3 ± 1.1 dB	-8.3 ± 1.5 dB	-8.1 ± 1.8 dB	-8.7 ± 2.4 dB
Thin FY (<70 cm)	-4.3 ± 1.2 dB	-5.2 ± 1.6dB	-5.6 ± 1.4dB	-1.8 ± 1.4dB	5.1 ± 2.2dB	-4.8 ± 1.9dB

Table 3.1 Estimated Normalized Radar Crossed Section for  
Sea Ice at 2.4 GHz at 4° Incidence Angle [ONST-92]

Based on this table, the system can be designed for a minimum scattering coefficient of -15 dB to ensure readable returns from the surface within a margin of error. Based on these values the dynamic range of the system is approximately 15 dB.

Another important factor when discussing the imaging of a natural surface is the contrast in received echoes from different identifiable features on the ground. If there is not enough contrast between the features, they will be indistinguishable from one another and will appear uniform in the image. The contrast of the signals is highly variable on the polarization used for the incident waveform.

The following table is found with data from [CARS-92] are approximate values for the contrast:

Polarization	MY to FY	FY to Thin FY	Thin FY to Open Water
Vertical	6 dB	3 dB	5dB
Horizontal	5dB	2dB	3 dB

Table 3.2 Sea Ice Radar Contrast at 2.4 GHz at 4° Inclination [ONST-92]

It has been noted in experimental data that a vertical polarization can increase the contrast of very thin, newly formed ice, to FY ice and water by 2-3 dB over the response of an horizontal polarization [ONST-92]. Therefore, polarization diversity will be an important feature of the system.

### **3.2 Power Requirements:**

Using these basic characteristics of the chosen imaging area, the power requirements must be determined. This is the most difficult constraint for a SAR system on a micro-satellite.



To discuss power constraints, the following system characteristics will be assumed: a circular orbit at an altitude of 700 km, an orbital velocity of 7.54 km/s, a look angle (from beam centre to scene centre) of 3.2 degrees, antennas of 2.5m diameter and an efficiency of 30%, a transmitted wavelength of 12.5 cm, and a total system loss of 15 dB. Given these parameters, the average power needed for the system can be calculated (see Figure 3.1).

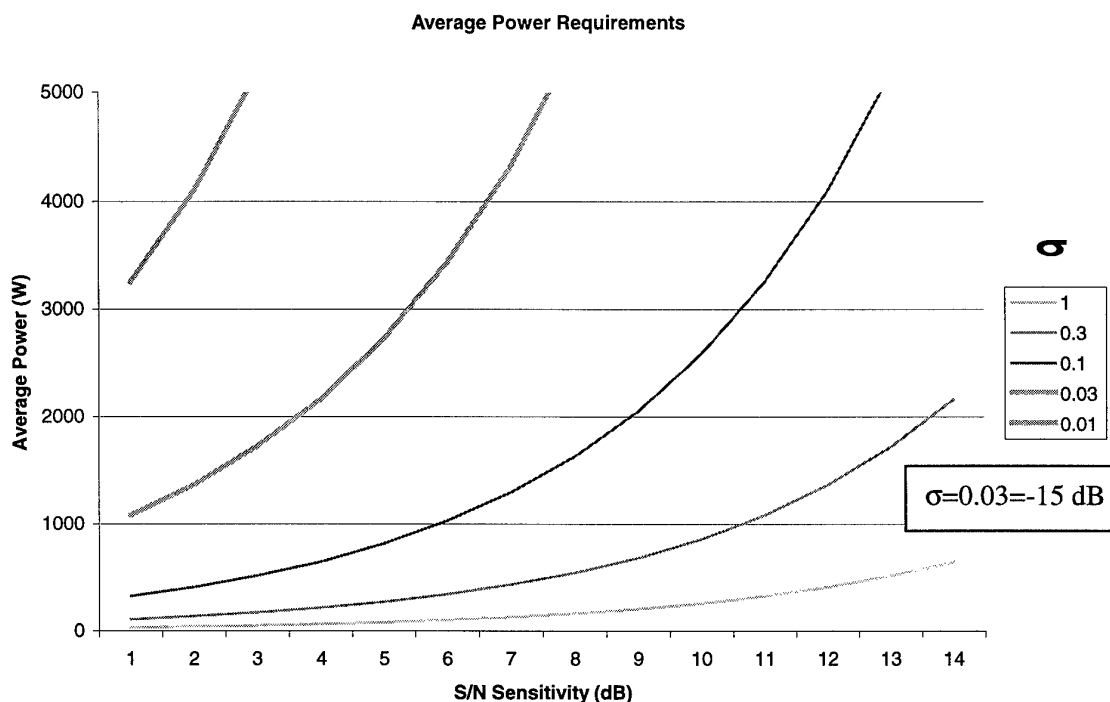


Figure 3.1 Average Power Requirements

The calculations are done at various normalized radar cross sections, from 0 to -20 dB, in order to determine the maximum performance of the system and the systems ability to meet the performance constraints. From this average power of the system, the total or peak power needed in the system can be calculated through the equation:

$$P_p = \frac{P_A}{(PRF)\tau} \quad [3.3]$$

where  $P_p$  is the peak power,  $P_A$  is the average power, PRF is the pulse repetition frequency and the  $\tau$  is the actual pulse length. Figure 3.2 shows the peak power needed in the system.

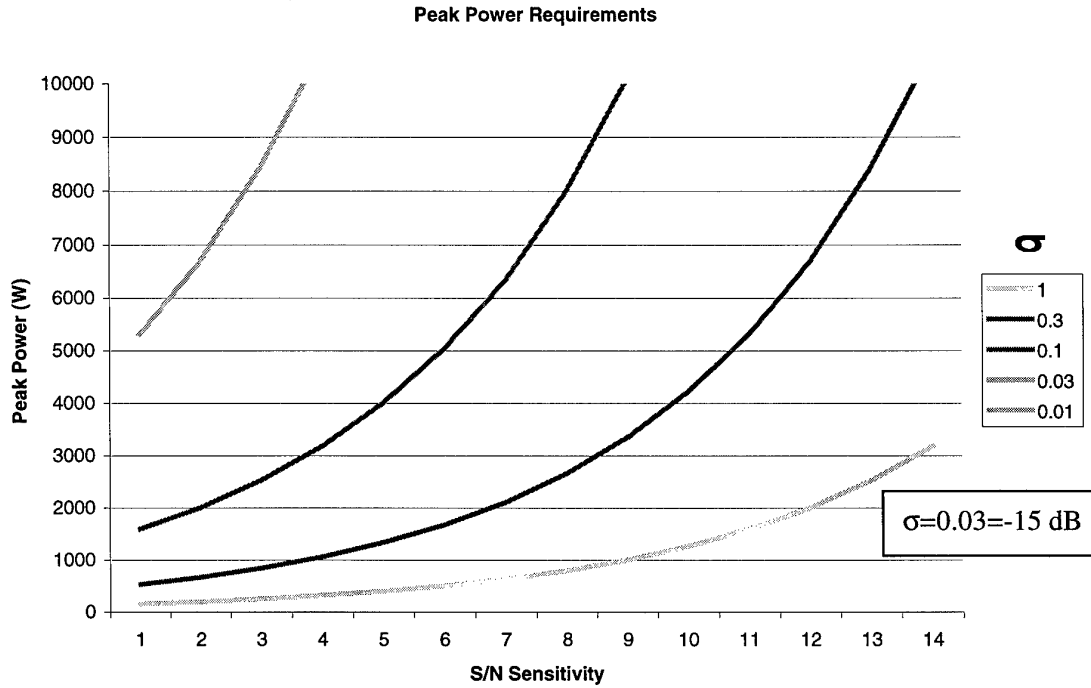


Figure 3.2 Peak Power Requirements

This peak power requirement can then be directly translated into the actual DC power that needs to be supplied by the transmitter to achieve the peak power output through the equation:

$$P_{DC} = \frac{P_p}{\eta G} \quad [3.4]$$

where  $P_{DC}$  is the DC power supplied to the transmitter,  $\eta$  is the efficiency, assumed to be 20%, and  $G$  is the gain of the antenna. Figure 3.3 represents this power requirement.

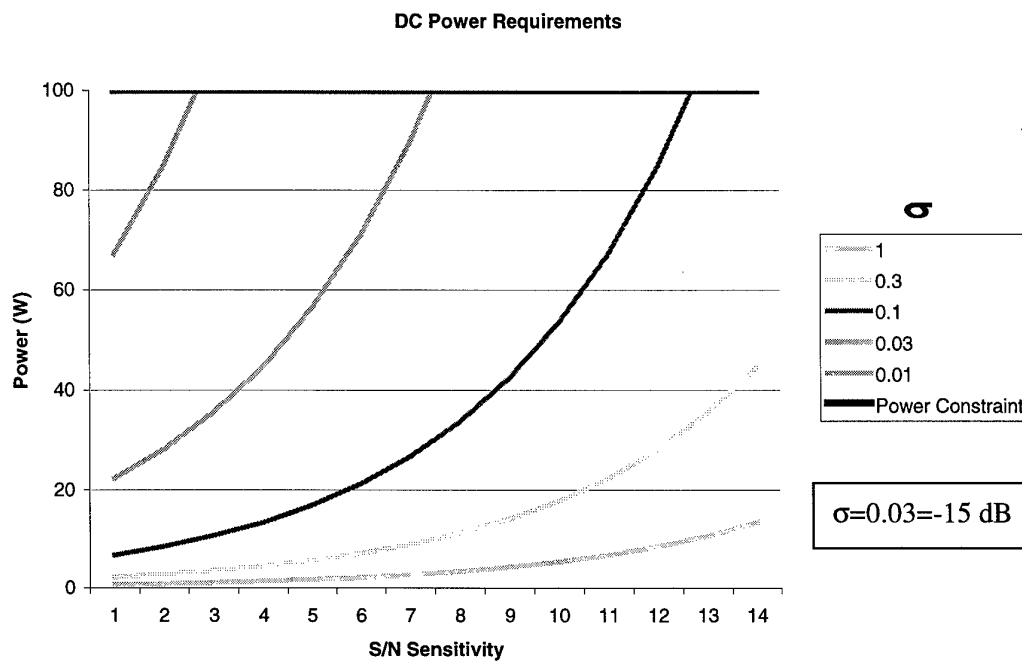


Figure 3.3 DC Power Requirements

Power constraints for the system is taken as 100 W, as can be seen from the horizontal constraint line, which can be achieved on the micro-satellite platform. This leads to a maximum system performance of  $-15 \text{ dB}$  radar cross section detected at a S/N sensitivity of at least 8 dB, to match the requirements set by the imaging area. These power requirements are calculated without taking into consideration the multi-look provisions and the resulting S/N gain. The integration of the returned energy over the multiple looks will increase the S/N by a factor of the number of looks, thereby reducing the power requirements by a similar factor. For this system, the number of looks is approximately 20.

### 3.3 Transmitter and Receiver Design:

#### 3.3.1 Transmitter Subsystem Design:

The transmitter for this system will need to generate coherent, rectangular pulses with a linear frequency modulation. It will need to be small in size to fit onboard a micro-satellite, however, as this is the only payload onboard the platform, this requirement is not constraining to the design of a relatively low power, S-band transmitter. The transmitter will need to transmit at a centre frequency of 2.4 GHz and a bandwidth of 100 MHz at a pulse repetition frequency of 6 kHz. The peak power output from the satellite's four body-mounted solar array is 140 W. Figure 3.4 is a block diagram of a coherent pulse transmitter.

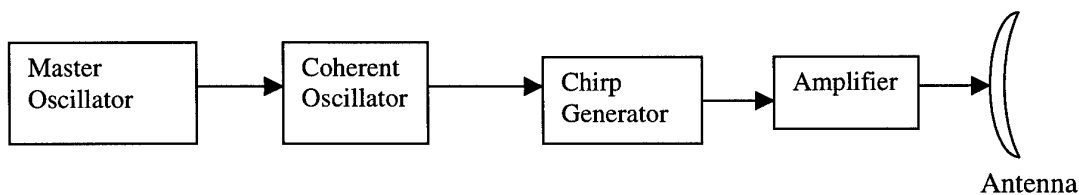


Figure 3.4 Transmitter Block Diagram

It is possible to see, that with this power constraint on the transmitter, it is possible to obtain, at maximum, a S/N of 8 dB for a scattering coefficient of  $-15$  dB, which requires 100 W input power to a 20% efficient transmitter. This is within the coefficients for sea ice sensing.

Having thus defined the basic requirements for the transmitter, it is important to look at the performance characteristics of the actual device and compare with the deviations from an ideal transmitter. Errors in the frequency, phase, and amplitude of the transmitter will cause defocusing and measurement errors in the final image, as the errors translate to azimuth phase and range timing errors.

When discussing the required stability of the transmitter, the first area of interest is the stable local oscillator, stalo, which provides the timing and control for the system. The

stalo needs to have good, short-term relative stability, specifically in the maintaining of a stable phase to allow for coherent demodulation at the receiver. The equation translating the stalo frequency drift into azimuth phase error is:

$$\sigma_p(\tau) = 2\pi f_c \tau \sigma_y(\tau) \quad [3.5]$$

where  $f_c$  is the centre frequency,  $\tau$  is the propagation time and  $\sigma_y^2(\tau)$  is the Allan variance of the oscillator [CURLc-91]. This equation gives a drift requirement of  $2.5 \times 10^{-10}$  over 4.7 ms propagation time with a  $1^\circ$  phase error. This value is well within the current technological possibilities [CURLc-91].

The long-term stability of the local oscillator is also important to the system, as it provides the maintenance of the carrier within a frequency band, and timing assemblies for other assemblies. Therefore, the stalo can either be reset periodically, i.e. before each imaging session, to ensure carrier phase maintenance, or the error of the transmitted signal, within bounds, can be translated to the receiving and processing subsystem to ensure a limited effect on the final image.

In a SAR system, a coherent oscillator, coho, is also used to maintain the phase of each pulse. It introduces, into the transmitter, the ability to begin each pulse with the same phase, necessary for coherent integration at the receiver. The error of phase within this instrument needs to be held to a minimum drift, approximately  $1^\circ$ , during the total imaging period of 4 s. This requirement is fixed, but achievable with current technology. The frequency stability and phase coherence requirements, whilst strict are not absolute. Small deviations from within the stated constraints will cause some image defocusing. However, with the use of auto-focusing during the processing of the received echoes, it is possible to iteratively reduce the effects of these errors, and thus restore the image.

While frequency and phase stability is necessary for the maintenance of a high performance system, the modulation scheme and its corresponding stability has greater effect on the actual image quality and resolution. In the case of a pulse compression radar, the compressed pulse width determines the actual range resolution of the system. The compressed pulse width is controlled by the bandwidth of the transmitted pulse, and

the ability for the matched compression filter to match transmitted values, i.e. the linearity of the transmitted pulse.

To achieve the stated requirement of a 30 m range resolution, at a minimum bi-static angle of  $5^\circ$ , it is necessary to have a transmitted signal bandwidth of 100 MHz, translating to approximately 3 MHz/ $\mu$ s sweep rate for a 34  $\mu$ s pulse. There is an error margin of approximately 3 MHz, or 3%, in the bandwidth value before there is a 1-metre loss in resolution. In sweep rate requirements this translates to a 0.11 MHz/ $\mu$ s error rate. While this is a strict requirement for the system, it is possible to achieve for short periods of time, of the order of a second.

Simply maintaining the bandwidth characteristics within these levels does not guarantee the desired range resolution. Addressing the linearity of the system, the requirements become relatively high to maintain system performance [CURLc-91]. Due to the low power nature of the system, and subsequently the relatively low S/N ratio at the input to the receiver, the system can sustain very small losses in S/N due to matched filter pulse compression. As the transfer function for the matched filter is defined on ideal characteristics, any deviation from these values relates to a loss of S/N as well as compression ability. To determine this requirement, the effects of non-linearity on the S/N will need to be tested. These values will then need to be translated to a maximum S/N loss tolerable in the system. Unlike the frequency and phase requirements, errors in the modulation scheme for the system are not removable through iterative correction, and therefore are fixed requirements.

To maintain a low cost system and relax these highly stable requirements, a direct digitally synthesized exciter is recommended. First applied to radar by W.D. Gallaway in the 1988 National Radar Conference, this exciter achieves near theoretical performance values [GALL-88]. This would allow for high synchronization between the transmitting, receiving and processing subsystems. It will be reviewed in more detail in the discussion on synchronization.

### 3.3.2 Receiver Subsystem Design:

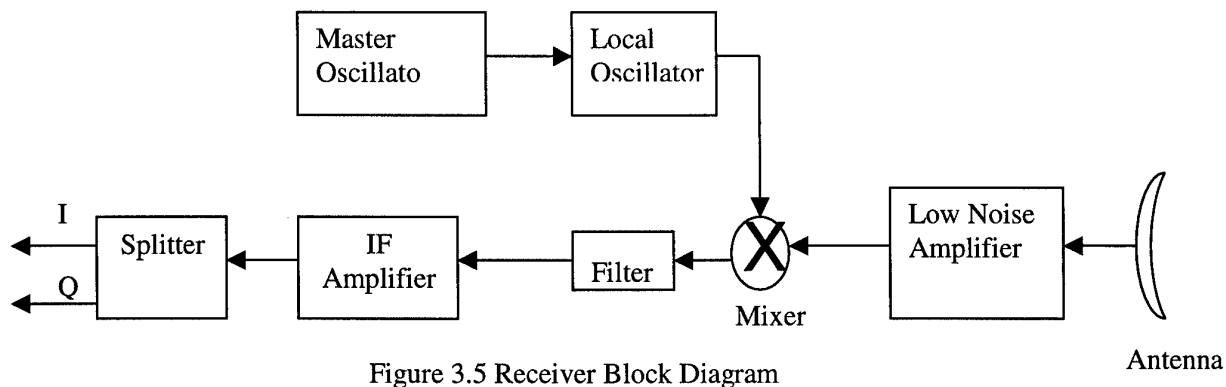
The ability of a radar receiver to detect an echo and extract the information from that echo is based, primarily, on the noise present. This noise may be external, having been input into the receiver along with the echo, or internal, due to the system components themselves. The receiver design is based on maximizing the S/N, usually done with a matched filter to enhance the desired signal, while suppressing the undesirable noise.

The first characteristic of the receiver that needs to be defined is the minimum detectable signal, i.e. the smallest signal which will be recorded, directly dependent on the probability of detection. Based on a S/N of 8 dB, which is achievable based on the transmitted power of 100 W and a probability of detection of 99.6 %, the minimum detectable signal is  $8.2 \times 10^{-10}$  Watts. This defines the sensitivity requirement for the system.

However, this calculation of the minimum detectable signal is based on a perfect receiver bandwidth. The bandwidth of the receiver determines the frequencies, which pass through the receiver at each of the stages. The bandwidth of the transmitted signal for system is 100 MHz, due to the chirped nature of the signal and the requirement for a 30 m range resolution. Added to this, is the total Doppler shift that can occur, 120 kHz, making a required minimum receiver bandwidth of approximately 101 MHz. If the bandwidth is smaller than this, then echoes returned outside of the receiver bandwidth will be lost. If the receiver bandwidth is made much larger than this bandwidth, excess noise can be admitted into the system, reducing the S/N and the quality of the image.

Figure 3.5 shows the basic block diagram for a receiver subsystem. The first stage of this is a low-noise amplifier. As any noise introduced into the system by the subsystem itself, i.e. internal noise, can mask a returned echo and also reduce the S/N ratio. All components, therefore, within the subsystem, are required to add as little noise to the system as possible. This amplified signal is then mixed with the signal from the local oscillator, to down-convert the signal to an intermediate frequency. This signal is again

passed through an IF amplifier. In this stage of the system, the signal is correlated, through matched filtering, with a copy of the transmitted pulse, to maximize the S/N. This signal is filtered through bandpass filter. The signal is then split into in-phase (I) and quadrature (Q) channels for digitising and recording. There will be no further SAR processing on-board the spacecraft, except to compression of the raw SAR data to minimize the required downlink bandwidth.



The receiver subsystem, like the transmitting subsystem, has limits on the amount of phase error, which can be introduced into the system, and has frequency stability requirements. As defined by convention, the total receiver phase error is of the order of  $5^\circ$  [CURLc-91]. This error is often defined by the pre- or post-processing techniques and any focusing algorithms used, as these techniques can compensate for some superfluous phase errors in the system. The frequency stability of the receiver stalo is the same as the transmitter, as this is a separate component due to the bi-static nature of the system. In mono-static SAR, the stalo is physically the same for both the transmitting and receiving system.

### 3.4 Antenna Design:

The final space borne components of the radar system are the antennas of both the transmitting satellite and the receiving satellite. Given the limited size of the spacecraft, the antennas will need to be of reduced size in comparison to other SAR satellite



antennas, and will need to be stowed for launch and deployed once in orbit. Finally, the antennas for the transmitting and receiving satellites need to be identical to allow for similar ballistic coefficients to minimize the station keeping activities.

The first decision is the size and shape of the antenna, e.g. a rectangular array or parabolic dish. The size of the antenna is constrained by the spacecraft size and the desired imaging area, 30 x 30 km.

It is possible to achieve a 35 x 35 km footprint with a 2.5 m diameter dish antennas, where 2.5m is the largest diameter the platform can support. The 5 km extra width in footprint, as compared to the desired image size, allows for a pointing error of  $0.5^\circ$  in any direction. The total area of the antenna is  $4.9 \text{ m}^2$ , resulting in a gain of 30.8 dB at 2.4 GHz at an efficiency of 30%. This antenna efficiency is a very conservative and pessimistic value, but to ensure the operability of the system, it is necessary to make such conservative assumptions until component testing can determine an accurate efficiency.

The difficulty with this antenna size is the volume needed for launch, requiring the antenna to be stowed initially and deployed once in orbit. The two proposed methods of deployment are the "umbrella" format, with a wire mesh antenna, or a "petaled" dish. Both deployment schemes will result in errors in aberrations and reduces the efficiency and cause errors in the antenna pattern. To gain accurate efficiency and radiation pattern information for either antenna designs, it will be necessary to construct and test the chosen antenna before operational use.

Due to the ease of deployment and storage, the petal structure was chosen. Figure 3.6a provides a side of the suggested stowed geometry. Figure 3.6b provides the deployed geometry for the antenna system. The basic idea behind the stowed geometry is a four-petal, flower configuration. The centre square of the antenna is attached directly to the base panel of the spacecraft. The remaining antenna area is divided equally into four parts and stowed along each side of the spacecraft. The panels will be designed so that

after deployment, they lock together to form a complete parabolic dish without any gaps between the panels.

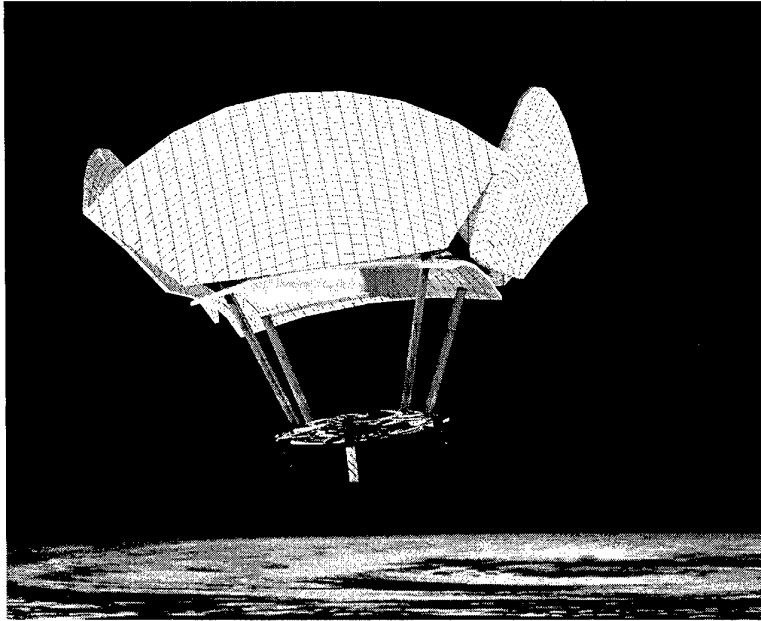


Figure 3.6a Side View of Antenna

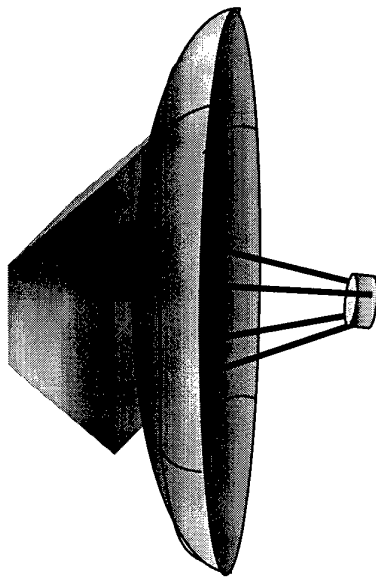


Figure 3.6b Deployed Antenna Design

Each panel will be rotated by  $85^\circ$ , making the total launch volume  $1.75 \times 1.75 \times 0.75 \text{ m}^3$ , and attached at the corner to the neighboring two sections for stability during launch.

The geometry of the dish and feed is defined by Figure 3.8. The relationship between the focal point,  $F$ , the radius,  $R_o$ , and the angle,  $\theta$ , is given by the equation [KRAU-88]:

$$F = \frac{R_o(1 + \cos \theta)}{2} \quad [3.6]$$

The following graph represents the relationship between the angle,  $\theta$ , and the focal length (as the radius is set at 2.5 m):

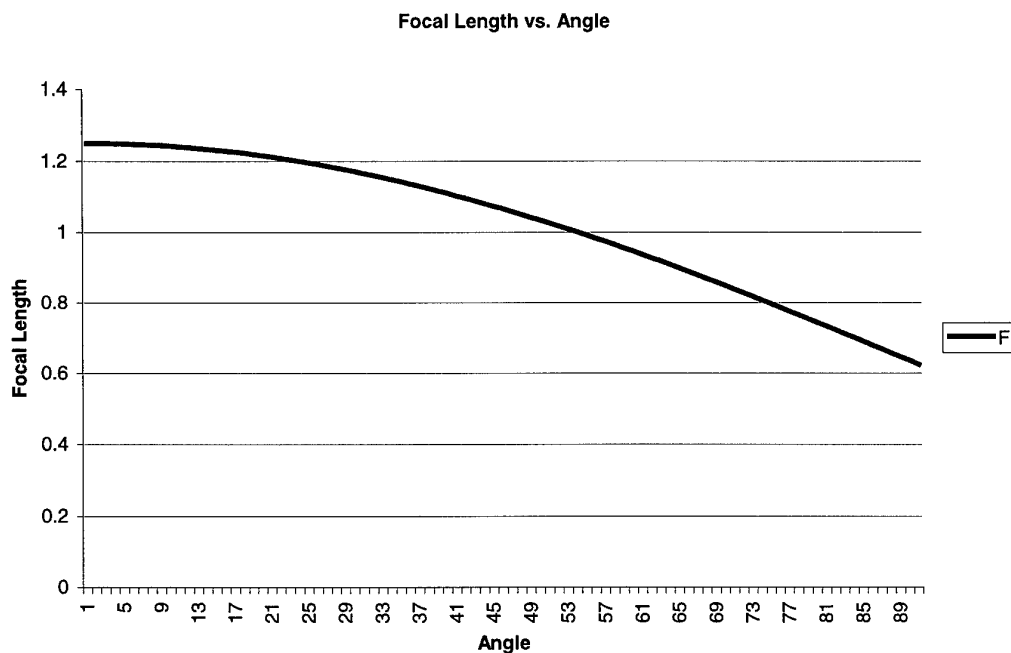


Figure 3.7 Graph of Focal Length and Angle Relationship

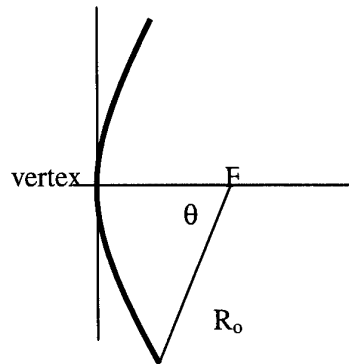


Figure 3.8 Parabolic Reflector Focal Length

Based on this geometry, the feed for this application will have an angle of 54 degrees and a focal length of 1 metre. A benefit from this choice is the optimization of the efficiency of the antenna, as the focal length is a multiple of a quarter wavelength, maximizing the coherence of the phase.

Having determined the geometry of the reflector, the final characteristic is the feed. An optimal feed design will have a symmetric pattern, be aligned with the phase centre, reduce the cross-polarization of field components, reduce the amount of blockage caused by the feed and the feed mount, and reduce the spill-over and edge diffraction [KRAS-88]. For phase coherence, it is necessary to place the feed at the feed phase center, to ensure that the feed emits a spherical wave front. The determination of the phase centre requires experimental testing.

The basic types of feeds include horns (pyramidal, conical and sectoral), dipole, loop, helix and spiral [KRAS-88]. A horn feed is a simple design, which provides good impedance, polarization and power handling capabilities. However, at S-band frequencies this can be a large feed. The second, and most simple feed, is the dipole, consisting of a simple radiating element. This feed can handle less power and needs a backing to direct the energy to the reflector. A dipole offers good linear polarization, or can be placed in combination, i.e. crossed dipole, to provide a circular polarization. The

loop, helix, and spiral all provide circular polarization and good directivity, but cannot handle high power and are more complex in design.

Before choosing the feed system for the antenna, it is necessary to determine the desired polarization based on the application. If the Earth's surface is considered as a large number of tilted facets, each equivalent to a smooth plane, it is possible to simplify the polarization determination. For all incident angles, except the Brewster angle, a flat plate will reflect the incident energy in a similar polarization for horizontal and vertical linear polarizations, and in an opposite sense for circular polarizations [KRAU-88]. As the system is designed to gather the forward-scattered element, the signal can be assumed to follow the reflecting rules. It is necessary to note that while the majority of the energy will be returned in these generalized polarizations, due to cross-polarization effects and volumetric scattering, as well as the assumption of a flat plane, some responses will be polarized differently, and this will cause a loss in the received energy.

Therefore, given the polarization rules and the nature of the scattering of ice, to maximize the energy received from the reflected signals, a crossed-dipole feed is chosen. If the crossed-dipoles are fed linearly and are electrically controlled, with a quarter-wavelength delay line between them, they can be polarized in a linear format, vertical and horizontal, as well as circular polarization. This will maximize the usefulness of the system, as it will be able to view the ice at different polarizations. Also, it will relax the control constraints placed on the attitude control of the spacecraft and compare. Since the dipoles are able to change polarization, the requirement to keep the spacecraft in the same attitude to ensure similar, in the case of linear, and reverse, in the case of circular, polarizations will be relaxed, as this can be controlled through the feed system. As a straight dipole feed will be an inefficient illuminator, as it has poor directivity, a cavity-backed dipole feed offers a simple design, circular polarization, with a high directivity and efficiency [KUMA-89]. The geometry of the system is shown in Figure 3.9.

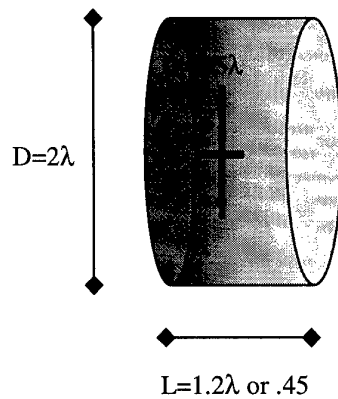


Figure 3.9 Dipole Feed Design [KUMA-89]

At a wavelength of 12.5 cm, the dipole length will be 9.375 cm for the vertical piece. The dimensions of the cavity will be 25 cm for the diameter and 15 cm for the length, with a dipole of  $\frac{3}{4}$  wavelength in the vertical direction and  $\frac{1}{2}$  wavelength in the horizontal direction [KUMA-89]. The resulting radiation pattern will need to be matched to the reflector diameter to ensure a low spillover effect, or a feed pattern taper will need to be applied. The distance of the dipole from the back wall is  $0.25\lambda$ , or 3.125 cm. This is necessary for the radiation reflected from the back wall to be in phase with the forward direction radiation. This antenna feed, if a  $-10$  dB edge taper is applied, will produce side lobes at a  $-16$  dB to  $-24$  dB level, and a total efficiency of 81%.

To accurately determine the characteristics of the antenna system, further work would be required. First, the reflector would have to be built, to determine the errors caused by the imperfections in shape due to the stowing scheme. The feed system would have to be built to accurately determine the edge taper that will be needed and any modifications necessary to the geometry to optimize the feed characteristics. Finally, the feed and reflector systems will need to be combined to test the losses in the system, radiation pattern, and feed phase centre.

### **3.5 On-Board Data Handling and Communications Downlink:**

#### **3.5.1 Data Handling:**

Signal processing is another difficult requirement to meet when attempting to place a SAR system on a micro-satellite. Even the large SAR satellites currently in use, such as ERS-1 and 2, have difficulty in meeting the large amount of storage memory needed and the fast sampling rate.

For the proposed system, the PRF must be above the total spread in Doppler frequency in the azimuth direction:

$$\begin{aligned}\Delta f_i &= \frac{2V}{L} \\ \Delta f_i &= \frac{2 \times 7500}{2.5} = 6000 \text{ Hz}\end{aligned}\tag{3.7}$$

where L is the aperture length in the azimuth direction and V is the satellite's velocity.

While not impractical, a repetition frequency of 6 kHz will require a large data storage capacity for the numerous samples over the 4s imaging period.

Having determined the PRF, the compressed pulse width is found using the desired ground resolution equation:

$$\begin{aligned}\tau &= \frac{2\Delta R_x \cos \alpha}{c} \\ \tau &= \frac{2 \times 30 \times \cos 86.7^\circ}{3 \times 10^8} = 10 \text{ ns} \\ B &= \frac{1}{\tau} = 100 \times 10^6 \text{ Hz}\end{aligned}\tag{3.8}$$

where  $\alpha$  is the compliment of the incidence angle and  $\Delta R_x$  is the ground range resolution. This compressed pulse width of 10 ns, gives a bandwidth for the chirped pulse of 100 MHz.

Once converted to the base-band frequency, the signal is split into two channels, one of which is phase shifted by 90 degrees to form the I and Q channels. These are then

digitized through an A/D converter and sampled at a rate of twice the frequency excursion of the signal, 200 MHz. These samples are passed through the digital signal processor performing the Doppler filtering and the initial signal processing. Due to the limited processing space and time, the data will then be compressed and stored for downlink to a ground station where it will be processed.

For this specific application, the characteristics of the radar system lead to severe performance constraints on the signal processing. Given an original pulse length of 34  $\mu$ s and a compressed pulse of 10 ns, the frequency excursion of the chirped signal is 100 MHz. The sampling rate of twice this frequency, 200 MHz, is applied to both the I and Q channels. Sampling both channels separately gives the effect of a sampling rate of four times the frequency excursion and is sufficient to reconstruct the original signal with only a small error. At this sampling rate, the processor must be able to write to memory at this speed multiplied by the number of bits of each sample (See Table 3.3).

This process is continued for each pulse within the 4 seconds it takes the satellite to fly over a 30 km ground swath, making a total of 24000 pulses. For each pulse, the echo return time is approximately 10  $\mu$ s, corresponding to the difference in the time it takes the signal to travel the shortest slant range to the longest slant range. If the desired ground swath is 30 km, then the corresponding slant range swath is given by:

$$W_s = W_g \sin \theta \quad [3.9]$$

where  $\theta$  is the incidence angle of the system. This leads to a slant range swath width of approximately 3 km, and a sampling window duration of 10  $\mu$ s. Given this, and the duration of the pulse, 34  $\mu$ s, the receiving satellite will record data for 44  $\mu$ s for each pulse. Over the 24000 pulses of the image, this equates to 1.05 s in total.

Table 3.3 shows the resulting channel and picture size for different quantization of the samples without any signal processing or compression.



Sampling Rate= 200 MSps	8 bits	6 bits	3 bits	1 bit
Memory Speed	1600 Mbps	1200 Mbps	600 Mbps	200 Mbps
Channel Size	1690 Mbits	1268 Mbits	634 Mbits	211 Mbits
Image Size	3380 Mbits	2536 Mbits	1268 Mbits	422 Mbits

Table 3.3 Image Size Requirements

### 3.5.2 Data Compression:

Due to the high data rate and consequently the large amount of data, which is collected for each image, the need for data compression is imperative to meet both storage and downlink requirements. The requirements for a compression algorithm for a SAR system are [PARK-99]:

- Good data output quality
- Compression with 2,3 or 4 bits
- High data rate compression
- Low power consumption
- Low mass

In SAR systems, due to the random nature of the returned echoes and the non-correlation between subsequent data points, lossless compression algorithms can gain, at most, a 1.4:1 compression ratio. This is not high enough to reduce the data to adequate levels. Therefore, lossy compression algorithms are used, limiting the compression ratio to maintain good picture quality. The most popular compression algorithm is the Block Adaptive Quantizer, BAQ, and will be used for this system. This is a simple algorithm without complex hardware and is well documented [BENZ-95]. The BAQ also offers a compression ratio of nearly 4:1, and limits the errors caused by losses due to the compression. The BAVQ, block adaptive vector quantizer, begins with the same BAQ algorithm, but places the output of this into vector format and matches this to a codebook and outputs the standard deviation from the BAQ and the codebook address for the vector [BENZ-95]. Other compression algorithms have been examined and used, but become more complex in hardware and therefore negate their benefit for this system.

Kwok et al. first presented the BAQ for the Magellan mission [KWOK-89]. It is an algorithm to estimate the statistics of the source data and attempts to match the quantizer to the observed statistics. Figure 3.10 offers a block diagram of the algorithm.

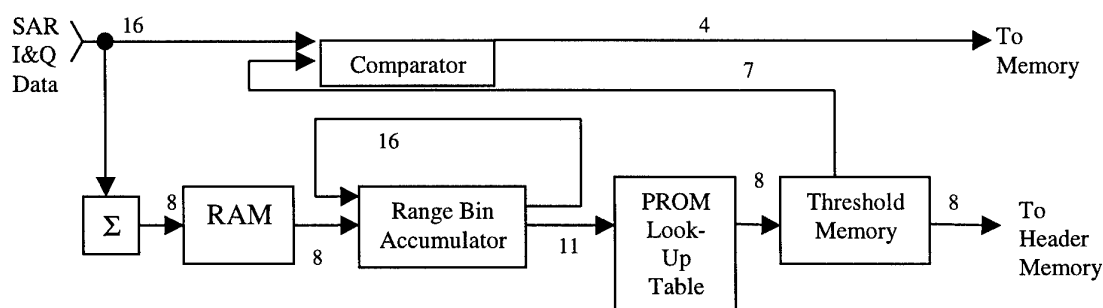


Figure 3.10 BAQ Block Diagram [KWOK-89]

As was found by Kwok et al., the optimum number of range samples per block is easiest and most accurate when limited to the size of one to two range resolution cells, however, as the block must exhibit Gaussian characteristics, the typical size is between 50 to 100 samples. Given this constraint, the simulation result show that a thermal S/N of 8dB was optimal as an increase in S/N did not improve image quality, and a lower S/N degraded it [KWOK-89].

The algorithm is based on the properties of the echo signal. The return from a radar signal is understood to be the super-position of the responses of several small scatterers, i.e. the convolution of the signal with the complex ground reflectivity. The amplitude and phases are statistically independent of each other and of other scatterers within the scene, which leads to the assumption that each range sample is uncorrelated with the previous and preceding sample. The phases can be considered uniformly distributed between  $-\pi$  and  $\pi$  radians [PARK-99]. Given these characteristics of the signal, it can be considered that the real and imaginary parts of the complex radar return signal have a zero-mean Gaussian distribution, unknown average power and uncorrelated real and imaginary parts. This is the basis for the BAQ [PARK-99].

The return signal for the system is modeled as:

$$A(x, y, z) = \sum_1^{N_s} a_k e^{j\phi_k} \quad [3.10]$$

where  $N_s$  is the number of samples per block,  $a_k$  is the reflectance amplitude and  $\phi_k$  is the phase delay. This signal follows the characteristics stated in the previous discussion [KWOK-89].

The first step in the algorithm is to separate the large data block into smaller blocks, where the signal's standard deviation is expected to be roughly constant and the Gaussian statistics within the block are evident [BENZ-95].

Next, the control statistics for the block are estimated. The signals of the I and Q channels are used to find the average signal magnitude, the statistic chosen to characterize the signal [KWOK-89]. The average signal magnitude can be found by:

$$|\bar{I}| = |\bar{Q}| = 2 \sum_0^{N_s-1} \left( x_n + \frac{1}{2} \right) \int_{x_n}^{x_{n+1}} p(x) dx \quad [3.11]$$

$$p(x) = \frac{1}{\sqrt{2\pi}\sigma} e^{-x^2/2\sigma^2}$$

where  $p(x)$  is the Gaussian distribution function,  $x_n$  is the signal magnitude of the  $n^{\text{th}}$  sample, and  $\sigma$  is the standard deviation of the input [KWOK-89]. The threshold setting, the control statistic, is determined by calculating the average signal of the data block for  $N$  samples and Equation 3.11 is used to determine  $\sigma$ . This value is found in a 4 K ROM look-up table, whose 8-bit word output is the header for that series of data compression and contains the control parameter for the block.

The next step is the quantizer, where each 8-bit data sample is encoded into 2 bits using the control parameter found in the previous step (see Figure 3.10 for the block diagram). The data sample is converted into a 2-bit sample based upon the Gaussian distribution and the threshold value. The sample is placed within the limits of the function. The first bit of the output is the sign bit, a 0 for a negative and a 1 for a positive, placing the signal on either side of the statistic function. The second bit places the sample at the centre of a

transition segment to allow for minimum distortion within the reconstructed data [BENZ-95]. It is possible to compress the each data point to 1 bit, but to do this requires a sampling rate of twice that to quantize to 2 bits, and therefore adds no reduction in image size, but increases the complexity of the hardware.

With the final output to the compression algorithm being the 8-bit control statistic, placed as the header to the data stream, and the compressed 2-bit data samples, a compression ratio of nearly 4 is possible. The total output to the system will be 4.4 Mbits of control statistic data, taken for 48 pulses over the 16 time samples. The compressed data is 845 Mbits, at 2 bit samples from the I and Q channels of the compressed pulse. The total compressed data size is 850 Mbits per picture, i.e. a compression ratio of nearly 4:1.

### **3.5.3 Communication Downlink:**

The communication subsystem is responsible for the interaction of the satellite with other satellites and the control, or ground, station. The system functions include receiving commands from the ground station while supplying it with telemetry data and the payload data.

As defined by the orbit, the receiver satellite is in view of a ground station for approximately 15 minutes for an overhead pass. Including a margin for the acquisition of the satellite's signal and the inclusion of the downlink telemetry data, approximately 10 minutes is available to downlink the payload data. For 850 Mbits (as defined by the output of the data compression algorithm) the data rate will need to be 1.28 Mbps. Therefore, the 2 Mbps link provided as standard with the spacecraft will be more than adequate.

At 700 km altitude, the slant range to the ground station varies from just over 3000km when the satellite is at 0° elevation, to 700 km when the satellite is directly overhead. This is shown in Figure 3.11.

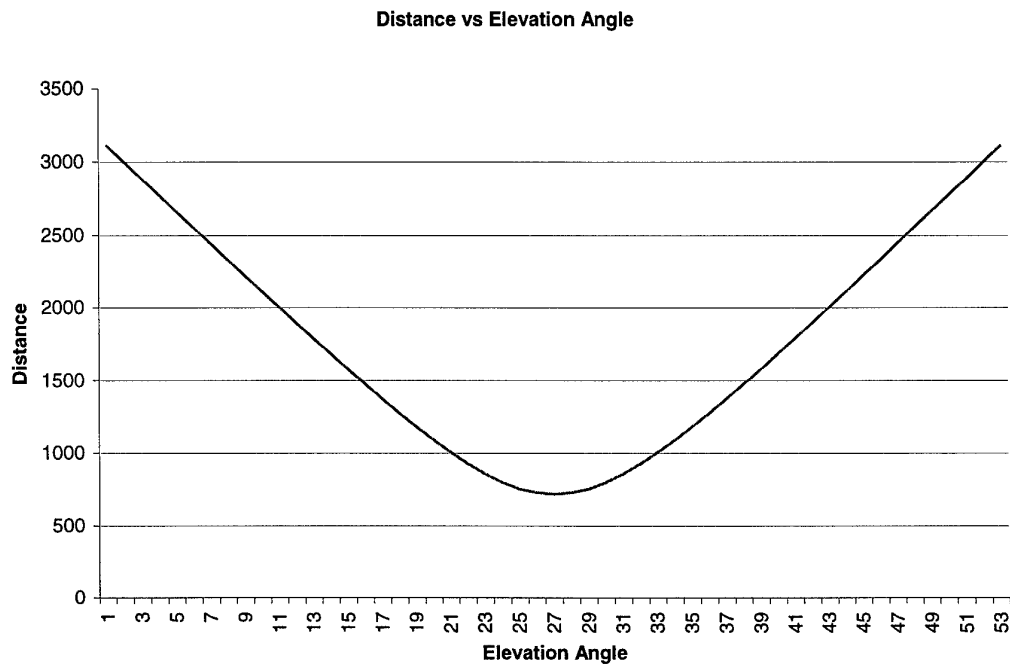


Figure 3.11 Relationship of the Distance to the Ground Station  
with respect to the Elevation Angle

If the satellite must be acquired on the horizon, the effective isotropic radiated power (EIRP) will need to be higher than if it was acquired at a higher elevation angle. This becomes known as the system margin. For the geometry of this system, with a 0dB antenna on the satellite, the change in the system margin is shown in Figure 3.12. From this graph, it is seen that if the satellite is acquired at the horizon, there will be a margin of 16 dB when the satellite is directly overhead. It is possible to design an antenna, which has a variable gain over the elevation angles so as to reduce this and this optimizes the system.

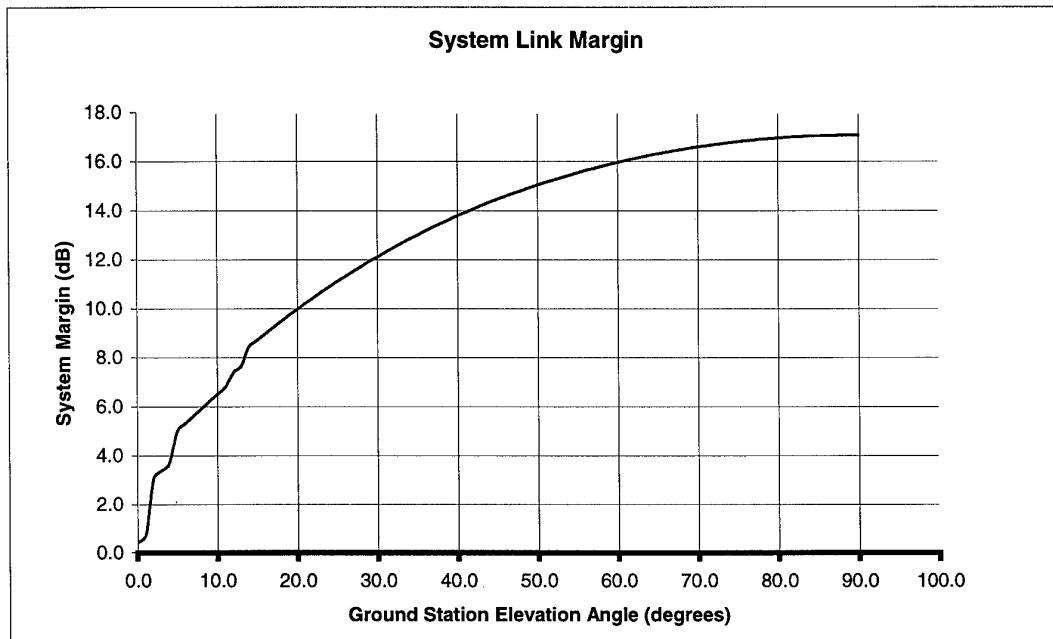


Figure 3.12 System Margin with Acquisition at Horizon

Before forming the link budget for the communications subsystem, it is necessary to describe the assumed values for certain variables. The frequency of the downlink is also as 2.4 GHz, the same as that of the payload. The receiving antenna is assumed to be a 2.5 m diameter dish antenna, the antenna used by the SSTL ground station. The receiving antenna will therefore have a gain of approximately 30 dB at an efficiency of 50%. Finally, the total system losses for the downlink system are estimated to be 10 dB with a 3 dB margin. Given these assumptions and the system constraints, it will be possible to determine the link budget for the data downlink.

The modulation scheme for the downlink has been chosen as Quadrature Phase Shift Keying (QPSK) was chosen due to its high use of spectrum, thus reducing the bandwidth necessary, and the lower value for the bit energy to noise spectral density requirement. QPSK offers a spectrum utilization of 2.0 bps/Hz [WERT-92]. Given this value, the bandwidth chosen is 1 MHz, allowing for a 2 Mbps downlink, providing a comfortable margin.

Also, given the need for accurate data transmission without large numbers of bit errors, the BER, bit error rate, must be no more than  $10^{-6}$ . This requires a received energy per bit to the noise spectral density,  $E_b/N_o$  to be 10 dB where  $E_b/N_o$  is

$$E_b/N_o = \frac{P_t G_t G_r \lambda^2}{4\pi R^2 k T_s R_{\max}} \quad [3.12]$$

where the subscripts t and r stand for the transmitter and receiver, respectively, R is the distance from the transmitter to the receiver, k is the Boltzmann's constant,  $T_s$  is the system temperature,  $L_s$  is the system losses, and  $R_{\max}$  is the data rate [MARAb-93].

This constraint, in turn, defines the carrier-to-noise density ratio,  $C/N_o$ , to be:

$$C/N_o = \frac{E_b/N_o}{R_{\max}} = \frac{P_t G_t G_r \lambda^2}{4\pi R^2 k T_s L_s} \quad [3.13]$$

If  $C/N_o$  is subsequently divided by the bandwidth of the system, the result is the C/N, thus defining the characteristics of the downlink [MARAb-93]. In the link design, the transmit power, system bandwidth and the C/N must all match to allow for system requirements.

Table 3.4 gives the complete link budget design for the system. This budget is designed with a constant gain antenna for acquisition at the horizon. The losses of the system are estimated from results of testing.

Orbit Height		Km	700.0
S/C Antenna Nadir Angle		Degrees	64.3
Range to Spacecraft	R	Km	3069.1
Total Time	Tp	Seconds	917.9230667
Frequency Of Operation	Fc	MHz	2400.0
Transmitter Power Output	Po	W	6.0
Transmitter Power Output	Pt	dBW	7.8
Feed Loss	Lf	dB	1.62
Antenna Absolute Gain	Gt	dBi	0.0
EIRP	EIRP	dBW	6.7
Free Space Loss	FSL	dB	169.8
Additional Atmospheric Losses	Latmos	dB	0.5
Power Flux Density At Ground	PFD	dBW/m2/4KHz	-160.3099565
Power Flux Density Limit	PFD	dBW/m2/4KHz	-154
Power Flux Density Margin	PFD	dB	6.309956461
Receiver System G/T	G/T	dBW/K	10.4
Boltzmanns Constant	K		-228.6
System Performance Requirements			
Data Rate	Rb	bps	2000000.0
Modulation Type	Coherent PSK, QPSK		
Modulation Spectral Efficiency		bps/Hz	2.0
Bandwidth		Hz	1000000.0
Eb/No		dB	10.55
Coding Gain	Viterbi K=7	dB	5.20
Implementation Loss		dB	1
Required Eb/No			6.35
System Eb/No		dB/Hz	6.7
System Margin		dB	0.4

Table 3.4 Link Budget for Communication Downlink



## **3.6 Satellite Synchronization:**

### **3.6.1 Time:**

A key element in the synchronization of the two systems is based on accurate timing. In bi-static SAR, accurate timing can also be used to measure of the baseline distance between the transmitter and receiver. There needs to be synchronized clocks on both the transmitting and receiving satellite. If there are errors in the clock times, this will cause errors both in the range resolution, resulting in image de-focusing. In a mono-static SAR system, the time synchronization is simple, as the components are linked to a common clock source. However, in bi-static SAR, transmitter and receiver subsystems are on separate platforms, therefore, the clocks must be kept synchronized, either one to the other, or both to an outside master clock, for example, one derived from the GPS satellite network.

As the satellites will be using a GPS receiver in the guidance and navigation system, it is logical to slave both on-board clocks to the time on the GPS receiver. This will require a clock stability on the order of a fraction, typically  $\frac{1}{4}$ , of the transmitted compressed pulse width [WILLd-91]. In this system, the clock stability during the imaging time of 4 s, with the required time accuracy of 2.5 ns, is  $6.25 \times 10^{-10}$  or about 2 parts per  $10^9$  for 4 s. This stability is easily achievable with current technology of quartz clocks [WILLd-91].

As the relative time in the system, i.e. the time of the transmitting clock and the time of the receiving clock, is important, and not a universal time, the GPS clock biases will not introduce errors into the system. However, the difference in propagation time between the GPS satellite and the transmitting and receiving satellites will cause the two clocks to be offset by an error. To remove this error from the timing, it is necessary to use a pulse delay ranging between the two satellites.

The transmitting satellite, as the master satellite, will be assumed to have the correct time. As the transmitter transmits its pulses, a -20 dB splitter will be used to transmit to the

receiver a copy of the pulse. The transmitter will start transmitting at time  $t_0$ , which is known on both the satellites. The receiving satellite will receive this ranging sample at the time  $t_0 + t_{\text{travel}} + \epsilon$ , where  $t_{\text{travel}}$  is the actual time for the signal to travel the baseline and  $\epsilon$  is the error in the receiver time compared to the transmitter. However, the receiver will assume that the pulse was transmitted at time  $t_0$ , and will interpret the travel time as  $t_{\text{travel}} + \epsilon$ , and compute a baseline distance from this. It will compare this distance to that determined by the GPS receiver. The differences in this value will mainly be the result of the clock error, with a small error due to the inaccuracy of the GPS measurement, i.e. a few cms. This process can be continued through the imaging time so that an accurate value of the change in the baseline can be determined, and the clock error can be held to a minimum. Furthermore, the clocks can be synchronized prior to the start of imaging, so that no corrections for clock error will need to be made during signal processing by the ground station.

### **3.6.2 Phase:**

Similar to mono-static systems, the transmitter and receiver need to maintain a high level of phase stability to ensure coherence within the system. This translates to stability of the local oscillator. However, this stability will need to be over the coherent integration time of the system, approximately 0.23 s, as there will be possibility for re-synchronizing the system during each integration time. Also, due to the distributed nature of the system, the total stability is the sum of the individual stability of the transmitting local oscillator and the receiving local oscillator. Given the possibility of a  $5^\circ$  phase error for the entire system, the total stability for the oscillators is  $2.3 \times 10^{-11}$ . This translates to an error of  $1.15 \times 10^{-11}$  for each oscillator over the 0.23 s integration time. This stability is possible with the quartz clock [WILLd-91].

### **3.6.3 Signal:**

Perhaps the most challenging aspect of synchronization of the transmitter and the receiver is the synchronizing of the signal. As stated previously, the on-board receiver will be

responsible only for down-converting the signal, dividing into I and Q channels, digitizing and storing the data. However, to accomplish this, the receiver must have an accurate copy of the transmitted pulse. This can be done directly from receiving the transmitted pulse and correcting for Doppler shifting and propagation errors to use it as the mixing signal. However, this approach will always add errors to the system, thereby, reducing the quality of the system raw data. The use of Direct Digital Synthesis, DDS, solves this problem.

The concept behind DDS is to store in memory, a digital copy of the waveform, or subsequently to store look-up tables for the phase, frequency and amplitude values, and store those addresses [GALL-88]. In effect, it replaces the analog exciter, responsible for producing the linear FM chirp waveform, with a digitally stored version. The DDS system would require high-speed random access memory to store the digital waveform and a high-speed digital to analog converter (DAC) [GALL-88]. The DAC of the system would output the analog base-band version of the desired waveform, which would then be up-converted to S-band for use. Testing results from such systems, show that it is possible to get near theoretical waveform generation, including a RMS phase error of  $1.4^\circ$  [GALL-88].

Using a DDS system would provide, a near theoretical waveform generated from the transmitter, and, with an identical system placed on the receiver, would provide a near-exact replica of the transmitted pulse to down-convert the signal. This system would limit the amount of errors introduced into the system by the distribution of the transmitter and receiver. The DDS signal can also be stored in the ground station for processing, updated with error readings from the transmitting satellite.

### **3.7 Ground Segment:**

Having stated the requirements and operations of the satellite-based portion of the SAR system, the ground segment completes the system, as the processing of SAR data is too complex and time consuming to be done on-board the spacecraft.

In order for the ground station to act as an effective correlator and processor for the SAR data, the following information concerning the spacecraft platform and SAR system performance must be known: antenna characteristics, the data rate from the satellite, the bit error rate (BER), the sampling frequency of the data and thus the number of samples per range line, the range bandwidth, the PRF, pulse duration and coding scheme for the radar pulse, the orbit characteristics of inclination and altitude, and the position, velocity, attitude and attitude rate accuracies of the spacecraft. Of these parameters, many are set values for the system—antenna characteristics, data rate and BER, sampling frequency, PRF, pulse duration, and coding scheme—and may be known by the system before the acquisition of the satellite.

Upon acquisition of the satellite, the ground station will maintain a communications link with the satellite for the total view time. This requires an antenna of a gain of 30 dB for the link budget designed. The ground station will receive the modulated downlink signal, down-convert the signal and demodulate it at a data rate of 2 Mbps. Once the data is demodulated, it must be stored for processing, requiring storage of 850 Mbits of data, written to memory at 2MHz. These requirements for the system are well within the limits of current technology.

Once the signal has been uncompressed, the processing of the SAR data begins. As there are no constraints on the time, the speed of the processor is not a constraint on the system.

The first step in the processing will be to decode the compressed raw data, using an inverse BAQ algorithm. This process consists of separating the data into the original

blocks by locating each header. The 8-bit header data is then passed through the threshold look-up table to find the threshold value. This is then applied to each of the 2-bit I and Q samples such that:

$$y_n = \begin{cases} (sign)x0.52xTh \\ (sign)x1.73xTh \end{cases} \quad [3.14]$$

where  $y_n$  is the sample, sign is given by the first bit, the magnitude, 0.52 or 1.73, is given by the second bit and  $Th$  is the threshold value, or signal statistic. The magnitude values of 0.52 and 1.73 are the centre points of the quantizer outputs, which minimize distortion.

The raw SAR data has now been recovered, with some loss due to the compression algorithm, and is now ready for SAR processing. This is fully explained in section 2.4.7.

The raw data must first be pulse compressed, which consists of using a matched filter correlator. To do this, the ground station must have an accurate copy of the transmitted pulse, which is gained through DDS of the pulse waveform. This will allow for an accurate replica, in phase and amplitude, of the transmitted pulse to be simulated, and therefore, maximize the S/N of the output of the filter. If more accurate phase information is necessary for processing, once the DDS system has been tested, it is possible to update the digital signal with the errors caused by the transmitter hardware. As the digital signal is passed through the analog system and the transmitter and antenna hardware, phase errors are introduced, which, if uncorrected for in the correlating signal, will cause errors in the system. To remove these errors from the system, the transmitter can record a copy of each pulse, or record the differences in phase and amplitude as compared to the DDS signal for each pulse, and transmit this information to the ground segment. The ground segment will then use this information to update the ground DDS signal for accurate correlation.

The pulse-compressed data is then processed through the range and azimuth algorithms, allowing for image defect correction. Figure 3.13 offers a block diagram of the processing flow. Unlike the constraint of time for on-board processing, the operational

requirements of the speed of the processor are based on the amount of processing done, to include phase corrections and auto-focusing, and how fast the final image is needed.

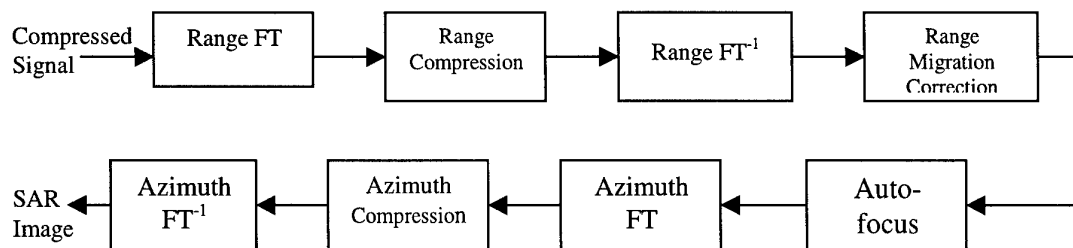


Figure 3.13 SAR Processing Flow

## **Chapter 4 Mission Design:**

### ***4.1 Satellite Design:***

#### **4.1.1 Choice of Satellites:**

The satellite design chosen for the project is the Surrey Satellite Technologies, Ltd. (SSTL) enhanced micro-satellite modified to a truncated pyramid shape. The decision to use a pre-designed satellite was due to the objective of producing a low-cost satellite, which would be readily available to everyone. By choosing a pre-fabricated, modular design, the spacecraft can be manufactured within the specifications of the customer without requiring a large increase in cost or production time. The SSTL enhanced micro-satellite has been designed with a highly modular structure for the purpose of rapid and low-cost adaptation to accommodate different payloads and missions [WICK-01].

This design is based upon SSTL's long heritage of small satellites, specifically the UoSAT missions, CERISE, TMSAT and CLEMENTINE. It is a design, which is well proven and, due to the modular sub-systems, allows for increased power, mass and volume from the previous missions. The modular design of the satellite will also allow for upgrades of the satellite with advancement in the state-of-the-art.

#### **4.1.2 Satellite Structure:**

The design consists of a truncated pyramid structure with dimensions of a 1x1 m base with a height of 600 mm. The mass of the satellite is 100 kg, with 40 kg allocated to payload mass. The satellite is specifically designed for low Earth orbits and is compatible for launch on most major launch vehicles. The basic design was used in the GANDER radar altimetry constellation design [WICK-01].

The reason that the structure is in the form of a truncated pyramid is due to the orientation requirement of the solar panels. By using body-mounted solar panels, there is a reduction in the complexity of the spacecraft by not requiring the deployment of the solar panels. However, in a typical cube design, the orientation of the solar cells to the sun is not optimal, therefore producing less power per array than is possible. Using a pyramidal shape with a  $30^\circ$  orientation to vertical gives an increase in the solar panel area by approximately 30% (given standard solar cells) when the satellite is correctly aligned and outside of eclipse, which can increase the output power by approximately 60%, in a sun synchronous orbit. Figure 4.1 offers a depiction of the enhanced micro-satellite in the traditional cube and truncated pyramid shapes.

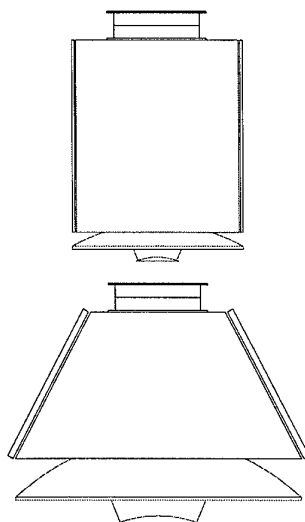


Figure 4.1 Enhanced Micro-Satellite Design with Cubic  
And Truncated Pyramid Shape [MEER-01]  
(antenna not to scale)

The truncated pyramid shape also provides the benefit of an extended base allowing for a larger mounting area for the 2.5 m diameter antenna. This will reduce the total volume of the spacecraft in the launch configuration, i.e. with stowed antenna. In launch configuration, the total volume of the satellite is 1x1 m for the base and a 1.75x1.75 m area for the top, to accommodate for the antenna width. The satellite will be 0.6 m in



height, and the stowed antenna will be 0.75 m in height. The spacecraft will, therefore, need to be mounted to the launch vehicle with an extended attach fitting cone, as the attachment site is the top of the satellite. The total volume for launch will need to be approximately 4 m<sup>3</sup> to allow for sufficient spacing.

The modular structure of the satellite is shown in Figure 4.2a and 4.2b. Figure 4.2a provides the basic internal structure to show the placement of the modular sub-systems within the satellite. Each dark cube represents the placement of possible systems. The total volume allocated to the payload module is 1x1x0.3 m.

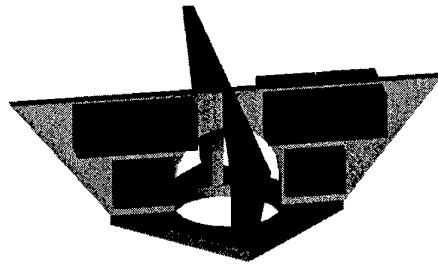


Figure 4.2a Basic Modular Design [MEER-01]

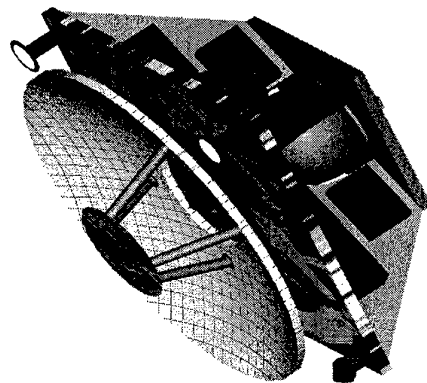


Figure 4.2b Modular Design [MEER-01]

Figure 4.2b shows the complete satellite without side panels. The antenna in this figure is not designed to scale to allow for a full view of the internal structure. This design allows for the benefits of a modular design stated above, and also provides an additional benefit in that the propulsion system can be varied to meet the mission requirements. Figure 4.3 shows the different propulsion systems, to be discussed in a later section that is possible for the satellite.

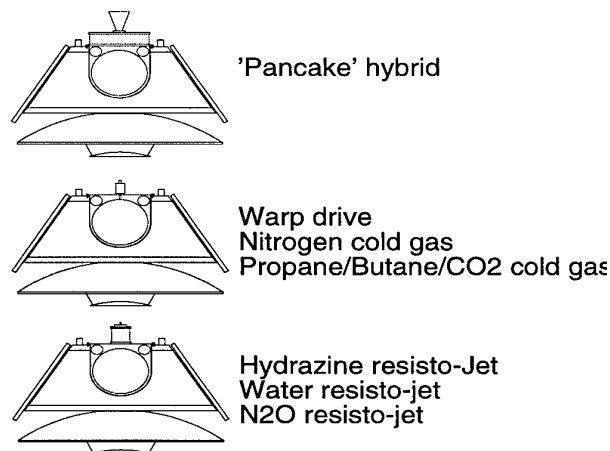


Figure 4.3 Proposed Propulsion Systems [MEER-01]

### 4.1.3 Power System:

As the most stringent constraint on the satellite, the power system is critical.

The satellite can be made with 4 body mounted Silicon (Si) or Gallium Arsenide (GaAs) solar panels, which produce 70 W and 100 W, respectively, for each panel. This allows for a peak power of 110W and 140 W, respectively. The efficiency of GaAs solar cells is achievable at 18% versus a 14% efficiency for Si [LARSb-92]. Also, the GaAs cells are more resistant to radiation effects and have a better response over a larger temperature range. The increase in the power generation performance of the GaAs cells over the Si cells well merit the increase in cost, which accompanies the upgrade.

The satellite is designed with a Nickel Cadmium, NiCd, battery pack providing a total of 200 Wh at a maximum of 28 V. NiCd batteries have long been used in small satellite applications, especially in low-Earth orbits. NiCd batteries have shown to have a lifetime

in LEO of up to 90,000 cycles [LARSb-92]. These batteries are easy to procure, low-cost, and have a high level of reliability and flexibility. The specific battery pack can be custom designed for the mission, again due to the modular design of the satellite. The total peak power drain from the satellite may be up to 1 kW.

#### **4.1.4 Guidance, Navigation and Attitude Determination and Control:**

The Attitude determination and control system, ADCS, of the satellite is another system, which is critical to the SAR system payload, as any error in pointing and positioning causes errors in the payload performance.

Conventionally, the ADCS of the satellite bus is equipped with multiple sensors—sun, horizon and star sensors, magnetometers, and gyros, and multiple actuators—reaction wheels and torque coils. This allows for a 3-axis stabilized spacecraft. For the enhanced satellite design, sun and horizon sensors are used in combination with a tri-axial magnetometer.

The sun sensor, a 2-axis, low-cost attitude determination sensor, is well proven in low-Earth orbits. The sensor measures the sun angle in both the azimuth and the elevation and determines the orientation of the satellite based upon these values. Figure 4.4 shows an example of the sensor. The total power consumption of the system is less than 100mW when in sunlight. The proposed accuracy of the system is  $0.5^\circ$  for  $3\sigma$ . Operationally, this sun sensor module has been flown on SSTL's Tsinghua satellite and achieved an accuracy of  $1^\circ$  in nadir pointing [STEY-01].

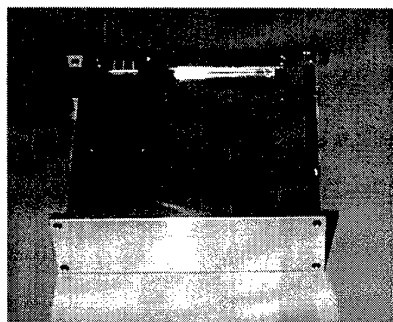


Figure 4.4 SSTL 2-Axis Sun Sensor [STEI-01]

The horizon sensor uses the relationship of the satellite to the horizon presented in the sensor to determine the orientation of the satellite. It provides a 2-axis determination of the attitude, i.e. it determines the pitch and roll axis, but not the yaw axis. Within a  $\pm 5^\circ$  angle off the horizon, the attitude can be determined by less than  $0.06^\circ$  [STEY-01]. Figure 4.5 shows a figure of the horizon sensor used by SSTL.

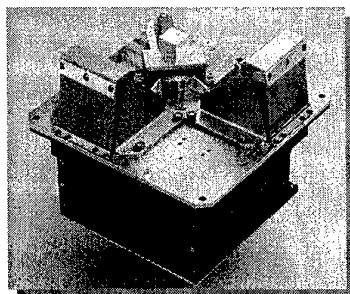


Figure 4.5 Horizon Sensor [STEY-01]

The actuators for the ADCS are momentum wheels providing 3-axis stabilization. The momentum wheels can be seen on the Figure 4.2 as the cylinder on the left side of the structure. These actuators provide control of  $0.25^\circ$  on the roll axis,  $0.4^\circ$  in the pitch axis and  $0.5^\circ$  in the yaw axis. Again, these values were shown on the Tsinghua satellite [STEY-01].

The guidance and navigation of the satellite is provided by an on-board GPS receiver, specially designed by SSTL for operations on small satellites. GPS can provide a position accuracy of  $\pm 15$  m when operated in normal mode. It is possible to use GPS in a differential mode, which can, theoretically, provide cm level position accuracy. Figure 4.6 shows the ADCS and GPS module for the spacecraft.

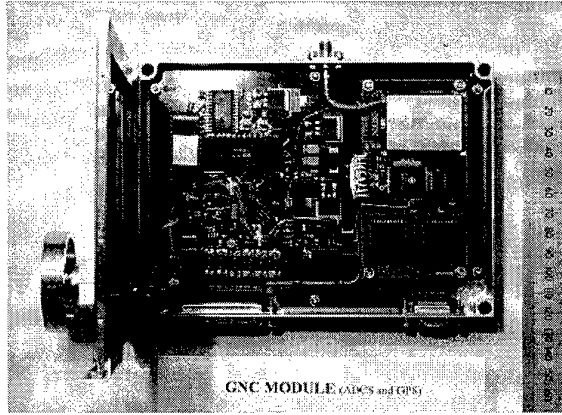


Figure 4.6 GPS Module for an Enhanced Micro-satellite

#### **4.1.5 Command, Data Handling and Communications:**

The command, data handling and communications subsystem of the satellite must operate at a high efficiency level due to the computational demands of the radar payload and will need to be specifically designed for this project. Chapter 3 provided requirements for this system.

The designed uplink for the system is an S-band receiver with 16-128 kbps data rate with Binary Phase Shift Keying (BPSK) coding. This is an adequate uplink design. There are no requirements placed on the uplink design by the payload, except that the ground station cannot use the uplink during imaging periods. Also, as the uplink and downlink are the same frequency, a redundant uplink in the L-band can be included, should the need arise.

The downlink of the satellite is designed as an S-band transmitter with a 2Mbps data rate at a power output of 6 W. It provides a QPSK modulation scheme with a Viterbi error algorithm coding. This design meets the payload requirements.

The antenna for the uplink and downlink will be an S-band helical antenna. The dimensions of this antenna have been given in section 3.4.3. The antenna will be placed on the back of the cavity for the SAR antenna. This will provide near-nadir pointing for the antenna.

Figures 4.7 and 4.8 provide an artistic rendering of the proposed spacecraft, in launch and deployed configurations, respectively. The antenna is shown with all four panels stowed in a launch position, as well as two opposite panels extended in the deployed position, to give an idea of the size of the deployed antenna with respect to the spacecraft.

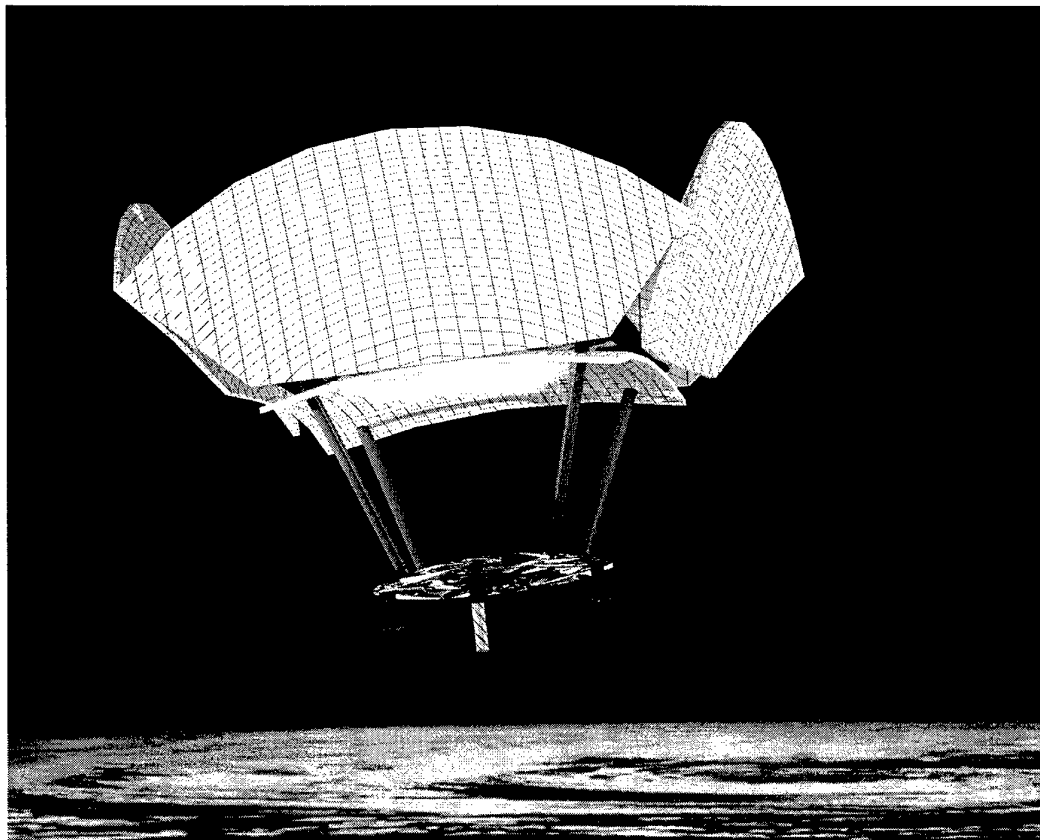


Figure 4.7 Launch Configuration for the Satellite

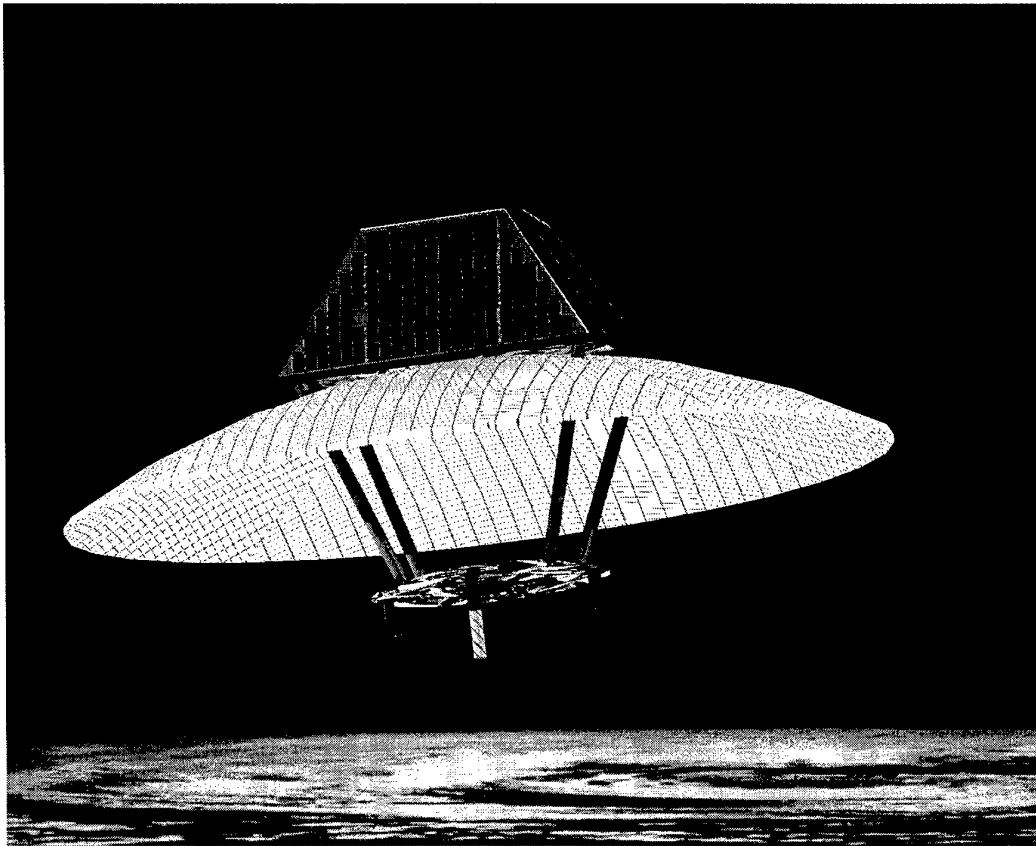


Figure 4.8 Deployed Configuration of the Satellite

## **4.2 Formation and Orbit Design:**

### **4.2.1 Basic Orbit Design:**

The first design consideration for the constellation concerns the positioning of the satellites in such a way such that the receiver detects the forward-scatter of the transmitter and each point in the image is fully resolvable, i.e. there is only one intersection between the isorange and iso-Doppler contours. The geometry of the orbits is shown in Figure 1.1a and 1.1b.

As was stated in the bi-static radar discussion, the isorange contours are confocal ellipses where the semi-major and semi-minor axes are based upon the baseline—the distance

between the transmitter and receiver. However, the iso-Doppler contours of a bi-static system, while still focused on the position of the transmitter and receiver, do not follow the confocal hyperbolas of the mono-static system, but are a complex series of conic contours.

The following graph shows the relationship of the contours for the proposed formation of the satellites:

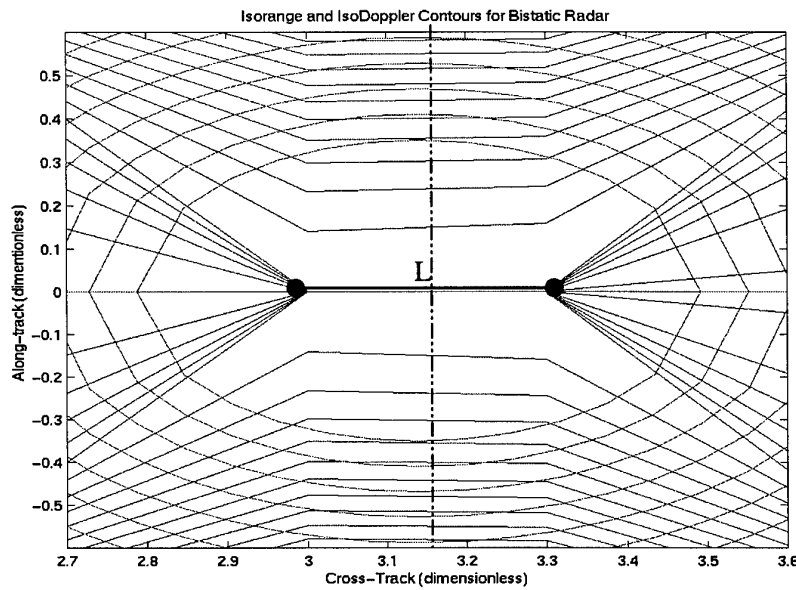


Figure 4.9 Isorange and Iso-Doppler Contours

where ovals represents the isorange and intersecting lines to the ovals represents the iso-Doppler contours. The thick solid line is to show the baseline between the transmitter and receiver and the thin, dashed line shows the bi-static bisector.

Again, there are two intersections between the contours. However, the bisector of the baseline separates the points, with one intersection on the right and one on the left. Since the system only images on one side of the bisector, this resolves the left-right ambiguity, making each target unique in its echo return.



The orbits for the formation have been chosen to be virtually sun-synchronous, circular, low Earth Orbits (LEO), at an altitude of 700 km. The requirements for the inclination of each orbit will be constrained only by the need for the transmitter orbit to be inclined 0.5 degrees more than the receiver orbits, as defined in the constellation geometry (see Figures 1.1a and 1.1b). The orbits will need to be sun-synchronous to meet the power constraint of the system, and the equatorial crossing times must be chosen to maximize the power production. This is assuming no perturbations within the system. Later analysis will show that this assumption is not valid.

Given these orbital parameters, the period of the orbit is 98.8 minutes, approximately 14.5 orbits per day. Figure 4.10 and 4.11 give a view of the satellite's orbits over a one day time propagation. This propagation is for the theoretical model only and does not contain any orbital perturbations.

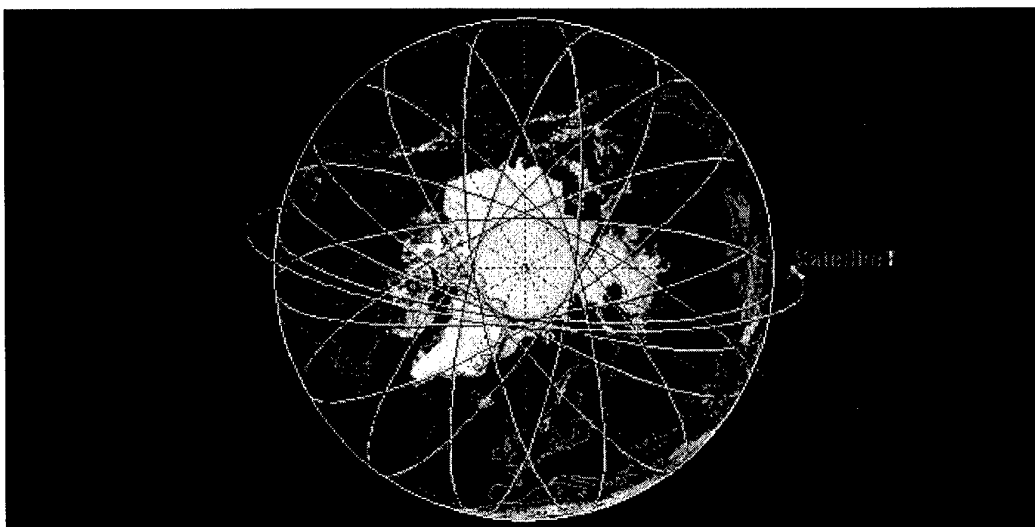


Figure 4.10 Polar View of Satellites' Orbits

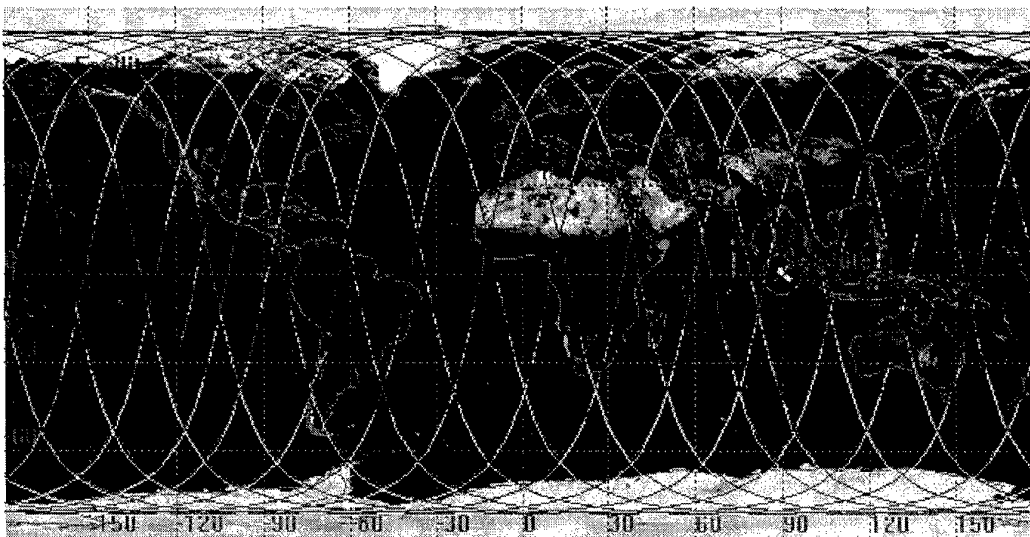


Figure 4.11 Ground Tracks of the Satellites

#### 4.2.2 Relative Motion Analysis:

Having determined the orbits and formation configuration for the system, the relative position and motion between the receiving and transmitting satellites is necessary to determine the time when the satellites are in a configuration for imaging.

To obtain the relative motion between the satellites, the Hill's equations (Clohessy-Wiltshire equations) are used. The solution to these equations relates the motion and position of one spacecraft, named the chase vehicle, with respect to the target vehicle. For the purposes of this study, the target vehicle will be the transmitting satellite and the chase vehicle will be the receiving satellite. The coordinate systems for this system is based on a local XY frame centered on the target satellite with the x direction being the radial, y direction being tangential to the orbit, and the z direction defined by the right-hand rule, out of the XY plane. These equations provide an analysis of the system based on the assumption of a perfectly spherical Earth with no perturbations or drag.

The orbit of the target vehicle in the inertial frame is a radius  $R_o$ , which is constant due to the circular orbit. The orbital rate of the spacecraft, mean motion, is defined by:

$$n = \sqrt{\mu_E / R_o^3} \quad [4.1]$$

where  $\mu_E$  is the gravitational constant of the Earth. This is the angular velocity of the coordinate system centered on the vehicle, with respect to the inertial Earth-centered frame.

Therefore, the position vectors of the two spacecraft defined in the inertial system are:

$$\begin{aligned} R_t &= R_o \hat{i} \\ R_c &= (R_o + x)\hat{i} + y\hat{j} + z\hat{k} \end{aligned} \quad [4.2]$$

where x, y and z are the coordinate position of the chase vehicle with respect to the target vehicle, and the subscripts t and c relate to the target and chase vehicles, respectively.

The inertial acceleration of the chase vehicle is then found to be:

$$\ddot{R}_c = [\ddot{x} - 2n\dot{y} - n^2(R_o + x)]\hat{i} + (\ddot{y} + n\dot{x} - n^2y)\hat{j} + \ddot{z}\hat{k} \quad [4.3]$$

The gravitational acceleration of the chase vehicle in the inertial frame is given by:

$$\vec{g} = -\frac{\mu_E}{R_o^3} \vec{R}_c = -\frac{\mu_E [(R_o + x)\hat{i} + y\hat{j} + z\hat{k}]}{[(R_o + x)\hat{i} + y\hat{j} + z\hat{k}]^3} \quad [4.4]$$

This equation can be simplified for small relative motions, where  $x^2 + y^2 + z^2 \approx 0$ , and the generalized binomial theorem, neglecting second-order terms. The acceleration is then considered:

$$\vec{g} \approx -n^2[(R_o - 2x)\hat{i} + y\hat{j} + z\hat{k}] \quad [4.5]$$

In this reduced form, the two acceleration equations for the chase vehicle can be resolved into component form:

$$\begin{aligned} \ddot{R}_c &= \vec{g} \\ (\ddot{x} - n^2 R_o - 2n\dot{y} - n^2 x)\hat{i} &= (R_o - 2x)\hat{i} \\ (\ddot{y} + 2n\dot{x} - n^2 y)\hat{j} &= -n^2 y\hat{j} \\ \ddot{z}\hat{k} &= -n^2 z\hat{k} \end{aligned} \quad [4.6]$$

The final Hill's equations are found by solving for each coordinate direction:

$$\begin{aligned}
\ddot{x} - 2n\dot{y} - 3n^2x &= 0 \\
\ddot{y} + 2n\dot{x} &= 0 \\
\ddot{z} + n^2z &= 0
\end{aligned}
\tag{4.7}$$

From these general equations, the update matrix can be found relative to time and the previous position and velocity. The update matrix of the in-plane motion is determined to be:

$$\begin{bmatrix} x(t) \\ y(t) \\ \dot{x}(t) \\ \dot{y}(t) \end{bmatrix} = \begin{bmatrix} 4 - 3\cos(nt) & 0 & \sin(nt)/n & 2(1 - \cos(nt))/n \\ 6\sin(nt) - 6nt & 1 & 2(-1 + \cos(nt))/nt & 4\sin(nt)/n - 3t \\ 3n\sin(nt) & 0 & \cos(nt) & 2\sin(nt) \\ 6n(-1 + \cos(nt)) & 0 & -2\sin(nt) & -3 + 4\cos(nt) \end{bmatrix} \begin{bmatrix} x_o \\ y_o \\ \dot{x}_o \\ \dot{y}_o \end{bmatrix} \tag{4.8}$$

where  $\begin{bmatrix} x_o \\ y_o \\ \dot{x}_o \\ \dot{y}_o \end{bmatrix}$  is the matrix of the previous position and velocity.

As can be seen from the Hill's equations, the out-of-plane motion,  $z$ , is decoupled with the in-plane motion,  $x$  and  $y$ .

Therefore, the solution of out-of-plane motion is:

$$\begin{bmatrix} z(t) \\ \dot{z}(t) \end{bmatrix} = \begin{bmatrix} \cos(nt) & \sin(nt)/n \\ -n\sin(nt) & \cos(nt) \end{bmatrix} \begin{bmatrix} z_o \\ \dot{z}_o \end{bmatrix} \tag{4.9}$$

where  $\begin{bmatrix} z_o \\ \dot{z}_o \end{bmatrix}$  is again the previous position and velocity.

Specific to this project, the decoupled nature of the in-plane to out-of-plane motion greatly simplifies the problem of determining the relative position of the transmitting satellite to the receiving satellite. The orbits of both satellites are circular orbits with a radius of 7078 km. The only variation between the two orbits is the inclination of

approximate  $0.5^\circ$  of the transmitting satellite's orbit. This, therefore, given us initial conditions in the in-plane motion of a zero matrix, stating that the relative to the receiving satellite, the in-plane motion of the transmitting satellite is identical. The only relative motion of the one satellite to the other is out of plane.

The out-of-plane motion of the transmitting satellite with respect to the receiving satellite in the time domain can be simplified to:

$$\begin{aligned} \dot{z}(t) &= A_n \cos(nt - \phi) \\ z(t) &= A \sin(nt - \phi) \end{aligned} \quad [4.10]$$

where  $A_n$  and  $A$  are coefficients of the system, based upon the maximum distance between the transmitting and receiving satellites during the orbit ( $A_n = A \times n$ ) and  $\phi$  is the phase difference of the separation of the satellites at start time.

When these equations are applied to the proposed constellation, it is possible to determine the relative position and velocity. The assumptions used to simplify the equations are a perfectly spherical Earth and no perturbing forces. This simulation was run, starting at the crossing of the equatorial plane. In this case, the crossing of the equatorial plane coincides with the intersection of the transmitter and receiver orbit. The relative position of the satellites is shown by:

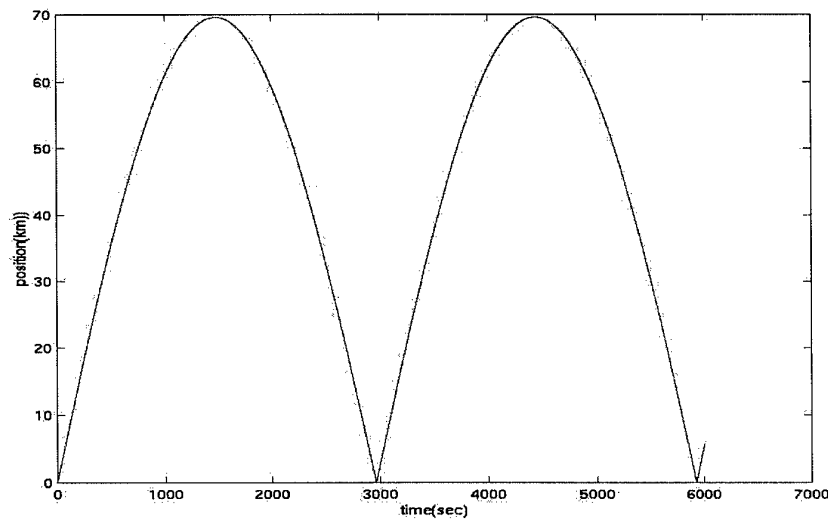


Figure 4.12 Relative Position

The relative position between the satellites must be greater than 60 km for imaging to occur. This separation takes place at two intervals: 990-2020 seconds and 4020-5050 seconds from the start of the simulation. In the configuration of the simulation, this would be made to coincide with the polar regions of the earth.

The relative velocity is:

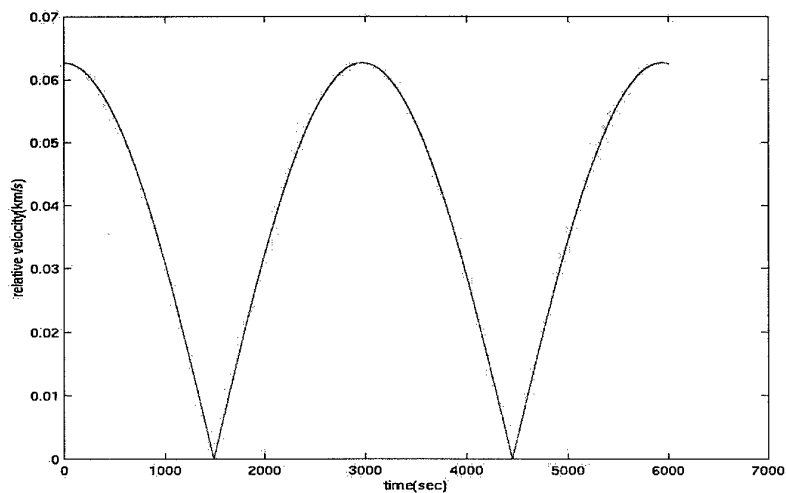


Figure 4.13 Relative Velocity

As can be seen from these graphs, as the formation approaches the maximum separation the relative velocity slows to zero. Needing approximately 4 seconds for imaging, it is optimum, for image quality, to image when the relative velocities are slowest. This occurs at 1510-1525 and 4540-4555, where the relative velocity is 25 cm/s going to zero and back to 25 cm/s by the end of the interval. Again, this corresponds to the Polar Regions.

### **4.2.3 Orbital Perturbations:**

There are a number of assumptions when deriving the Keplerian orbits, which were used in the above study, that are not valid for operational use: perfectly spherical Earth, no drag and only two-body gravity effects. To determine the total required  $\Delta V$  budget for the satellites, it is necessary to remove these assumptions, propagate the orbits forward in time and determine the necessary velocity burns required to maintain the formation.

#### **4.2.3.1 Non-spherical Earth:**

The perturbation caused by the non-spherical shape and non-homogeneous distribution of mass is often referred to as the  $J_2$  effect. The Earth contains a "bulge" at the equator and a flattening at the poles, giving the Earth a slight pear shape. This disrupts the theoretical potential function of the Earth, and consequently the satellite's orbital motion, resulting in a drift of the right ascension of the ascending node, and the argument of perigee.

The effect of the change in the potential function of the Earth allows for a zonal, geopotential function, with its zonal coefficients,  $J_n$ , which depends on the latitude and longitude, dividing the Earth into a checkerboard pattern. However, as the  $J_2$  coefficient is  $10^3$  times larger than the others, it is possible to model this perturbation using only the  $J_2$  term. The effect of this perturbation on the orbital elements is found by:

$$\begin{aligned}
\dot{\Omega}_{J_2} &= -1.5nJ_2 \left( \frac{R_E}{a} \right)^2 (\cos i)(1-e^2)^{-2} \\
\dot{\omega}_{J_2} &= 0.75nJ_2 \left( \frac{R_E}{a} \right)^2 (4-5\sin^2 i)(1-e^2)^{-2}
\end{aligned}
\tag{4.11}$$

where  $n$  is the mean motion,  $R_E$  is the Earth's radius at the equator,  $a$  is the semi-major axis,  $e$  is the eccentricity,  $i$  is the inclination and  $\dot{\Omega}_{J_2}$  and  $\dot{\omega}_{J_2}$  are the drift rates. This perturbation is dominant in LEO. In fact, it is because of the  $\dot{\Omega}_{J_2}$  that the orbit can be set equivalent to the rate at which the Earth revolves around the sun and thereby making a sun-synchronous orbit.

#### 4.2.3.2 Third-Body Perturbations:

The gravitational forces of the Sun and Moon cause periodic variation in the right ascension of the ascending node (RAAN). This variation results in the precession of the orbit about the ecliptic pole. The precession is much smaller than the mean motion of the orbit, and has little effect on LEO satellites. These perturbations can be found from the equations:

$$\begin{aligned}
\dot{\Omega}_{MOON} &= -0.00338 \cos i / N \\
\dot{\omega}_{MOON} &= -0.00169(4-5\sin^2 i) / N \\
\dot{\Omega}_{SUN} &= -0.00154 \cos i / N \\
\dot{\omega}_{SUN} &= 0.00077(4-5\sin^2 i) / N
\end{aligned}
\tag{4.12}$$

where  $N$  is the number of revolutions per day.

#### 4.2.3.3 Atmospheric Drag:

This perturbation is much more prevalent in LEO than in GEO operations. The drag will act opposite the velocity vector, removing energy from the orbit and decreasing the altitude of the orbit. For a circular orbit, the effects of drag can be modeled as:



$$\begin{aligned}
\Delta a_{rev} &= -2\pi(C_D A/m)\rho a^2 \\
\Delta P_{rev} &= -6\lambda\pi^2(C_D A/m)\rho a^2/V \\
\Delta V_{rev} &= \pi(C_D A/m)\rho aV \\
\Delta e_{rev} &= 0
\end{aligned}
\tag{4.13}$$

where  $r$  is the atmospheric density,  $C_D$  is the coefficient of drag,  $A$  is the satellites cross-sectional area,  $m$  is the satellite's mass,  $V$  is the satellite's velocity and  $a$  is the semi-major axis. As the satellites have been designed to have the same cross-sectional area, and it can be assumed that they are affected by the same atmospheric density due to the nearly identical orbits, the effects of this perturbation on the relative motion of the satellites is negligible.

#### 4.2.4 Constellation Optimization with Perturbations:

With the basic Keplerian equations of motion, the optimal constellation for the satellite would be two orbits, one inclined  $0.5^\circ$  relative to the other. However, due to the introduction of perturbations, specifically the  $J_2$  perturbation, the relative orientation of the two orbits is not constant. The  $J_2$  perturbation causes a drift in the RAAN. This drift is characterized by Equation 4.11, which is dependent upon the semi-major axis, the inclination and the eccentricity. Due to the difference in the inclinations of the two orbits, the drift of the satellite differs by approximately  $0.067^\circ/\text{day}$ , causing an increasing distance between the satellites. Figure 4.16 represents the nodal drift of the constellation and Figure 4.14 shows the relative position of the two satellites propagated forward in time using the Satellite Tool-Kit (STK) High precision orbit propagator (HPOP) over a 15 day period. This propagator includes is a simulation tool, used to propagate orbits in time including the perturbations of drag, the effects of the sun and the moon,  $J_2$  effect, and can include a varying solar radiation perturbation.

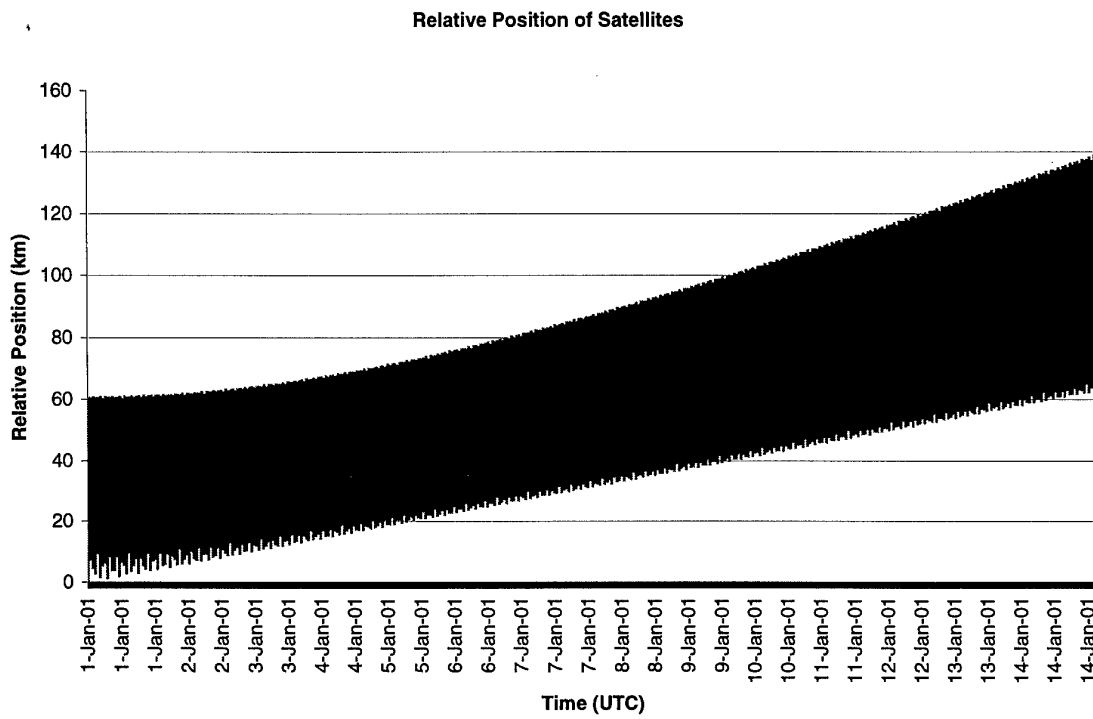


Figure 4.14 Relative Position of the Satellites Propagated over 15 Days

By virtue of the increasing position, the relative velocity changes as well, according to Figure 4.15.

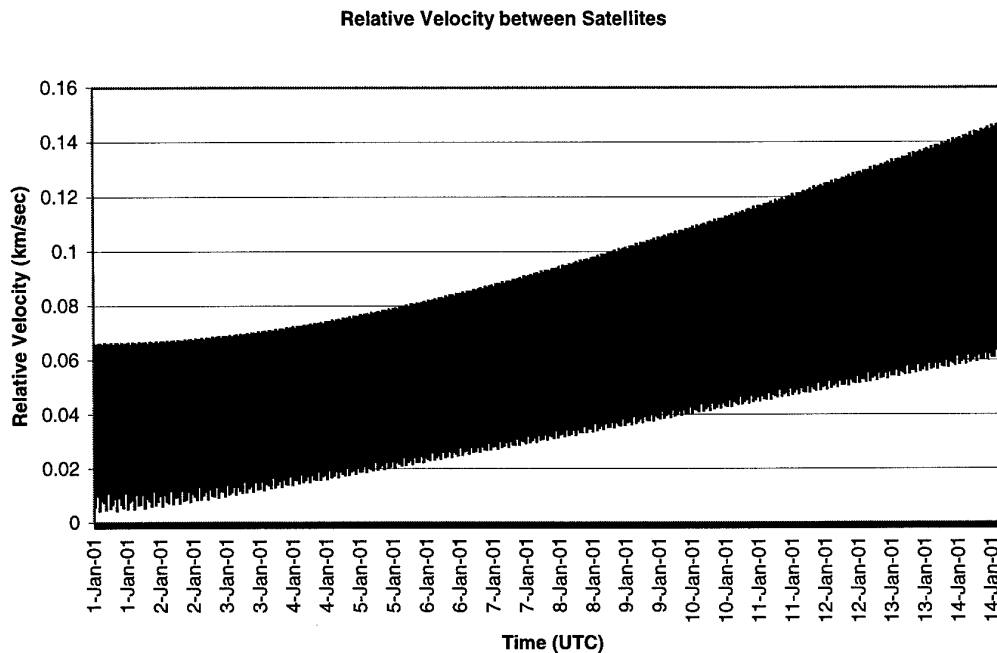


Figure 4.15 Relative Velocity Propagated over 15 Days

This nodal drift will need to be corrected after every 15 orbits, approximately once a day, with a  $\Delta V$  of 5.4 m/s. Figure 4.16 shows the nodal drift of the satellites during the propagation period. This amount of  $\Delta V$  is too high for the satellite, whose entire budget is around 30-40 m/s. This constellation is not possible to maintain.

To correct for this drift, it is necessary to compensate using the eccentricity or the semi-major axis. However, due to the nature of the perturbation, it is necessary to change the semi-major axis by almost 5000 km in order to compensate. The constellation would then no longer be feasible, as the transmitted power would increase above the capacity of the satellite. Therefore, the constellation design is not feasible.

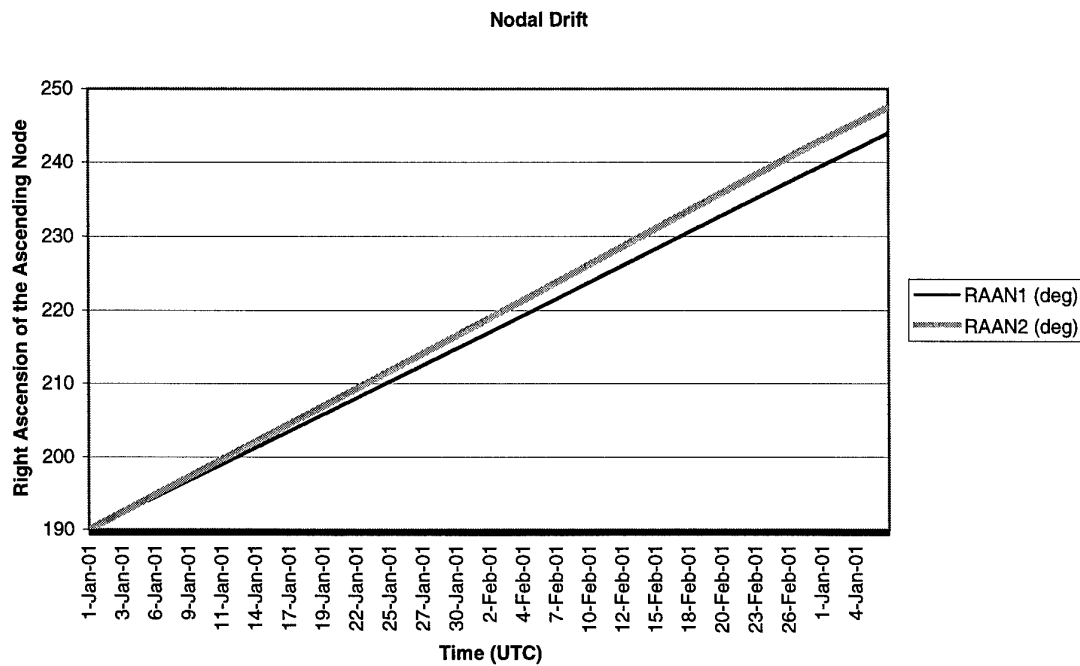


Figure 4.16 Nodal Drift of Initial Formation

However, if the satellites were to have the same inclination, and be separated by a  $3.5^\circ$  RAAN difference, the separation between satellites at the poles would be 60 km, and the relative drift between the satellites would be zero. Figure 4.17 shows the RAAN drift of this design.

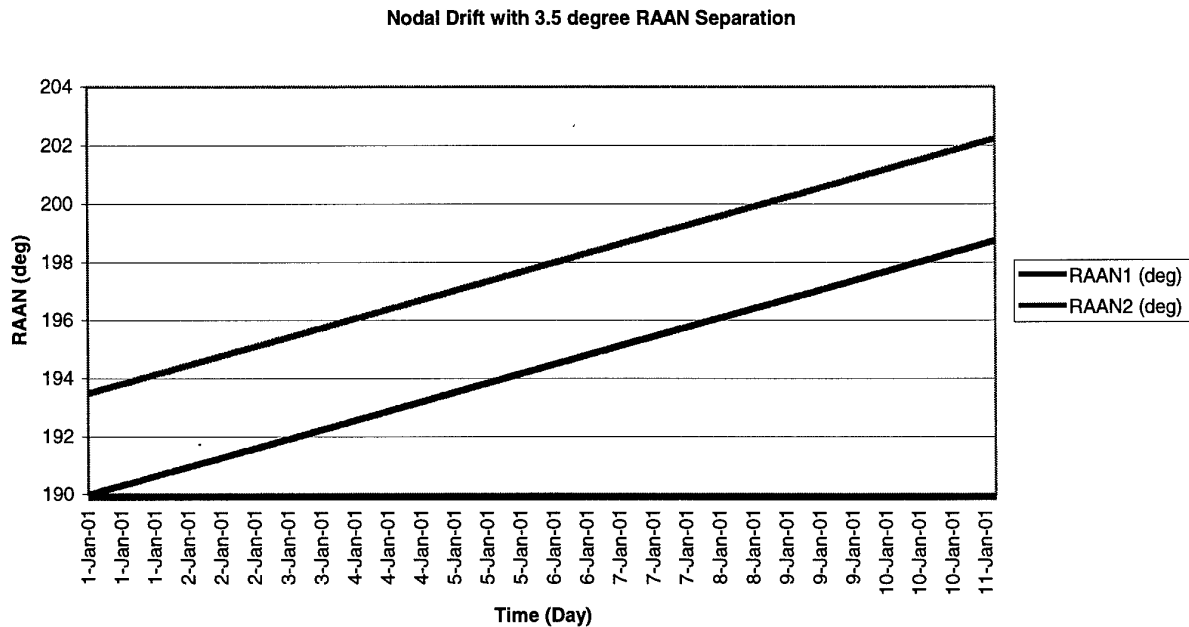


Figure 4.17 Nodal Drift with 3.5° RAAN Separation

While this constellation design reduces the  $\Delta V$  requirement of formation control to simply that required for the station keeping to achieve the two orbital planes., it also requires the launch of the satellites from two separate launch vehicles, to achieve the two orbital planes. This would greatly increase the cost of the mission, and it would be difficult to ensure that each satellite is released in the orbit needed for the constellation.

Therefore, the satellites will be launched from the same vehicle, and the transmitting satellite will change its inclination. This configuration will be allowed to propagate forward in time until the nodal drift has caused the required difference in RAAN so that the satellites are separated by 60 km at imaging. At this time, the receiving spacecraft will perform an inclination change, to match the inclination of the transmitting satellite. The final inclination will be appropriate for a sun-synchronous orbit at 700 km: 98.2°. Therefore, the two orbits will have the same orbital elements, leading to the same nodal drift, and still be separated by 60 km at the time of imaging. Given the initial conditions of an inclination change of 0.5° and a 3.5° RAAN separation, the nodal drift of this

constellation is shown in Figure 4.18. Figures 4.19 and 4.20 show the relative position and velocity, respectively, of the spacecraft after the correction.

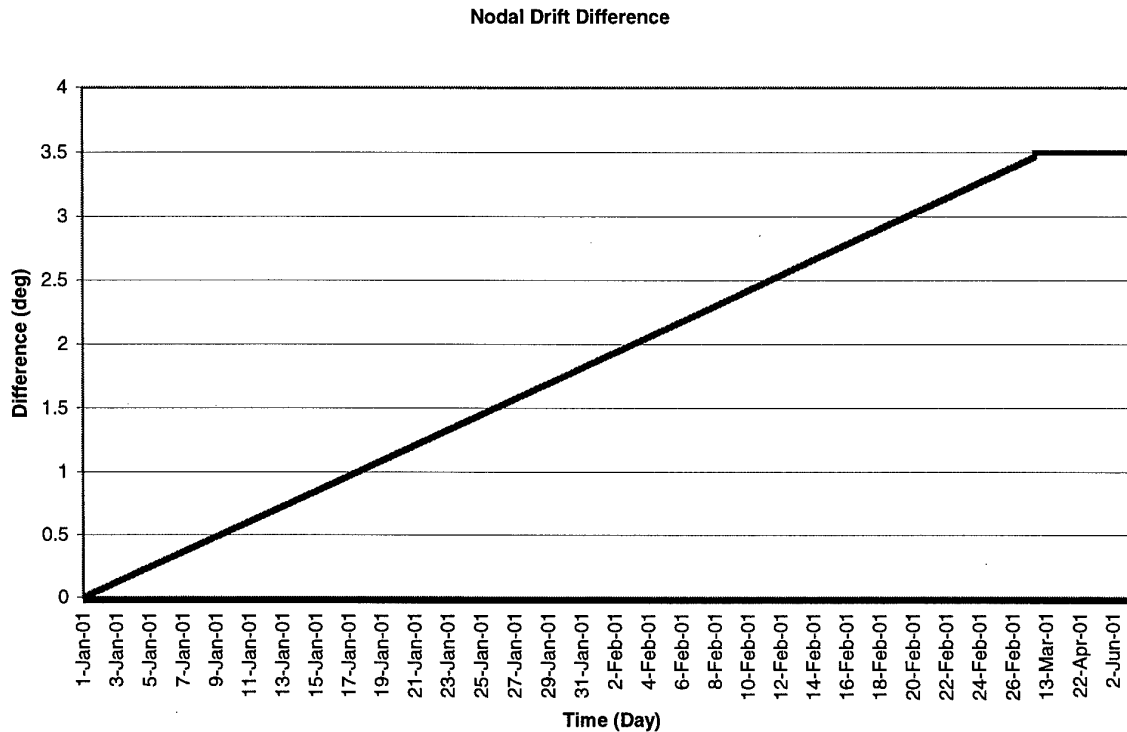


Figure 4.18 Nodal Drift for Revised Constellation Design

It can be seen from this, that the correct orbital configuration, of a  $3.5^\circ$  RAAN separation, will be achieved in 54 days, after the initial plane change manoeuvre. Changing the value of the RAAN separation will change the required change in inclination or the time it takes to achieve the correct orbital configuration.

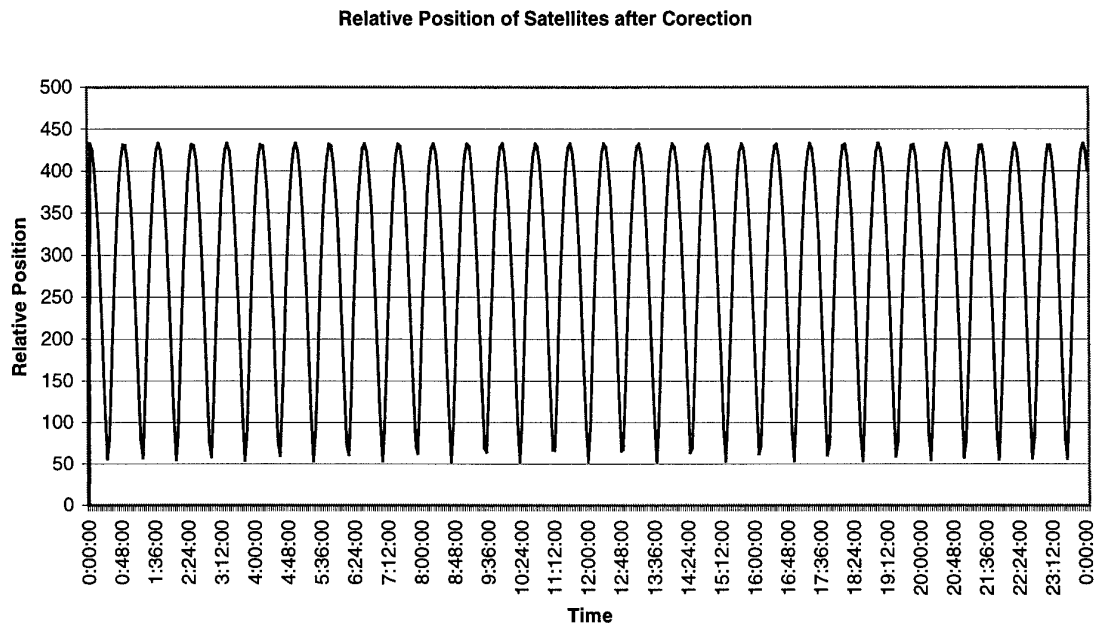


Figure 4.19 Relative Position of Satellites after Correction

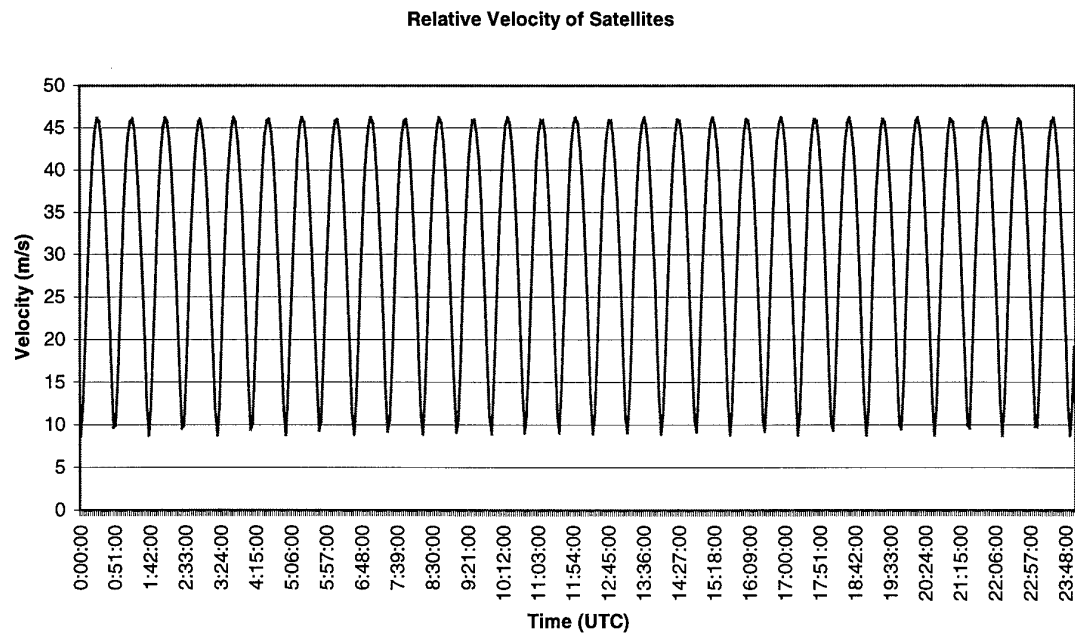


Figure 4.20 Relative Velocity of Satellites after Correction

A problem introduced by this design is the relatively high relative velocity between the two satellites, approximately 47 m/s during the imaging time. This can be compensated by subtracting the Doppler shift in frequency caused by this relative velocity. This is possible due to the relatively small change in velocity over the entire imaging time: 0.00847 m/s. Despite this addition to the processing of the system, this constellation design will allow for the satellites to remain within the needed parameters without excessive station keeping.

The  $\Delta V$  of each satellite will be limited to the normal station keeping of satellites in orbit, which can be approximated by 0.209 m/s per year [LARSc-89]. This velocity requirement is added to the  $\Delta V$  needed for the inclination change of 65.3 m/s. The total requirement for the system is then 66.4 m/s over a 5-year lifetime.

This initial orbit design is for a system that images at the highest latitude possible for the sun-synchronous orbit: 83°. However, the orbit design can be changed to match the desired imaging latitude based upon mission specifications, as the Polar Regions extend from approximately 65° to 90° latitude. As the desired imaging latitude decreases, the RAAN difference, and thus the  $\Delta V$ , needed to position the satellites also decreases. Figure 4.21 illustrates the differing latitude with RAAN separation.



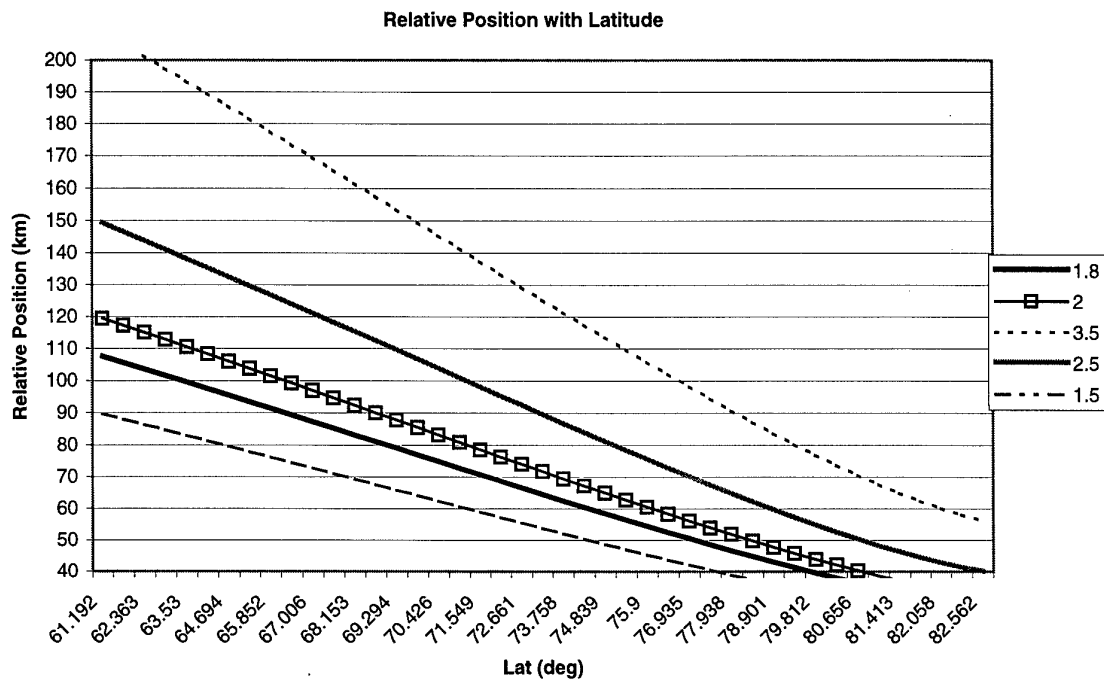


Figure 4.21 Imaging Latitude based on RAAN Differences (in degrees)

For the desired application of the system, i.e. imaging of the polar regions for the commercial and scientific applications, the optimum latitude is approximately  $72^\circ$ , which images the northern parts of Europe, Asia and North America, and the edge the polar ice sheet growth in winter. This requires an RAAN difference of  $1.8^\circ$ , and, consequently, an initial inclination change of  $0.25^\circ$ . The  $\Delta V$  budget is therefore 35 m/s for a 10-year lifetime—32.8 m/s for the plane change and 2.1 m/s for station keeping.

### 4.3 Position Sensors and Error Requirements:

#### 4.3.1 Position and Velocity Errors:

When discussing the position and velocity errors of the radar platform, the errors are in effect, the ephemeris errors of the satellite's guidance and navigation system. The errors

can, for the application to radar, be broken into the along-track, cross-track and radial errors.

The along-track position error, also known as the tangential position error with reference to the satellite's orbital plane, causes a location error in the azimuth direction, only, as the range error is negligible [CURLd-91]. The error follows the equation:

$$\Delta x_{ax} = \Delta R_x \frac{R_t}{R_s} \quad [4.14]$$

where  $\Delta x_{ax}$  is the azimuth error for the image,  $R_t$  is the target location with respect to the center of the earth, which is equal to the earth's radius for this application,  $R_s$  is the sensor position, the radius of the satellite's orbit, and  $\Delta R_x$  is the error in the tangential direction. If this error is assumed to be the position accuracy knowledge of the satellite,  $\pm 15$  m for the GPS navigation system, the total azimuth position error is:

$$\Delta x_{ax} = 15 \cdot \left( \frac{6378}{7078} \right) = 13.5m \quad [4.15]$$

or almost half of the azimuth resolution cell.

With multiple measurements from the navigation system on-board the satellite, the position error can be reduced, due to the constrained nature of satellite orbital motion. The final azimuth error in the image will be 90% of the total error of the navigation system.

In a bi-static system, however, the total along-track position error is the combination of the transmitter and receiver position error. This would make a total error of 30m, for the worst-case scenario, or a 27 m azimuth error. It is therefore apparent that imaging cannot take place until the error is reduced or differential GPS is used for the position finding or a more accurate distance measuring system is used.

The cross-track error is determined by the same method as the along-track, however, it causes a location error in the range direction instead of the azimuth direction [CURLd-91]. The error equation is therefore:

$$\Delta x_{ry} = \Delta R_y \frac{R_t}{R_s} \quad [4.16]$$

where  $\Delta x_{ry}$  is the range location error, and  $\Delta R_y$  is the cross-track position error. The same constraints, which concern the azimuth location error, are identical for the range error.

The radial error of the sensor, or the error in the sensor height, causes error in both the range and azimuth directions due to the change in the look angle. The look angle change can be determined by the equation:

$$\Delta \gamma = \cos^{-1} \left[ \frac{R^2 + R_s^2 - R_t^2}{2RR_s} \right] - \cos^{-1} \left[ \frac{R^2 + (R_s + \Delta R_z)^2 - R_t^2}{2R(R_s + \Delta R_z)} \right] \quad [4.17]$$

where  $\Delta \gamma$  is the change in the look angle,  $R$  is the slant range, and  $\Delta R_z$  is the radial error [CURLd-91]. This change in the look angle results in range and azimuth errors according to the following equations:

$$\begin{aligned} \Delta r_r &= R \Delta \gamma / \sin \theta \\ \Delta r_a &= V_E (V_{swT} + V_{swR}) R / (V_{Tt} + V_{Rt})^2 (\cos \zeta \sin i \cos \gamma) \Delta \gamma \end{aligned} \quad [4.18]$$

where  $V_E$  is the Earth's velocity at the equator,  $V_{sw}$  is the swath width velocity,  $V_{st}$  is the velocity of the sensor with respect to the target, T and R subscripts are for the transmitter and receiver, respectively,  $R$  is the slant range,  $z$  is the latitude, and  $i$  is the orbit inclination [CURLd-91]. The  $V_{sw}$  is defined by the velocity of the sensor minus the velocity of the target.

Errors in the satellite's velocity determination lead to azimuth location errors only, as it changes the Doppler shift of the echoed response. Again, the total velocity error of the system is the sum of the velocity errors of the transmitting and receiving satellites. For an error of 10% of the total filter bandwidth, 120 Hz, the acceptable total velocity error is 1.5 m/s. Given this figure, the errors produced by the uncertainty in the velocity measurements are negligible.

### 4.3.2 Attitude Errors:

The variation of the pre-determined roll, pitch and yaw of the satellite will cause errors in the antenna beam pointing and therefore, errors in the final image. The errors caused by each of these motions will be analyzed with respect to the system design.

The effects of small roll errors, within half a degree, are negligible to the image [ELACb-87]. In the system design, the total swath width in the range and azimuth directions is 35 x 35km. However, an image of dimensions 30x30km is used for the system, allowing for a small pointing error of 0.5°. The roll accuracy knowledge of the spacecraft is 0.25° with a control ability of 0.2°, which are both within the error limit. Therefore, the roll error remains within the limit of the system.

The effects of the pitch and yaw errors cause a distortion in the Doppler frequency shift. As the pitch and yaw rates contribute negligibly to the Doppler shift, they will not be analyzed in this discussion [ELACb-88].

An error in the yaw knowledge of the system, causes a displacement of the antenna beam footprint around the non-zero Doppler line—causes a squint angle. This adds a Doppler shift of:

$$\Delta f_y = \frac{(V_T + V_R)}{\lambda} \sin \theta \sin \epsilon_y \quad [4.19]$$

where  $\theta$  is the incidence angle, and  $\epsilon_y$  is the yaw error.

The ADCS for the satellite provides a yaw accuracy of 0.5°. This leads to a yaw error of 97 Hz. This error is contained within one resolution cell.

This error can be corrected by adding an error frequency to the echoed response or in the processor through auto-focusing [ELACb-88].

The pitch error has a similar effect on the image, as it displaces the footprint either forwards or behind the zero-Doppler line in the cross-track direction. This error is found by:

$$\Delta f_p = \frac{(V_T + V_R)}{\lambda} \sin \epsilon_p \quad [4.20]$$

where  $\epsilon_p$  is the pitch error.

The attitude accuracy of the satellite with respect to the pitch is  $0.4^\circ$ , this leads to an error of 350 Hz. This is greater than an azimuth resolution cell and will create a significant error to the image. Therefore, it will be necessary to determine the pitch error more accurately, or use the signal processing to correct for this error. The yaw and pitch errors can be combined, and both compensated for at during processing.

To correct the attitude errors through processing methods, therefore not requiring the furtherance of technology, the method is iterative, but simple. As the known error can be translated directly to a Doppler shift frequency, this frequency can be added to the range compressed data, i.e. before azimuth processing, to remove these errors from the image. If this process is going to be done outside of the auto-focus algorithm, which will also correct for these errors, it should be done prior to auto-focusing to allow for less iterations of the auto-focusing algorithm.

It is possible to use GPS to gain an accurate knowledge of the motion of each satellite. If the GPS navigation system is used before, during and after the image, an accurate orbit can be determined due to the constrained motion of the orbit. This knowledge would then be used to correct for these errors in the processing.

### 4.3.3 Orbital Errors:

In space borne SAR, an error is introduced due to the rotation of the Earth with respect to the orbital plane. As the planet rotates around its axis, it introduces a Doppler shift on the magnitude of:

$$\Delta f_R = \frac{2R_E \Omega_E}{\lambda} \sin \theta \cos \gamma \quad [4.21]$$

where  $\theta$  is the incidence angle,  $\gamma$  is the latitude,  $R_E$  is the radius of the Earth, 6378 km, and  $\Omega_E$  is the rotational velocity of the Earth [ELACb-88]. To be more accurate, a correction to Equation 4.21 can be made by subtracting from  $\Omega_E$  the rotation in the inertial frame. However, this movement is small in comparison to  $\Omega_E$ . As the imaging will happen near the poles, the Doppler shift is negligible—approximately 10Hz.

An error will also be introduced as the eccentricity of the orbit, which is nominally set to zero, but this value is unachievable in actual orbits. The eccentricity of the orbit can be achieved within 0.001 [ELACb-88]. In this system, this will cause a change in the range of approximately 14 km and, subsequently, a change in the relative velocity. However, as the orbit is known before the imaging time to high precision using navigation and the ADCS, this error is known and can be processed out of the final image.

The previous discussion gives an initial analysis of the effects of the motion and attitude errors of the platform. To gain an accurate knowledge of the level of errors, which are acceptable to the system, it is necessary to model the SAR data with errors, process it through the system including auto-focusing. This will determine the quality of the image given different levels of errors.

## ***4.4 Slot Allocation and Power Flux Restrictions:***

### **4.4.1 Signal Allocation**

Due to the congested nature of the radio frequency bands for communication, research and radiolocation in both earth-bound, airborne and space borne applications, the International Telecommunications Union creates allocation guidelines [ITU-01]. From 1844, when Samuel Morse sent his first public message over telegraph to modern times, the frequency bands have become increasingly congested. The ITU, which was first

formed in 1865, and later became under the regulation of the United Nations in 1947, is responsible for the regulation of the telecommunications industry. Part of this control involves the International Frequency Registration Board, responsible for managing the increasing complex frequency spectrum through the Table of Frequency Allocation. This table allocates to each service using radio waves specific frequency bands to avoid interference between stations.

The ITU has divided the world into three regions of control: Region 1—Europe, Africa, and the Middle East, Region 2—the Americas, and Region 3—Asia, except for the Middle East [ITU-01]. While the Frequency Allocation Table allows for specific bands to be allocated to specific services, each region is allowed to present regulations on those services to ensure non-interference between signals. Due to the nature of the project, with the transmission period over the poles, the regulatory requirements of each region must be met.

Given these regulatory statutes, it is necessary to determine the availability within the chosen S-band frequency, which will allow for the operation of the SAR system. The frequency band of 2290-2300 MHz is allocated for space-to-Earth Space research. The band of 2390-2483.5 MHz is allocated as amateur bands with an emphasis placed on industry, scientific and medical purposes. Frequency use in each of these bands is possible for this project.

#### **4.4.2 Power Flux Regulation:**

Having determined the availability of the desired frequency band for use for the project, the power flux of the signal at ground level must also be determined. Figure 4.22 shows a representation of the allowable power flux densities for all S-band usage.

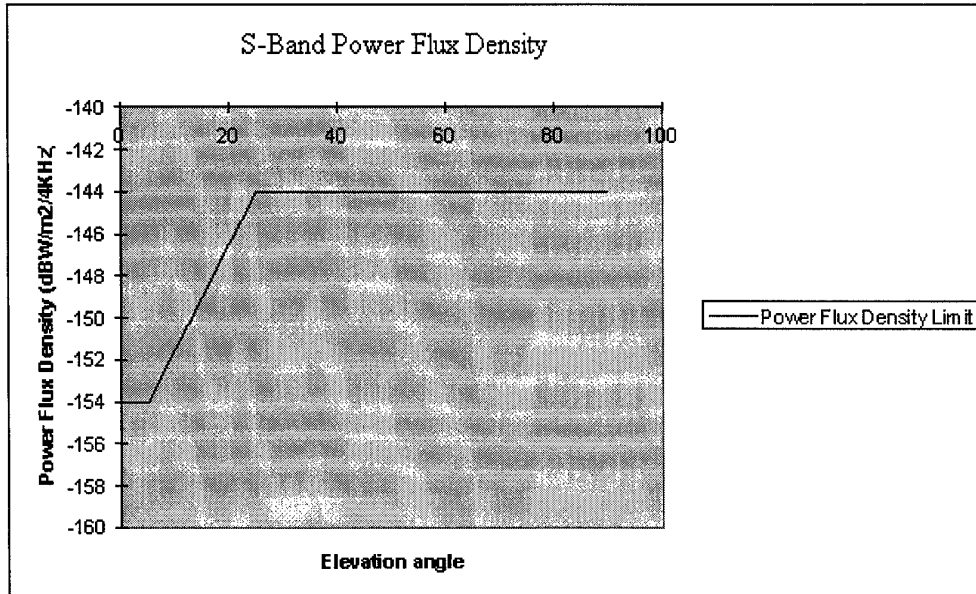


Figure 4.22 Power Flux Density at S-band [MARA-86]

Therefore, the maximum power flux density possible for transmission is  $-144 \text{ dBW/m}^2$  per 4 kHz bandwidth. Given the transmitted signal is at a distance of 700 km and the peak transmitted power is 624 W with multiple look integration, the power flux density over the 100 MHz bandwidth is  $-100 \text{ dBW/m}^2$ . Correcting to a 4 kHz bandwidth, the power flux density of the signal per 4 kHz bandwidth of the transmitted signal is  $-144 \text{ dBW/m}^2/4\text{kHz}$ , operating at an elevation of  $60^\circ$  to  $83^\circ$  in elevation. This value is within the prescribed limit. The system, therefore, operates within an appropriate frequency band and has a power flux density within the required limit. The power output cannot exceed this level as the power flux density at the ground will be above the limit.



## **Chapter 5 Conclusions and Future Work**

### **5.1 Conclusions**

The study shows the feasibility of placing a Synthetic Aperture Radar system on-board a constellation of micro-satellites. This is an important development in satellite technology, as it would reduce the cost and development time for SAR system and allow for wider use in commercial and scientific applications.

The system geometry consists of a transmitting and a receiving satellite in a bi-static configuration, allowing for the reception of the forward-scatter to reduce the required transmit power. The satellites will be placed in two identical orbits, separated by an RAAN difference of  $1.8^\circ$ , i.e. a separation of 60 km at  $72^\circ$  latitude. At the time of imaging, the antenna of the transmitter will point at an angle of  $3.7^\circ$  from vertical, approximately 45km cross-track from the transmitter. This requires the receiver antenna to point at  $1.2^\circ$  from vertical for the beam centres to match. The receiving satellite will be slaved to the transmitter, which, when used in conjunction with the GPS navigation system, will allow for synchronization of the distributed SAR system in time, phase and signal.

The two satellites are based on the SSTL enhanced micro-satellite design, which is a truncated pyramid with a 1x1m base and 0.6 m height. The truncated pyramid shape is used to allow for a maximum power production by the satellite's solar panels in a sun-synchronous orbit. It has a total mass of 100 kg with 40 kg being allocated to the payload. The satellite has been designed with a modular structure to allow for fast, easy conversion to meet payload requirements or adapt due to changes in the state-of-the-art.

The power system consists of body-mounted Gallium Arsenide (GaAs) solar cells, producing 100 W individually, for a total production of 140 W. The standard Nickel

Cadmium battery pack allows for 200 Wh of power to be stored. This system has a total available peak power drain of 1 kW.

The satellite is 3-axis stabilized, using multiple sun and horizon sensors, with a control accuracy of  $0.25^\circ$  on the roll axis,  $0.5^\circ$  on the yaw axis and  $0.4^\circ$  on the pitch axis. This attitude control is not quite accurate enough for SAR imaging, but the estimated errors can be removed from the SAR data through processing or auto-focusing. The position knowledge for the satellite is provided by a standard SSTL GPS receiver for small satellites, which provides position knowledge of  $\pm 15$  m. This position accuracy can be increased using Differential GPS and pulse ranging.

The on-board SAR system consists of a transmitter and receiver, distributed on two different satellites. The transmitter must be compact to fit on the micro-satellite, smaller than  $1 \times 1 \times 0.3$  m, and transmit at a centre frequency of 2.4 GHz with a bandwidth of 100 MHz, allowing for a 10 ns compressed pulse length. The transmitter will emit a chirped pulse of 34  $\mu$ s duration at a PRF of 6 kHz, making 24,000 pulses per image (each image requires 4s of flight time). The total DC power of the transmitter must be 100 W, approximately an RF power of 25 W. This power output will allow for the detection of a target with a  $-15$  dB RCS, the estimated lowest RCS encountered when imaging sea ice. The transmitter must also maintain a high level of stability to ensure coherence between the pulses. The stalo must have a drift of less than  $2.5 \times 10^{-10}$  over 4 s within a phase error of  $1^\circ$ . The on-board clock must not drift more than 2 parts per  $10^9$  over the 4 s imaging time.

The receiver subsystem is characterized by the same stability requirements as the transmitter, since the system, though distributed on two satellites, must work together coherently. The receiver must be sufficiently low-noise, as all added noise will degrade the system, causing false responses and masking of actual echoes. While limiting the noise in the system, the receiver must also have a bandwidth of at least 101 MHz, comprising the transmitted bandwidth and the Doppler shift. This wide bandwidth will allow for a high level of external noise to be detected along with the echoed responses,

but any limiting of the value will cause some echoes to remain undetected. The minimum detectable signal of the receiver is  $8.225 \times 10^{-10}$  W, given a probability of detection of 99.6%.

The receiving satellite will also provide for the compression and storage of the returned echoes. The system must be able to down-convert, sample and store the incoming data at 200 MSps on both the I and Q channels. This will require a 4 Gbit temporary memory for the sampled pulses. This data is then compressed by a factor of 4 using a standard BAQ compression algorithm. The final compressed data is 850 Mbits per image. This is small enough to be sent to the ground station with the standard communication downlink of 2 Mbps over the 10 minutes. This will require the downlink antenna to have a beam width of at least  $129^\circ$ .

The antenna used for the SAR system is a 2.5 m diameter parabolic dish antenna with a cavity backed, crossed-dipole feed system providing horizontal, vertical and right-handed or left-handed circular polarization for "multi-spectral" imaging of the ice. This will achieve a 35 x 35 km footprint and a gain of 30 dB at 30% efficiency. Due to the large size of the antenna compared to the satellite dimensions, the antenna is stowed for launch in a "petaled" configuration, to be deployed once the satellite is in orbit. The power of the multiple polarizations, though complex to implement, will allow for the imaging of the ice structures at various levels. Using similar linear polarizations or reverse circular polarizations, the imaging will provide data on the surface scattering of the ice to provide detailed images. This data is useful for the general study of the ice structure and the extent of coverage. However, if reverse linear polarizations or similar circular polarisations are used for the transmitting and receiving satellites, the returned echo will show the cross-polarization element of the scatter, which will provide data on volumetric scattering of the ice and study the ice thickness. The thickness of the ice will provide a detailed description of the ice.

One of the most important features of the space borne components of the SAR system is the synchronization, in time, phase and signal, of the transmitting and receiving

subsystems. Synchronization of time is accomplished by using the GPS receiver to update the on-board clocks. To further remove the errors of the GPS signal due to the differing propagation time, the receiver will use GPS and the pulses from the transmitter to determine the differences in the GPS baseline and the receiver computed baseline, allowing the removal of this error. The synchronization of the signal will be accomplished through DDS, in which a digital copy of the waveform replaces the exciter, providing a copy of the waveform for the transmitter, receiver and ground station. Finally, the phase synchronization will be accomplished through stalos with a combined drift of  $2.3 \times 10^{-11}$  for the imaging time.

As no on-board processing is done, the ground station becomes an integral part of the SAR system. To complete the synchronization of the signal for all subsystems which require an accurate copy of the transmitted pulse, the ground station will be supplied with the same DDS memory as that which in on-board the satellites, and it can use updated error measurements from the transmitter to correct for errors. The ground station will receive the compressed data from the receiving satellite, requiring memory write-able at 2 MHz. The ground station will then decompress the data and accomplish SAR processing to produce an image. As there is no system time requirements on the processing done in the ground station, there are no constraints on processing speed and the ability to use auto-focusing to reduce the effects of higher order phase errors in the image.

Having designed and determined the feasibility of the SAR system and the platform, the final area of study is the formation and orbit design, to show that the satellite will be able to remain in formation with the propulsion system constraints. The basic orbits for the satellites are sun-synchronous, with an inclination of approximately  $98^\circ$ , at an altitude of 700 km, a period of 98.8 minutes, and an RAAN separation of  $1.8^\circ$ . With this RAAN difference, the satellites will image at approximately  $72^\circ$  latitude, corresponding to the northern coasts of Europe, Asia and North America. This formation will need a  $\Delta V$  budget of 35 m/s for a 10-year lifetime—32.8 m/s dedicated to the formation construction and 2.2 m/s for lifetime station keeping.

Due to the theoretical nature of the study, the system was designed with very conservative assumptions as to the efficiency of the components and the scattered power from the scene. This was done to produce a system that was detailed and complete, yet was not overly dependent upon the assumptions made. Therefore, if the component was more constrictive on the constraint, the system would not be rendered inoperable.

The feasibility of placing the designed SAR system on a micro-satellite platform is shown through this research. However, this study provides only one design of a SAR system dedicated to one area of imaging. It is not an exhaustive study as to the extent to which this system can be applied to other areas on the Earth. In addition, as this study was based on theoretical objectives, there was no component testing to show if the practical system will comply with the theoretical results.

## **5.2 Future Work**

The scope of this study was to determine the feasibility of a SAR system on the SSTL enhanced micro-satellite. Being a theoretical study only, there was no construction or component testing done to any aspect of the system, leaving the testing for future work.

### **5.2.1 Sea Ice Scattering**

Further study into the properties of sea ice scattering is recommended. The values presented in this study were gained from the extrapolation of the values of vertical scattering from different ice type and structures. This seems a valid assumption as the system works at a total of  $4^\circ$  off the vertical, which can be considered vertical, and the study was conducted to gain only an estimate of the RCS and the radar contrast of the ice. While adequate for providing an estimate of the strength of the return echo and the energy received, a detailed study, in which the forward-scatter from various types of sea ice at S-band frequency is necessary for accurate classification of the type and depth of

ice. Also, testing of the ice using different polarization will allow for the optimisation of the system so the maximum return is collected by the system. Therefore, the returns in the system can be accurately classified and used for both the commercial and scientific applications. It would be possible to conduct this study in the actual environment (from a boat or aircraft) or in a simulated environment in a laboratory.

In conducting this research into accurate sea ice properties, it will be possible to also gain an accurate figure for the power requirements. As this is based directly on the RCS, the more accurately the RCS is known, the more accurate the power requirement can be determined. It will be useful construct a similar system for the testing of the properties of ice, the results can be used to gain accurate information on the transmit power needed. Finally, by testing the echoes of ice, it will be possible to gain a better understanding and expand the uses of the multiple polarization aspect of the system.

Other than the testing of sea ice characteristics, it is not necessary to conduct any further studies on the construction of the transmitter and receiver satellite platforms, as these spacecraft are not specific to the radar system and are currently available as commercial-off-the-shelf items. However, before the system is actually flown, further work will need to be conducted so that the attitude stability of the two platforms, and their combined characteristics can be determined before flight. This would be similar to any flight-testing done on a system before it is flown in space.

### **5.2.2 Antenna**

Due to the unique nature of the deployment scheme for the antenna and the aberrations that are caused by this scheme, it will be necessary to conduct a further study on the effects of these errors on the characteristics of the antenna. A model of the antenna will need to be constructed using the reflector geometry and the feed system presented in the study. First, the locking mechanisms used during launch will need to be tested to validate their ability to withstand the forces of launch. This is necessary to ensure the stability during launch. After this has been validated, the deployment scheme of the antenna will

need to be tested to ensure the panels fit closely together and are locked into place on deployment. Most importantly, an adequate antenna pattern and gain value will need to be gathered from testing. This will test the efficiency of the reflector-feed system, any losses caused by the feed lines, and the losses in gain due to the aberrations. Also, an accurate model of the antenna pattern will be found, and any edge tapering or corrections to the feed pattern can be determined. As these factors can help to increase the efficiency and gain of the antenna, it is important to minimize these losses to maintain system integrity.

### **5.2.3 Data Handling and SAR Processing**

The algorithms used in this system are all well known and have been previously used. However, a further study into the data handling and SAR processing using all algorithms suggested (data compression and decompression, processing, error correction and auto-focusing) will allow for the system performance to be determined. A sample of raw SAR data, or simulated data, can be gathered to give accurate echo characteristics. The compression and decompression algorithms will then process this data. As the compression is lossy, there will be an inherent degradation in the raw data quality before this process, which can be determined with a simulation. Passing this data through the processing algorithm, including auto-focusing and error correction, will then produce an accurate representation of the images, which can be formed from the system.

### **5.2.4 Synchronization**

The final aspect of the SAR system, which will require further work, is the synchronization methods between the transmitter and the receiver. The feasibility study outlined the requirements for the synchronization and basic methods for synchronization. However, no exact values of the likely errors that will be encountered were offered.

Using two GPS receivers, the transmitter and the receiver can test the time synchronization between the two satellites. The GPS can be used to find the position of

the transmitter and receiver as would happen in operation. The transmitter will transmit a pulse, which the receiver will use to determine the baseline and its clock error. The average baseline and the clock errors can be measured over successive testing iterations. Differential GPS should be investigated to get errors down to the centimetre range.

### **5.2.5 Satellite Design**

While the structure and size of the enhanced micro-satellite is fixed, there is the possibility for further work to improve the platform for the SAR system. The feasibility study mainly used the standard components of the enhanced micro-satellite, however, a more detailed study into possible components compatible with the size, volume and power constraints inherent to micro-satellites, might provide a more SAR “friendly” platform. An additional battery pack or further solar panel, for example, may be added to the satellite to allow for a higher power production and a relaxing of the constraints on the SAR system. Also, more accurate attitude sensors or actuators may be used to decrease the errors in the image caused by attitude errors. As this is one of the main sources of errors that will degrade the image, the additional costs for better components may be worthwhile. Finally, the propulsion system or the attitude actuators on-board the satellite may be revisited to provide more agility and manoeuvrability, allowing for further imaging opportunities and areas. This additional design process would be standard practice before any construction of an actual flight system would take place and allows for design updates with increases in technology.

### **5.2.6 System Applicability**

This system was designed with the specific application to sea ice. However, the design of the system is limited to this region only, but could be expanded or revised to apply to many different areas. For example, if the area of interest for the system was an urban environment or city imaging, it might be possible to use only one satellite, given that the mass and volume of each component will meet the micro-satellite constraints, or to increase the resolution due to the high backscatter from this region. City environments are known to have a minimum backscatter of approximately -10 dB, and the possibility



exists to use a single satellite system. Also, given the direct relationship between power and resolution, the resolution can then be improved if the returned power is greater. Conversely, if the system were to be applied to a region with significantly less forward-scatter, e.g. woodlands, the resolution constraint of 30 m can be relaxed to compensate for the reduced power return. Investigating other regions of application will expand the usefulness of this system.

## References:

- [ADAM-87] Adams, J.W. and T.M. Schifani. *Waveform Error Analysis for Bistatic Synthetic Aperture Radar*. IEE International Conference on Radar. 1987.
- [ALGR-00] Algra, Theo. *Compression of Raw SAR Data using Entropy-Constrained Quantization*. IEEE International Geoscience and Remote Sensing Symposium. 2000.
- [AUTE-84] Auterman, James L. *Phase Stability Requirements for a Bistatic SAR*. IEEE National Radar Conference. 1984. pg. 48-52.
- [BALA-82] Balanis, Constantine. *Antenna Theory: Analysis and Design*. John Wiley & Sons, New York. 1982. pg. 785-830.
- [BARB-85] Barber, B.C. *Theory of Digital Imaging from Orbital Synthetic-Aperture Radar*. International Journal of Remote Sensing, Vol. 6, No. 7. 1985. pg.1008-1057.
- [BARB-98] Barber, David, Adrian Fung, Thomas Grenfell, Son Nghiem, Robert Onstott, VI Lytle, Donald Perovich and Anthony Gow. *The Role of Snow on Microwave Emission and Scattering over First-Year Sea Ice*. IEEE Transactions on Geoscience and Remote Sensing, Vol. 36, No.5. Sept 1998. pg. 1750-1763.
- [BECKa-87] Beckmann, Petr and Andre Spizzichino. *The Scattering of Electromagnetic Waves from Rough Surfaces*. Artech House, Inc., Maine. 1987. pg. 9-33.
- [BECKb-87] Beckmann, Petr and Andre Spizzichino. *The Scattering of Electromagnetic Waves from Rough Surfaces*. Artech House, Inc., Maine. 1987. pg. 70-98.
- [BENZ-95] Benz, Ursula, Klaus Strodl, and Alberto Moreira. *A Comparison of Several Algorithms for SAR Raw Data Compression*. IEEE Transactions on Geoscience and Remote Sensing, Vol. 33, No. 5. Sept 1995. pg. 1266-1276.
- [BLAK-66] Blake, Lamont V. *Antennas*. John Wiley & Sons, Inc., New York. 1966. pg. 256-283.
- [BOVE-87] Bovey, C.K. and C.P. Horne. *Synchronization Aspects for Bistatic Radar*. IEE International Conference on Radar. 1987.
- [BROW-73] Brown, William and George Houser. *Synthetic Aperture Processing with Limited Storage and Presumming*. IEEE Transactions on Aerospace and Electronic Systems, Vol. AES-9, No. 2. March 1973. pg. 166-175.
- [BURD-68] Burdick, William S. *Radar System Processing*. Prentice Hall, Inc., New Jersey. 1968.
- [BURE-71] Bures, Kenneth and Ferrel Stremmler. *Synthetic Aperture Bistatic Radar for Mapping Tropospheric Radio Scatterers*. Proceedings IEEE, Vol. 59, No. 4. April 1971.
- [CARS-92] Carsey, Frank D. [ed] *Microwave Remote Sensing of Sea Ice*. Geophysical Monograph Series, Washington DC. 1992. pg.9-47.
- [CHAN-98] Chan, Hiam Lim and Tat Soon Yeo. *Non-iterative Quality Phase-Gradient Autofocus Algorithm for Spotlight SAR Imagery*. IEEE Transactions on Geoscience and Remote Sensing, Vol. 36, No. 5. Sept. 1998.

- [CHEN-99] Chen, Victor and William Miceli. *The Effect of Roll, Pitch and Yaw Motions on ISAR Imaging*. SPIE Conference for Radar Processing, vol. 3810. July 1999.
- [COOK-67] Cook, Charles E. and Marvin Bernfeld. Radar Signals: An Introduction to Theory and Application. Academic Press, New York. 1967. pg. 130-171.
- [COUL-97] Coult, Regina. **Investigation of the Feasibility of Low-Cost Small Satellite SAR in Present Constraints**. Centre for Satellite Engineering Research. Sept, 1997.
- [CURLa-91] Curlander, John and Robert McDonough. Synthetic Aperture Radar Systems and Signal Processing. John Wiley & Sons, Inc., New York. 1991. pg. 126-152.
- [CURLb-91] Curlander, John and Robert McDonough. Synthetic Aperture Radar Systems and Signal Processing. John Wiley & Sons, Inc., New York. 1991. pg. 182-208.
- [CURLc-91] Curlander, John and Robert McDonough. Synthetic Aperture Radar Systems and Signal Processing. John Wiley & Sons, Inc., New York. 1991. pg. 256-294.
- [CURLd-91] Curlander, John and Robert McDonough. Synthetic Aperture Radar Systems and Signal Processing. John Wiley & Sons, Inc., New York. 1991. pg. 376-379.
- [CURLe-91] Curlander, John and Robert McDonough. Synthetic Aperture Radar Systems and Signal Processing. John Wiley & Sons, Inc., New York. 1991. pg. 428-473.
- [CURR-91] Currie, A. *Synthetic Aperture Radar*. Electronics and Communication Engineering Journal. August 1991. pg. 159-170.
- [CUTR-70] Cutrona, L.J. *Synthetic Aperture Radar*. Ch.23 of The Radar Handbook. Merrill Skolnik, ed McGraw-Hill Book Co., New York. 1970.
- [D'ADD-86] D'Addio, E., and A. Farina. *Overview of Detection Theory in Multistatic Radar*. IEE Proceedings Pt. F, Vol. 133, No. 7. 1986.
- [D'ELI-00] D'Elia, Ciro, Giovanni Poggi and Luisa Verdoliva. *Compression of SAR Raw Data via Range Focusing and Trellis Coded Quantization*. IEEE International Geoscience and Remote Sensing Symposium. 2000.
- [DONG-97] Dong, Y., B. Forster and C. Ticehurst. *Radar Backscatter Analysis for Urban Environments*. International Journal of Remote Sensing, Vol. 18, No. 6. 1997. pg. 1351-1364.
- [EDMO-84] Edmonds, Marty. Digital Algorithms in Spaceborne Synthetic Aperture Radar. AFIT Internal Report. 1984.
- [ELACa-88] Elachi, Charles. Spaceborne Radar Remote Sensing: Applications and Techniques. IEEE Press., New York. 1988. pg. 51-80.
- [ELACb-88] Elachi, Charles. Spaceborne Radar Remote Sensing: Applications and Techniques. IEEE Press., New York. 1988. pg. 85-109.
- [ELACa-87] Elachi, Charles. Introduction to the Physics and Techniques of Remote Sensing. John Wiley & Sons, Inc., New York. 1987. pg. 22-45.
- [ELACb-87] Elachi, Charles. Introduction to the Physics and Techniques of Remote Sensing. John Wiley & Sons, Inc., New York. 1987. pg. 161-218.

- [ENVI-01] EnviSat Homepage: <http://envisat.esa.int>.
- [ERS-01] ERS Homepage: <http://earth.esa.int>.
- [FRAN-99] Franceschetti, Giorgio and Riccardo Lanari. Synthetic Aperture Radar Processing. CRC Press, Florida. 1999. pg. 105-165.
- [GALL-88] Gallaway, William, Kirk Luckscheiter, Eric Cowen, and Joseph Wilhelm. *A Direct Digitally Synthesized Exciter Achieving Near Theoretical Performance for an Operational SAR System*. IEEE National Radar Conference. 1988. pg. 22-27.
- [GLAS-86] Glaser, J.I. *Fifty Years of Bistatic and Multistatic Radar*. IEE Proceedings Pt. F, Vol. 133, No. 7. 1986.
- [GRIF-91] Griffiths, H.D. *The Effect of Phase and Amplitude Errors in FM Radar*. IEE High Time-Bandwidth Waveforms Colloquium. 1991. pg. 9/1-9/5.
- [HANL-80] Hanle, Eberhard. *Distance Considerations for Multistatic Radar*. IEEE International Radar Conference. May 1980. pg. 100-105.
- [HOM-90] Hom, R.L., R.E. Rouse and K.L. Bateman. *An Automatic Phase Alignment System for Transmitters*. IEEE International Radar Conference. 1990. pg. 141-146.
- [HOVA-80] Hovanessian, S.A. Introduction to Synthetic Array and Imaging Radars. Artech House, Inc., Maryland. 1980.
- [HSU-86] Hsu, Y.S., and D.C. Lort. *Spaceborne Bistatic Radar - An Overview*. IEE Proceedings Pt F, Vol. 133, No. 7. 1986.
- [HUAN-97] Huang, J., M. Lou, and E. Caro. *Super-Low-Mass Spaceborne SAR Array Concepts*. IEEE Antennas and Propagation Society International Symposium. 1997. pg. 1288-1291.
- [HUDS-81] Hudson, J.E. Adaptive Array Principles. Peter Peregrinus, Ltd., London. 1981.
- [ITU-01] International Telecommunication Union Website: <http://www.itu.int/aboutitu/history.html>
- [JORD-75] Jordan, Gary Blake. *Comparison of Two Major Classes of Coherent Pulsed Radar Systems*. IEEE Transactions on Aerospace and Electronic Systems, Vol. AES-11, No. 3. May 1975. pg 363-371.
- [JPL-01] JPL Remote Sensing Website: [www.southport.jpl.nasa.gov/desc/imagingradarv3.html](http://www.southport.jpl.nasa.gov/desc/imagingradarv3.html).
- [KING-92] Kingsley Simon and Shaun Quegan. Understanding Radar Systems. McGraw-Hill Book Co., England. 1992.
- [KRAS-88] Krassner, George and Jackson Michael. Space Communications Systems. McGraw-Hill, New York. 1964. pg. 130-166.
- [KRAU-88] Kraus, John D. Antennas. McGraw-Hill International Editions, New York. 1988.
- [KUMA-89] Kumar, A., and H.D. Hristou. Microwave Cavity Antennas. Artech House, Inc., Maine. 1989. pg. 101-210.

- [KWOK-89] Kwok, Ronald and William TK Johnson. *Block Adaptive Quantization of Magellan SAR Data*. IEEE Transactions on Geoscience and Remote Sensing, Vol. 27, No. 4. July 1989. pg. 375-383.
- [LARSa-92] Larson, Wiley J. and James R. Wertz. *Space Missions Analysis and Design*, 2<sup>nd</sup> ed. Microcosm, Inc., California. 1992. pg. 167-190.
- [LARSb-92] Larson, Wiley J. and James R. Wertz. *Space Missions Analysis and Design*, 2<sup>nd</sup> ed. Microcosm, Inc., California. 1992. pg. 339-468.
- [LARSc-92] Larson, Wiley J. and James R. Wertz. *Space Missions Analysis and Design*, 2<sup>nd</sup> ed. Microcosm, Inc., California. 1992. pg. 503-553.
- [LI-83] Li, F.K. and WTK Johnson. *Ambiguities in Spaceborne Synthetic Aperture Radar Systems*. IEEE Transactions on Aerospace and Electronic Systems, Vol. AES-19, No. 3. May 1983.
- [LIVI-91] Livingstone, Charles and Mark Drinkwater. *Springtime C-band SAR Backscatter Signatures of Labrador Sea Marginal Ice: Measurements versus Modeling Predictions*. IEEE Transactions on Geoscience and Remote Sensing, Vol. 29, No. 1. Jan 1991. pg. 29-41.
- [MARa-86] Maral, G., Bousquet, M. *Satellite Communication Systems*, 2<sup>nd</sup> ed. John Wiley & Sons, Chichester. 1986. pg. 96.
- [MARaA-93] Maral, G., Bousquet, M. *Satellite Communication Systems*, 2<sup>nd</sup> ed. John Wiley & Sons, Chichester. 1993. pg. 14-45.
- [MARAb-93] Maral, G., Bousquet, M. *Satellite Communication Systems*, 2<sup>nd</sup> ed. John Wiley & Sons, Chichester. 1993. pg. 227-248.
- [MASS-00] Massonnet, D., E. Thouvenot, S. Ramongassie, L. Phalippou. *A Wheel of Passive Radar Microsats for Upgrading Existing SAR Projects*. Proceedings of the International Conference on Geoscience and Remote Sensing Symposium, Vol. 3. 2000.
- [MASS-99] Massonnet, Didier. *Capabilities and Limitations of the Interferometric Cartwheel*. CNES Memo. November 1999.
- [MEER-01] Meerman, Max. "Design History of SSTL Microsatellites." Internal presentation for SSTL. 11 Sept, 2001.
- [MOCC-00] Moccia, A. N. Chiacchio, and A. Capone. *Spaceborne bistatic Synthetic Aperture Radar for Remote Sensing*. International Journal of Remote Sensing, Vol. 21, No. 18. pg. 3395-3414.
- [MOHR-00] Mohr, Johan and Soren Madsen. *The Impact of Curved Satellite tracks on SAR Focusing*. IEEE International Geoscience and Remote Sensing Symposium. 2000.
- [MRAZ-83] Mrazek, Catherine, and Samuel McCandless. *A Multi-Look Correlation Auto-Focus technique for Synthetic Aperture Radar*. IEEE National Telecommunications Conference. 1983. pg. 118-122.
- [MUFF-95] Muff, DG, AP Blake, and AM Horne. *Spaceborne SAR Autofocus*. IEE Colloquium on the Recent Development in Radar Imaging Systems. 1995. pg.11/1-11/11.
- [NASD-01] NASDA Website: <http://www.nasda.go.jp>.

- [NAVY-01] Navy Electronic Warfare Website: <http://ewhdbks.mugu.navy.mil>.
- [NEWK-96] Newkirk, Michael and Gary Brown. *A Waveform Model for Surface and Volume Scattering from Ice and Snow*. IEEE Transactions on Geoscience and Remote Sensing, Vol. 34, No.2. March 1996. pg. 444-456.
- [NGHI-94] Nghiem, S.V., R. Kwok, S.H. Yueh, and M.R. Drinkwater. *Polarimetric Signatures of Sea Ice: Theoretical Model*. Journal of Geophysical Research. 1994.
- [NOHA-98] Nohara, Tim J. *Design of a Space-based Radar Signal Processor*. IEEE Transactions on Aerospace and Electronic Systems, Vol. 34, No. 2. April 1998. pg. 366-377.
- [NOZE-96] Nozette, S., C.L. Lichtenberg, P. Spudis, R. Bonner, W. Ort, E. Malaret, M. Robinson, and E.M. Shoemaker. *The Clementine Bistatic Radar Experiment*. Science Vol. 274. Nov. 1996. pg 1495-1498.
- [OLIV-94] Oliver, A.D., PJB Clarricoats, A.A. Kisak, L. Shafai. *Microwave Horns and Feeds*. IEEE Press, New York. 1994. pg. 416-426.
- [OLIV-97] Oliver, Chris and Shaun Quegan. *Understanding Synthetic Aperture Radar Images*. Artech Hous, Inc., Maryland. 1997.
- [ONST-92] Onstott, Robert G. "SAR and Scatterometer Signatures of Sea Ice." *Microwave Remote Sensing of Sea Ice*. Frank D. Carsey [ed]. Geophysical Monograph Series, Washington DC. 1992. pg.73-110.
- [PARKa-99] Parkes, S.M. and H.L. Clifton. *The Compression of Raw SAR Image Data*. International Journal of Remote Sensing, Vol. 20, No. 18. 1999. pg. 3563-3581.
- [PARKb-99] Parkes, S.M. *Wide Bandwidth BAQ for On-Board Compression of Raw SAR Data*. Proceedings of the Data Systems in Aerospace Conference. May 1999. pg. 613-617.
- [PASC-98] Pascazio, V. and G. Schirinzi. *Synthetic Aperture Radar Imaging by One-bit Coded Signals*. Electronics & Communications Engineering Journal. Feb, 1998. pg. 17-28.
- [PASC-00] Pascazio, V., G. Schirinzi. *SAR phase history data compression by using wavelet packets*. IEEE International Geoscience and Remote Sensing Symposium. 2000.
- [PRAT-93] Prati, C. and F. Rocca. *Improving Slant Range Resolution with Multiple SAR Surveys*. IEEE Transactions on Aerospace and Electronic Systems, Vol. 29, No. 1. Jan 1993.
- [POGG-99] Poggi, Giovanni, Arturo RP Ragazini, and Luisa Verdoliva. *On-Board Compression of SAR Data Through Range Focusing*. IEEE International Geoscience and Remote Sensing Symposium. 1999. pg. 2247- 2250.
- [PYAT-78] Pyati, S. *Signal Processing of Synthetic Aperture Radar Data*. Internal Report no. TOR-0078(3070-20)-5. Aerospace Corporation. 1978.
- [RADA-01] RadarSat Homepage: <http://www.space.gc.ca>.
- [RAVE-66] Raven, R.S. *Requirements on Master Oscillators for Coherent Radar*. Proceedings of the IEEE Vol. 54, No. 2. Feb. 1966. pg. 237-247.
- [ROMB-99] Rombeck, F. and E. Weih. *Ultra-High Speed & Large Capacity Solid State Memories*. Proceedings of the Data Systems in Aerospace Conference. May 1999. pg. 631-634.

- [SCHA-99] Schaefer, C. and E. Krahn. *Processing and Storage Subsystems for Hig-Resolution SAR Instruments*. Proceedings of the Data Systems in Aerospace Conference. May 1999. pg. 625-630.
- [SCHI-00] Schiff, Conrad and John Bristow. *Formation Flying in Elliptical Orbits*. IEEE International Aerospace Conference. May 2000. pg. 37-47.
- [SEA-01] Sea Ice Monitoring Website:  
[http://fram.nrsc.no/CEO\\_Training/Training%20and%20Education/html/Word\\_html/Tr\\_M](http://fram.nrsc.no/CEO_Training/Training%20and%20Education/html/Word_html/Tr_M)
- [SKOLa-62] Skolnik, Merrill I. Introduction to Radar Systems. McGraw-Hill Kogakusha, Ltd., Tokyo. 1962. pg. 1-4.
- [SKOLb-62] Skolnik, Merrill I. Introduction to Radar Systems. McGraw-Hill Kogakusha, Ltd., Tokyo. 1962. pg. 20-114.
- [SKOL-70] Skolnik, Merrill I. The Radar Handbook. McGraw-Hill Book Co., New York. 1970. pg. 5-72.
- [SMIT-00] Smith, Ryan L. and David V. Arnold. *Development of a Low Cost, FM/CW Transmitter for Remote Sensing*. IEEE International Geoscience and Remote Sensing Symposium. 2000.
- [STEI-76] Steinberg, Bernard D. Principles of Aperture and Array System Design: Including Random and Adaptive Arrays. John Wiley & Sons, Inc., New York. 1976.
- [STEY-01] Steyn, Herman. "In-orbit ADCS results and achievements on SSTL Nano to Minisatellites." Internal presentation to SSTL. 24 Jul y2001.
- [STIL-00] Stiles, J., N. Goodman, SiChung Lin. *Performance and Processing of SAR Satellite Clusters*. IEEE International Geoscience and Remote Sensing Symposium. 2000.
- [STIMa-98] Stimson, George W. Introduction to Airborne Radar. Scitech Publishing, Inc., New Jersey. 1998. pg. Pg 163-185.
- [STIMb-98] Stimson, George W. Introduction to Airborne Radar. Scitech Publishing, Inc., New Jersey. 1998. pg. 253-277.
- [STIMc-98] Stimson, George W. Introduction to Airborne Radar. Scitech Publishing, Inc., New Jersey. 1998. pg. 393-435.
- [SOUM-89] Soumekh, M., J. Choi, and W. Zwolinski. *Target Imaging Using A Synthesized Bistatic Radar*. IEEE International Conference on Systems Engineering. 1989.
- [SOUM-91] Soumekh, Mehرداد. *Bistatic Syntheitc Aperture Radar Inversion with Application in Dynamic Object Imaging*. IEEE Transactions on Signal Processing, Vol. 39, No. 9. 1991. pg. 2044-2055.
- [SOUM-99] Soumekh, Mehرداد and Jeong-Hu Choi. *Phase and Amplitude Restoration in SAR Imaging*. IEEE Transactions of Image Processing, Vol. 1, No. 2. April 1999.
- [SUES-00] Suess, M., C. Schaefer and R. Zahn. *Discussion of the Intriduction fo On-Board Data Processing to Spaceborne SAR Instruments*. IEEE International Geoscience and Remote Sensing Symposium. 2000.

- [THOM-99] Thompson, Douglas, James Bates, and David Arnold. *Extending the Phase Gradient Autofocus for Low-Altitude Stripmap Mode SAR*. IEEE National Radar Conference. 1999. pg. 36-40.
- [TOLL-98] Tollefson, Mark V. and Bruce K. Preiss. *Space Based Radar Constellation Optimization*. IEEE International Aerospace Conference. May 1998. pg. 379-388.
- [TOMI-78] Tomiyasu, Kiyo. Bistatic Synthetic Aperture Radar Using Two Satellites. IEEE EASCON. 1978. pg. 106-110.
- [UTEX-01] University of Texas Radar Website: [www.csr.utexas.edu/projects/rs/whatisradar](http://www.csr.utexas.edu/projects/rs/whatisradar).
- [VACC-00] Vaccaro, R., P.C. Smits, S.G. Dellepiane. *Exploiting Spatial Correlation Features for SAR Image Analysis*. IEEE Transactions on Geoscience and Remote Sensing, Vol. 38, No. 3. May 2000.
- [WAHL-94] Wahl, D.E.; Eichel, P.H.; Ghiglia, D.C.; Jakowatz, C.V., Jr. *Phase Gradient Autofocus-A Robust Tool for High Resolution SAR Phase Correction*. IEEE Transactions on Aerospace and Electronic Systems, Vol. 30, No. 3. July 1994.
- [WICK-01] Wicks, Alex. "Constella Satellite." SSTL Marketing Information Page. 2001.
- [WILLa-91] Willis, Nicholas J. *Bistatic Radar*. Artech House, Inc., Maryland. 1991. pg. 59-67.
- [WILLb-91] Willis, Nicholas J. *Bistatic Radar*. Artech House, Inc., Maryland. 1991. pg. 70-81.
- [WILLc-91] Willis, Nicholas J. *Bistatic Radar*. Artech House, Inc., Maryland. 1991. pg. 191-195.
- [WILLd-91] Willis, Nicholas J. *Bistatic Radar*. Artech House, Inc., Maryland. 1991. pg. 255-265.
- [WOOD-98] Wood, Peter and Guy Seguin. *Synthetic Aperture Radar with a Spacecraft Antenna of Reduced Size*. European Conference on Synthetic Aperture Radar. 1998. pg. 171-174.
- [WONG-00] Wong, Frank, Ngee Leng Tan, Tat Soon Yeo. *Effective Velocity Estimation for Space-Borne SAR*. IEEE Geoscience and Remote Sensing Symposium. 2000.
- [WU-00] Wu, R. and J. Li. *Autofocus and Super-Resolution Synthetic Aperture Radar Image Formation*. IEEE Proceedings Radar, Sonar and Navigation, Vol. 47, No. 5. October 2000.
- [YANG-01] Yang, W.Q. and TY Ng. *Phase-Shiftable Signal Generator*. Electronics World. July 2001. pg. 514-520.
- [YE-99] Ye, Wei, Tat Soon Yeo, and Zheng Bao. *Weighted Least-Squares Estimation of Phase Errors for SAR/ISAR Autofocus*. IEEE Transactions on Geoscience and Remote Sensing, Vol. 37, No. 5. 1999. pg. 2487-2493.
- [YEH-00] Yeh, Pen-Shu, Jack Venbrux, Prakash Bhatia and Warner Miller. *A Real-Time High Performance Data Compressions Technique for Space Applications*. IEEE International Geoscience and Remote Sensing Symposium. 2000.
- [YUNC-94] Yunck, T.P. *Orbit Determination. Global Positioning System: Theory and Applications, vol II*. B.W. Parkinson and J.J. Spilker, Jr. [eds]. American Institute of Aeronautics and Astronautics. Washington. 1994. pg. 559-592.



- [ZAVA-99] Zavattero, Paul. *Distributed Target SAR Image De-Blurring Using Phase Gradient Autofocus*. IEEE International Radar Conference: Into the Next Millennium. 1999. pg. 246-250.
- [ZHUK-99] Zhukov, Boris, Dieter Oertel, Franz Lanzl and Götz Reinhäcke. *Unmixing-Based Multisensor Multiresolution Image Fusion*. IEEE Transactions on Geoscience and Remote Sensing, Vol. 37, No. 3. May 1999.